Title
Electronic Interfaces for Bacteria-Based Biosensing

Author
Zajdel, Thomas J.

Publication Date
2018

Peer reviewed|Thesis/dissertation

Electronic Interfaces for Bacteria-Based Biosensing

by

Thomas J. Zajdel

A dissertation submitted in partial satisfaction of the

requirements for the degree of

Doctor of Philosophy

in

Engineering – Electrical Engineering and Computer Sciences

in the

Graduate Division

of the

University of California, Berkeley

Committee in charge:

Professor Michel M. Maharbiz, Chair
Professor Kristofer S.J. Pister
Professor Adam P. Arkin

Fall 2018

Electronic Interfaces for Bacteria-Based Biosensing

Abstract

Electronic Interfaces for Bacteria-Based Biosensing

by

Thomas J. Zajdel

Doctor of Philosophy in Engineering – Electrical Engineering and Computer Sciences

University of California, Berkeley

Professor Michel M. Maharbiz, Chair

Bacterial sensing systems have evolved to detect complex biomolecules, operating near fundamental physical limits for biosensing. No modern engineered biosensor has managed to match the efficiency of bacterial systems, which optimize for each sensing application under constraints on response time and sensitivity. An emerging approach to address this shortfall is to build biosensors that electronically couple microbes and devices to combine the sensing capabilities of bacteria with the communication and data processing capabilities of electronics. This dissertation presents three techniques that advance engineering at the interface between bacteria and electronics, all working towards the integration of living material into hybrid biosensing platforms. In the first technique, we embed current-producing *Shewanella oneidensis* inside a conductive PEDOT:PSS matrix to electronically interface and structure the bacteria into 3D conductive biocomposite films to our specifications. In the second technique, we observe large numbers of chemotactic bacterial flagellar motor (BFM) behavior to infer environmental conditions, using machine learning to co-opt *Escherichia coli*'s motor response for the front end of a biosensor. In the final technique, we demonstrate progress towards a method to electronically monitor BFM rotation over time for electrochemical biosensing. Together, this body of work contributes to more functional interfaces between silicon- and carbon-based materials for advanced biosensing applications including persistent in situ environmental sensing and microbiorobotics.

To my family

Contents

List of Figures

List of Tables

Acknowledgments

First and foremost, I have a deep debt of gratitude to my advisor Michel Maharbiz. You guided my graduate career with consistent encouragement during the harder parts. Thanks for your support throughout these years. Thanks also go to Kris Pister, Adam Arkin, and Ali Niknejad for taking the time to serve on my committees.

I thank members past and present of the Maharbiz lab, for their help in navigating graduate school and being an excellent group to work with: Daniel Cohen, Travis Massey, Maysam Chamanzar, Konlin Shen, Camilo Diaz-Botia, Monica Lin, Amy Liao, Alyssa Zhou, Bochao Lu, DJ Seo, Arda Özilgen, David Piech, Oliver Chen, Mauricio Bustamante, KyoungTae Lee, Soner Sonmezoglu, Wei Li, Tim Hanson, and Josh van Kleef.

I give my thanks and admiration to the staff of the Marvell Nanofabrication Lab for their persistent work to keep things moving, especially to Greg Mullins, Joanna Bettinger, Richelieu Hemphill, Kim Chan, Ryan Rivers, Allison Dove, and Jeff Clarkson.

Without my wet lab mentors, I would never have realized my dream of working in biology. I thank the members of Adam Arkin's lab that helped me get started: Esteban Toro, David Chen, Kelly Wetmore, and Morgan Price. I thank Caroline Ajo-Franklin and her group for offering their lab as a second academic home: Michaela TerAvest, Moshe Baruch, Marimikel Charrier, Jose Cornejo, and Frankie Manea. Special thanks go to Behzad Rad for all his help with microscopy of all sorts and surface chemistry. I also thank Marc Chooljian for his input on microfluidics, and I thank Jasmine Nirody and Teuta Pilizota, for sharing their expertise regarding the bacterial flagellar motor.

I was lucky to work directly with many talented students who kept the research moving forward. Robin Herbert, Alex Walczak, Debleena Sengupta, Victor Tieu, Bilal Sheikh, Vikram Shirsat, Jove Yuan, Andrew Nam, and Meera Lester. I wish you luck in your future endeavors and am grateful for your help!

I was fortunate to have worked on meaningful education projects during my time at Berkeley. I thank the Electronics Support Group for their prompt help: Ming Wong, Katherina Wu, Winthrop Williams, Peter Caragher, and Skot Croshere. I am thankful for Eric Arvai for his creative input and heroic efforts for the Electronic Interfaces MOOC. I am indebted to Miki Lustig for letting me teach his amateur radio seminar for a year and for being a constant source of encouragement throughout the last few years.

To my friends at Berkeley and elsewhere - thanks for taking the time to visit, roll d20s, grill out, hike, boulder, and chat.

I thank my parents and my brother for their encouragement and patience as I toiled on this dissertation for so many years across the country. Stef, thanks for your companionship and unconditional support.

This work was supported by the Office of Naval Research, U.S. Department of Energy, Chan Zuckerberg BioHub, and a National Science Foundation Graduate Research Fellowship.

Lastly, I thank *you*, the one who is taking the time to read through any part of this dissertation. Please do not hesitate to reach out to me with any questions or comments you may have!

Chapter 1

Introduction

1.1 Prelude: Carbon & silicon

Microorganisms have evolved myriad adaptations for dealing with the problems of life, using billions of years to conform neatly to a virtually infinite array of environmental niches. Over the past hundred years or so, electronic devices have developed at a feverish pace, directed by careful design, propelled by technological discovery and lured by economic recompense. The systems of both the microbiological and monolithic silicon worlds developed to solve problems specific to their respective domains. Increasingly complex demands in healthcare, robotics, manufacturing, agriculture, and environmental stewardship require blended solutions that draw from both the living and the synthetic worlds. Ideally, organisms and electronics could directly exchange information, but the interfaces in use for this exchange are at present very rudimentary. This dissertation examines several methods to create biohybrid systems with more sophisticated interfaces to bridge the gap between carbon-based bacteria and silicon-based microsystems.

1.2 Why interface bacteria with electronics?

Bacteria live in every niche on this planet. Their range includes the deepest oceans, the highest mountains, the hottest hydrothermal vents, the coldest glaciers, and the grumpiest humans. Facing such varied situations, the bacterial kingdom presents us with a range of ingenious nanoscale multitools adapted for nearly every purpose. Bacteria sense biomolecules, actuate movement, accumulate materials against concentration gradients, generate chemiosmotic potentials, synthesize organic substrates, and catabolize countless compounds. Although bacteria are adapted to life in primarily aqueous environments, their diffusion-based communication methods are slow and they cannot perform complex digital computations like microprocessors do [1], [2].

Electronics have transformed modern life many times over since their proliferation throughout the past century. From thermionic valves to monolithic integrated circuits, elec-

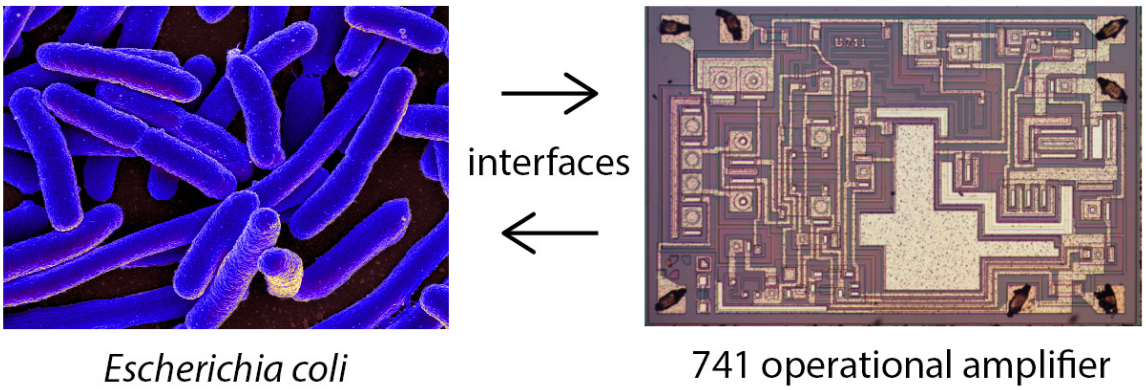

Figure 1.1: Interfacing bacteria and electronics. *Escherichia coli* is the most well-known bacterium in existence, and the 741 op amp is one of the most well-known monolithic integrated circuits. The two excel in very different environments. The colored scanning electron micrograph of *E. coli* on the left of this image, "*E. coli* Bacteria" by NIAID is licensed under CC-BY 2.0. The photograph of the 741 op amp die was taken by Ken Shirriff and is used with his permission.

tronics furnished society with its modern trappings: wireless communication, complex computation, data storage, ubiquitous persistent sensing, and so on. Despite recent strides, a brief encounter with a splash of water will send a smartphone directly into a bag of rice for dessication and silicon-based microrobotics systems have so far failed to reproduce the nanoscale rotary motors that propel flagellated microorganisms through their environments.

Great strides have taken place in both fields to compensate for their shortcomings. A substantial branch of synthetic biology aims to use organisms to make complex distributed computations [3]–[5]. Although micro-electromechanical systems (MEMS) have made progress in microassembly for various applications [6]–[8], silicon microassembly with the complexity of the bacterial flagellar motor's over 50 components has not yet been replicated [9]. On the other hand, despite the sophisticated analog computation that cells partake in [10], efficient digital computation on the scale of a microprocessor is out of reach.

The alternative approach explored in this dissertation is to build systems that electronically couple microbes and devices to combine the capabilities of the living world with those of advanced electronics (Figure 1.1). Biosensors already do this by definition and the sensing problem is central to this dissertation. Direct interfacing between bacteria and electronics is difficult, but emerging techniques will make such coupling more efficient. First, we will take a deeper look at the sensing problem.

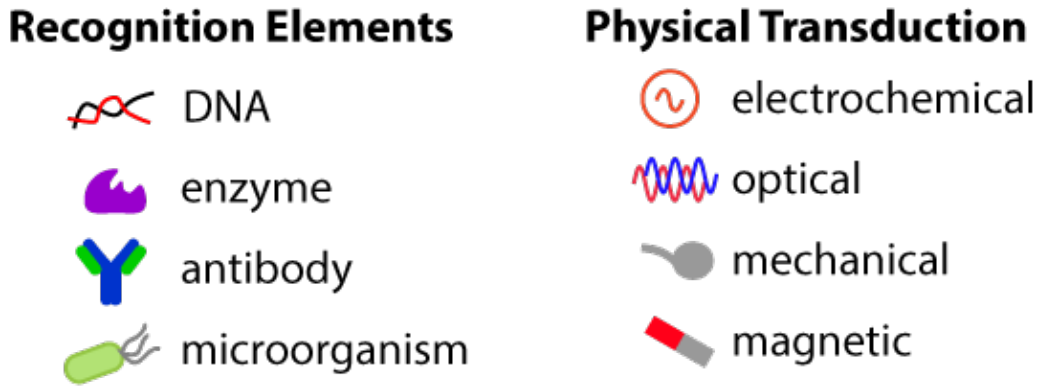

Figure 1.2: Biological recognition elements and physical transduction methods. Biosensors consist of a pairing between a biological recognition element and a physical transduction method. Cross any two to describe a subfield of biosensors. This is not an exhaustive list, but it does reflect the variety of biosensing strategies that have been developed.

1.3 The sensing problem

The sensing problem concerns collecting some information about an analyte in solution, such as its concentration, composition, or partial pressure. A **chemical sensor** transforms chemical information about an analyte into analytically tractable signals, such as voltages, light waves, or digital bits. Therefore, every chemical sensor has two connected components: a chemical detection element and a physical transducer for readout [11]. The remainder of this section describes the biosensing subset of chemical sensors, briefly surveys the biosensing literature, and concludes by laying out the physics governing the performance limits of biosensing.

1.3.1 Biosensors

A **biosensor** is a chemical sensor whose recognition element is biological in origin, such as an enzyme, biochemical receptor, nucleic acid, or cell [12]. The first biosensor was designed by Leland C. Clark, and it detected glucose [13]. Clark's sensor consisted of the enzyme glucose oxidase immobilized on the surface of a gas-permeable platinum electrode. Glucose oxidase, which is found in certain fungi and insects, catalyzes the reaction wherein oxygen is reacted with glucose to form hydrogen peroxide and D-glucono-δ-lactone [14]. The platinum electrode would monitor the electric current produced by oxygen reduction in order to measure the amount of available oxygen. In the presence of glucose, the glucose oxidase would consume oxygen to produce hydrogen peroxide and the oxygen current signal would decrease [15]. In this case, the analyte was glucose, the biological recognition element was the enzyme glucose oxidase, and the transduction involved producing an electric current.

Table 1.1: Brief survey of biosensor review literature.

Review	Readout				Biological Recognition Element			
	Echm.	Opti.	Mech.	Magn.	Nucl.	Enzy.	Anti.	Cell
Arlett et al. [16]	X	X	X		X	X	X	
Tamayo et al. [17]			X		X	X	X	
Llandro et al. [18]				X	X		X	
Huan et al. [19]				X	X	X	X	
Su et al. [20]	X	X						X
TerAvest et al. [21]	X							X
Leung et al. [22]		X			X	X	X	
Khalil et al. [23]		X						X
Shao et al. [24]	X				X	X		
Wang [25]	X			X	X	X	X	
Wang et al. [26]	X				X			
Chen et al. [27]	X					X		

Since Clark's invention in the 1960s, biosensor development has grown at an accelerating pace. Any single pairing of a biological recognition element with a physical transduction method delineates a rich subfield (Figure 1.2). A brief survey of biosensor literature reviews is presented in Table 1.1. This table emphasizes the sheer diversity of biosensing strategies reported in the literature. It classifies each review into four types of readouts (electrochemical, optical, mechanical, and magnetic) and four types of biological recognition elements (nucleic acid, enzyme, antibody, and whole cell).

Why are so many different types of biosensors being developed? Every biosensor must balance constraints on power, response time, and sensitivity. Each readout method and biological recognition element comes with its advantages and disadvantages. For example, optical readouts generally are more sensitive but have longer response times, while electrochemical sensors are generally faster but less sensitive. A non-exhaustive survey of published biosensors, each plotted by their response time and detection limit, is shown in Figure 1.3. A natural trade-off between response time and sensitivity is evident. It turns out that this relationship is deeply rooted in the fundamental physics of biosensing.

1.3.2 The "perfect" biosensor

The Perfect Monitor was conceived by Berg and Purcell as a theoretical instrument with spherical shape of radius a, permeable walls, and the ability to instantly count all the particles located within its volume V [28], as pictured in Figure 1.4. A single such snapshot would yield in expectation an estimated number of molecules $n_x = Vc_x$. Because the molecules move about independently, n_x is Poisson distributed (i.e., $\langle(\delta n_x)^2\rangle = \langle n_x\rangle$), and when in-

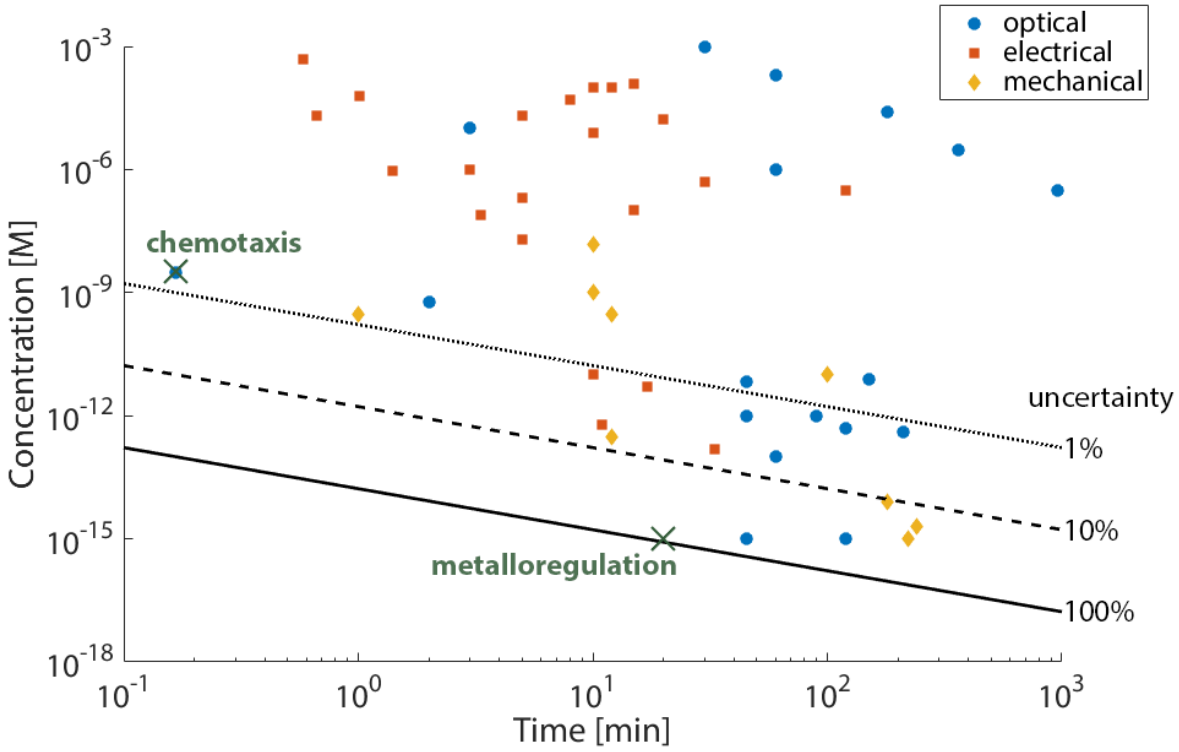

Figure 1.3: Survey of biosensor response time and sensitivity, adapted from two biosensor reviews [16], [20]. Optical, electrical, and mechanical readouts are labeled by different markers. The Perfect Monitor limits are noted for 1%, 10%, and 100% sensitivity by the dotted, dashed, and solid black lines, respectively [28]. The green X's mark the performances of two specific sensing systems in *E. coli*: chemotaxis [29] and metalloregulation [30].

ferring the external concentration c_x from a single count, a "perfect" instrument makes an error given in Equation (1.1):

$$\frac{\langle(\delta c_x)^2\rangle}{c_x^2} = \frac{\langle(\delta n_x)^2\rangle}{\langle n_x\rangle^2} = \frac{Vc_x}{(Vc_x)^2} = \frac{1}{Vc_x}. \tag{1.1}$$

However, if allotted enough time, the Monitor can take several such counts to reduce this uncertainty. For these measurements to be statistically independent of each other, the Monitor must wait for the amount of time it takes for most molecules to clear out of its volume by diffusion: $t = V^{2/3}D$, where D is the diffusion coefficient. So for a given measurement period T, with approximately $T(D/V^{2/3})$ such counts, the cell's measurement is left with an error given in Equation (1.2):

$$\frac{\langle(\delta c_x)^2\rangle}{c_x^2} = \left(\frac{V^{2/3}}{TD}\right)\left(\frac{1}{Vc_x}\right) = \frac{1}{DV^{1/3}c_xT} \approx \frac{1}{Dac_xT}. \tag{1.2}$$

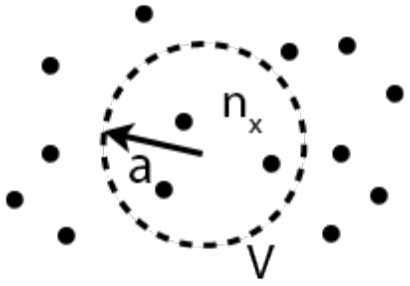

Figure 1.4: A Perfect Monitor counts n_x particles inside its volume V to estimate the concentration of these particles in the bulk solution $c_x = \frac{n_x}{V}$ cm^{-3}.

By considering the correlations between particles within the sphere, Berg and Purcell derived the exact measurement error of a single Perfect Monitor given a measurement period T shown in Equation (1.3):

$$\frac{\langle(\delta c_x)^2\rangle}{c_x^2} = \frac{3}{5\pi D a c_x T}. \tag{1.3}$$

A full derivation of this error is provided by Berg and Purcell [28]. Important to note is that a heavier biomolecule with larger diffusion coefficient D will require more time to take a measurement with the same uncertainty as that of a smaller biomolecule with a smaller diffusion coefficient.

The Perfect Monitor gives us a point of reference with which to judge biosensors known as the Berg-Purcell limit, and it is denoted in Figure 1.3 by the black lines (dotted for 1% uncertainty, dashed for 10%, and solid for 100%), assuming that the radius of the monitor is $a = 1$ µm, and that the diffusion coefficient is $D = 1 \times 10^5$ cm^2 s^{-1}, which approximates most amino acids [31]. A number of biosensors apparently overcome these fundamental reference points, but they do so by employing some method of capture that pre-concentrates the analyte before detection, thus countering the higher fluctuation in counts encountered in very dilute solutions.

How do these engineered systems compare with the bacterium? *Escherichia coli* is known to operate around these fundamental limits on both short and long timescales, marked with X's in Figure 1.3 in each case [29], [30], [32]. Understanding why *E. coli* tolerates more uncertainty for some applications than others requires understanding what is being detected and for which purpose it is being detected.

1.4 Sensing in bacteria

Most bacteria are like *E. coli* in that they have a fast response and a slow response to adapt to their environment. Over very short timescales, on the order of seconds to minutes, *E.*

coli uses its chemotaxis system to bias its movement towards nutrients and away from toxins. In this case, the sensing system must be very sensitive to minute changes in concentration to properly detect chemical gradients and its performance approaches the 1% uncertainty line. Over longer generational timescales, on the order of 20 minutes to hours, *E. coli* responds to environmental conditions by modifying its genetic expression through transcription and translation [33]. Depending on what is being detected by which system, *E. coli* has a different tolerance for uncertainty.

The molecular mechanism that *E. coli* uses to detect analytes in solution is inherently fast. Receptor proteins are designed to bind tightly with their analyte ligands when they encounter each other, and binding/unbinding events happen on the order of milliseconds [34]. *E. coli* must determine how to read these events and respond to them as quickly as possible given the tolerance for error in each case.

1.4.1 Transcription: A slow and sensitive response

One example of a very sensitive transcription-regulated response is metalloregulation in *E. coli*. Zinc is toxic to *E. coli* in excess concentrations, so its level within the cell is tightly controlled [35]. In Figure 1.3, the metalloregulatory response of *E. coli* to zinc is denoted with a green X, with a response time of 20 minutes and a femtomolar sensitivity [30]. The transcription of zinc regulation machinery, such as the ZntR export proteins, is regulated by the DNA and zinc-binding Zur protein. The high affinity of the Zur protein to Zn(II) ions, in addition to the sharp increase of affinity of Zur for the *znuC* promoter after binding to Zn(II), ensures transcription and translation of the regulatory machinery in the presence of 1 fM Zn(II), which corresponds to one atom per 10^6 cell volumes. Such high sensitivity means that *E. coli* will produce the export proteins in response to the presence of Zn(II) without much regard to the exact concentration. Roughly one cell generation, about 20 minutes, is the time that it takes for the regulatory proteins to be expressed, so this response approaches the fundamental limit of the Perfect Monitor with a very high tolerance for inaccuracy.

1.4.2 Chemotaxis: A fast and accurate response

In contrast to the metalloregulatory transcriptional system, chemotaxis requires very accurate estimates of the concentration of nutrients over timescales on the order of seconds. The cell modulates its motility in response to chemical gradients in its environment. Since the cell body is small (about 1-2 micrometers in length), it is nearly impossible for the cell to detect a spatial gradient along its length [28]. Therefore, *E. coli* and other prokaryotic organisms use a kinase-phosphatase biochemical signaling network to quickly monitor changes in concentration with respect to time as they sample their surroundings. They then bias their motility in the direction of a rising chemical gradient. Chemotaxis is remarkably fast; large step changes in the chemoattractant L-serine affect motility within 300 ms [36]. Chemotaxis is also sensitive; the detection limit for the chemoattractant L-aspartate is 3.2 nM, which corresponds to the detection of 3 molecules per cell volume [29]. This balance places chemo-

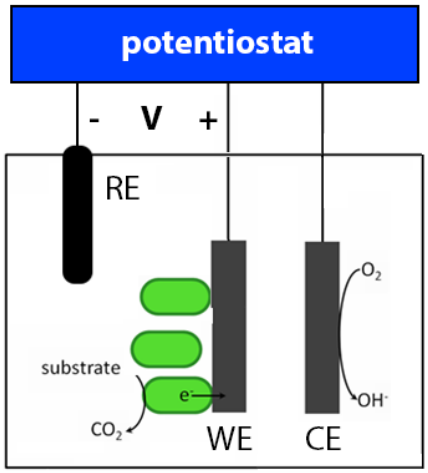

Figure 1.5: A typical three-electrode microbial electrochemical system. WE = working electrode, CE = counter electrode, and RE = reference electrode (typically Ag/AgCl). The potentiostat poises the working electrode at some potential above the reference and measures the resultant current.

taxis near the fundamental Berg-Purcell limit for the ideal biosensor for high accuracy and is marked in Figure 1.3 with a green X. The high accuracy is required in this case so that the cell can detect minute increases in nutrient concentration. The chemotaxis system is elaborated upon in more detail in Section 3.2.

1.5 Electronic interfaces with bacteria

The advantages of electrochemical readouts for chemical sensors include relatively low power requirements, rapid response times, and large spatial coverage. Electrochemical interfaces therefore have great potential for quickly reading out bacterial responses to their environment. Bacteria live in electrolytic solutions, so any electronic interface with bacteria will involve an aqueous phase with dissolved salts. In this section, we first introduce microbial electrochemical systems and highlight their potential for biosensing applications. We then consider more carefully various circuit models that describe the transfer of charge at the electrode-electrolyte interface, which is relevant to both microbial electrochemical systems and abiotic electrode-solution interfaces. We then conclude with a brief description of how electrochemical impedance spectroscopy can be used to characterize electrochemical interfaces.

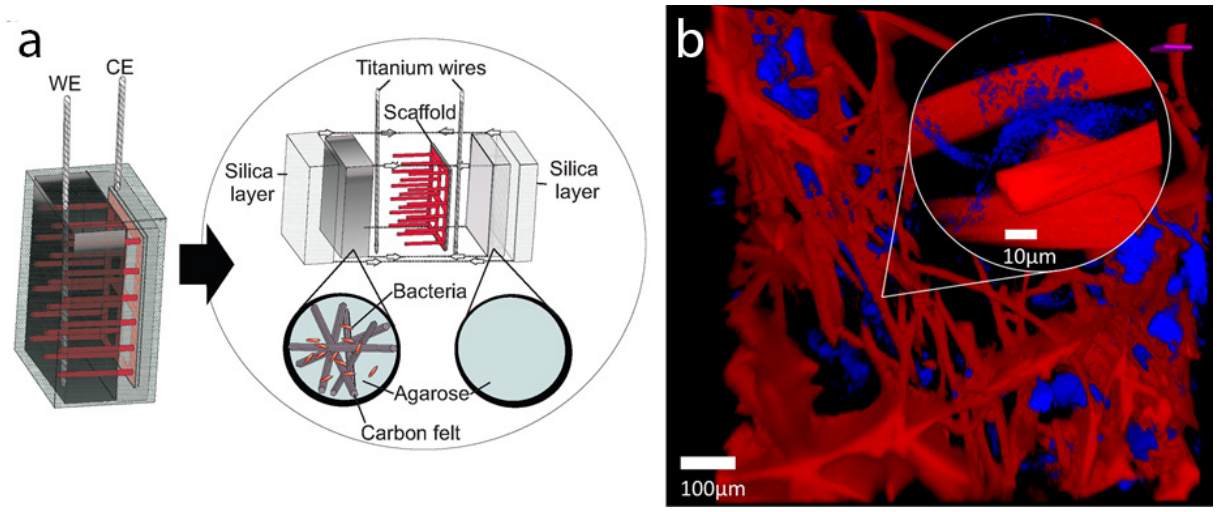

Figure 1.6: Miniaturized bioelectronic sensing system (BESSY). (a) Miniaturized reactor geometry. (b) Reconstructed confocal image of the bacteria-agarose-carbon felt matrix. Bacteria in blue and carbon fibers in red. Reproduced and adapted with permission from Zhou et al. [42], licensed under CC-BY 4.0.

1.5.1 Microbial electrochemical systems

Microbial electrochemical systems (MES) facilitate the direct transfer of charge between electroactive bacteria and an anode [37], usually by the oxidation and reduction of diffusible redox shuttles like riboflavin [21], [38]. A typical MES is illustrated in Figure 1.5, where a potentiostat is used to poise a working electrode (anode) at a constant potential with respect to a Ag/AgCl reference electrode and measure the resultant current traveling between the working electrode and counter electrode (cathode). In the case of the MES illustrated, the oxidation of a hydrocarbon substrate is coupled to electron transfer to a working electrode.

Shewanella oneidensis is an electroactive species of bacteria commonly used in MESs [39]. The metal reducing (Mtr) pathway allows *S. oneidensis* to respire on metal ions outside its membrane, acting as an electron conduit from the redox processes happening inside the cell to an external electron sink through either direct electron transfer or riboflavin-mediated transfer [40], [41]. This current can be measured and monitored by a potentiostat as an output signal.

Potentiostats can be miniaturized to the point of environmental deployment, as with the BioElectrochemical Sensing SYstem (BESSY) by Zhou et al. [42] shown in Figure 1.6. The miniaturized reactor is encapsulated by a silica sheath and produces $6.31\,\mu A\,cm^{-3}$. Closer inspection of the BESSY anode in Figure 1.6b reveals that the bacteria are in some cases separated from the carbon fiber conductors by up to $10\,\mu m$, requiring flavin diffusion to connect the cells to the carbon fiber. The approximate diffusion coefficient for riboflavin, a redox shuttle used by *S. oneidensis* for external electron transfer, is $D \approx 5 \times 10^{-6}\ cm^2\,s^{-1}$

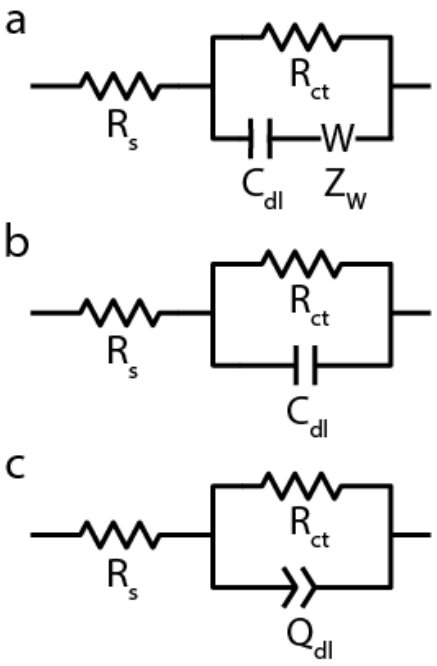

Figure 1.7: Randles circuit models of the electrode-electrolyte interface: (a) the standard Randles circuit, (b) removing the Warburg diffusion impedance, and (c) using a constant phase element for electrode polarization.

[43], which means that it would take up to 300 ms for the shuttles to diffuse 10 µm. This extra leap drastically reduces the electron transfer rate, and therefore reduces the current output of BESSY. If there were a way to program more intimate conductive contact between the bacteria and the anode, the current production density could be increased significantly. Such a method is described in Chapter 2.

Microbial electrochemical systems present us with an opportunity to directly couple bacterial sensing systems to an electronic readout. Because bacteria live in electrolytic solutions, the nature of the electrode-electrolyte interface must be considered carefully.

1.5.2 Equivalent circuit models for electrode-electrolyte interfaces

When an electrode is immersed in a solution and energized with an electric potential, charge may be transferred across the solid-liquid interface in one of two ways: 1) faradaic current due to redox reactions at the interface and 2) charging current. The dynamics of this electron transfer can be modeled as an electrical impedance using the so-called Randles equivalent circuit model [44], [45] shown in Figure 1.7a. This equivalent circuit consists of the electrolyte resistance of the solution R_s in series with a double layer capacitance (C_{dl}) in

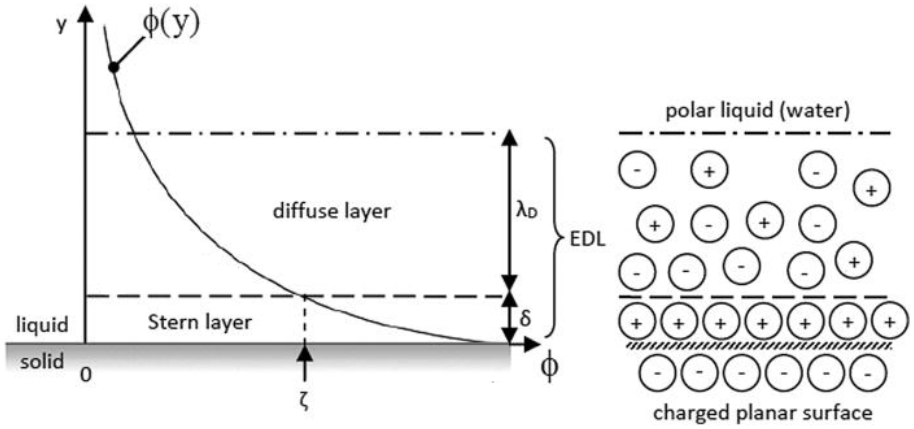

Figure 1.8: The electrical double layer. Adapted from Li et al. [48] with permission.

parallel with the charge transfer resistance R_{ct} and a Warburg impedance Z_W that models diffusion [46]. Since the Warburg element is generally only important at very low frequencies (< 1 Hz), the simplified circuit in Figure 1.7b can often be used. Sometimes a constant phase element (Q_{dl}) is used in the place of the double layer capacitance C_{dl}, as in Figure 1.7c, since it better approximates the behavior of real systems [47]. The remainder of this section will break down the individual components of the Randles circuit model.

Electrical double layer impedance

The electrical double layer results when a potential applied to an electrode in contact with an electrolytic solution. Electrostatic interactions between ions in the solution and the potential of the electrode result in a layer of ions tightly bound to the electrode surface followed by a second, more diffuse layer of counterions (Figure 1.8). The potential ϕ resulting from this charge distribution drops off exponentially with the distance from the electrode, characterized by the Debye length λ_D [48]. This charge separation at the interface can be modeled as a capacitor C_{dl} [49] by Equation (1.4).

$$C_{dl} = \epsilon \frac{A}{\lambda_D} \tag{1.4}$$

ϵ is the electric permittivity of the solution in $\mathrm{F\,m^{-1}}$, A is the area of the interface in $\mathrm{m^2}$, and λ_D is the Debye length in m. The Debye length is ultimately a function of the ionic strength, or electrolyte concentration, of the solution, following Equation (1.5) [49].

$$\lambda_D = \sqrt{\frac{\epsilon RT}{2F^2 I_c}} \tag{1.5}$$

ϵ is the electric permittivity of the solution in $\mathrm{F\,m^{-1}}$, R is the gas constant in $\mathrm{J\,mol^{-1}}$, T is the temperature in K, F is the Faraday constant in $\mathrm{C\,mol^{-1}}$, and I_c is the ionic strength in

M. The ionic strength I_c for a given solution can be computed by Equation (1.6).

$$I_c = \frac{1}{2}\sum_{i=1}^{n} c_i z_i^2 \tag{1.6}$$

The solution is assumed to consist of i ions, c_i is the concentration of ion i and z_i is the valency of ion i.

The double layer capacitance is a good first approximation, but in practice, the electrical double layer tends to act more like a "leaky" capacitor, better modeled by the constant phase element (CPE) [50]. The CPE impedance Z_Q is described by Equation (1.7).

$$Z_Q = \frac{1}{Q(j\omega)^\alpha} \tag{1.7}$$

ω is the stimulus angular frequency in rad/s, j is the imaginary number, and Q and α are parameters describing the CPE. Q has units $\mathrm{F\,s^\alpha}$ and α is a unitless number between -1 and 1. The CPE therefore acts like a capacitance in that its impedance decreases with an increase in frequency and that it has a constant phase value (typically between -80 and -70 degrees).

Solution resistance

The solution resistance R_s describes the phenomenon of charge traveling through the bulk solution to the electrode. Its value depends on electrode geometry and electrolyte concentration by the relationship in Equation (1.8) [51]:

$$R_s = \kappa\rho \tag{1.8}$$

ρ is the resistivity of the solution in $\Omega\,\mathrm{m}$ and κ is the cell constant in m^{-1} [51]. For a uniform electric field applied across a rectangular volume, the cell constant follows Equation (1.9), where ℓ is the volume's length in m and A is its cross-sectional area in m^2.

$$\kappa = \frac{\ell}{A} \tag{1.9}$$

For electrode geometries that do not result in a uniform electric field, such as coplanar electrodes, the cell constant must be calculated by using a geometric transformation to account for the nonuniformities in the field, such as Schwartz-Christoffel mapping [51], [52].

Charge transfer resistance

If a single electrochemical reaction is occurring at equilibrium, faradaic current is flowing across the interface. The potential applied to the electrode controls the reaction's kinetics. The rate of charge transfer across the interface may be modeled as an electric current. If

the applied potential has a small amplitude, this charge transfer can be modeled as a linear resistance R_{ct} with the expression in Equation (1.10) [46].

$$R_{ct} = \frac{RT}{nFi_0} \tag{1.10}$$

R is the gas constant in $\mathrm{J\,mol^{-1}}$, T is the temperature in K, n is the number of electrons involved in the redox reaction at the electrode, F is the Faraday constant in $\mathrm{C\,mol^{-1}}$, and i_0 is the exchange current density in $\mathrm{A\,m^{-2}}$, which is a function of electrode composition, the specific electrochemical species involved, temperature, and other factors [53]. The charge transfer resistance is often measured by electrochemical impedance spectroscopy [46].

Warburg diffusion impedance

Rate-limiting diffusion of electrochemical species to the electrode gives rise to the frequency-dependent Warburg impedance Z_W. For microelectrode systems where the double layer impedance is high, the Warburg impedance is typically only relevant for very low frequencies at steady state and can often be ignored in analysis. It is presented in Equations (1.11) and (1.12) for reference [46].

$$Z_W = \sigma\left(\omega^{1/2} - j\omega^{1/2}\right) \tag{1.11}$$

$$\sigma = \frac{RT}{n^2F^2A\sqrt{2}}\left(\frac{1}{C_O^*\sqrt{D_O}} + \frac{1}{C_R^*\sqrt{D_R}}\right) \tag{1.12}$$

R is the gas constant in $\mathrm{J\,mol^{-1}}$, T is the temperature in K, n is the number of electrons involved in the redox reaction at the electrode, F is the Faraday constant in $\mathrm{C\,mol^{-1}}$, A is the interface area in $\mathrm{m^2}$, D_O and D_R are the diffusion coefficients of the oxidant and reductant respectively in $\mathrm{m^2\,s^{-1}}$, C_O^* and C_R^* are the bulk concentrations of the oxidant and the reductant respectively.

1.5.3 Impedance-based electrode interface characterization

Electrochemical impedance spectroscopy (EIS) is commonly used to characterize electrochemical systems, whether they are biotic or abiotic. An small-amplitude sinusoidal potential V_ω is applied to the electrode of interest and the response current I_ω is measured at a specific frequency ω. From these measurements, the impedance Z_ω is calculated by the ratio in Equation (1.13):

$$Z_\omega = \frac{E_\omega}{I_\omega} \tag{1.13}$$

The impedance Z_ω is a complex number representing the difference in amplitude and phase between voltage and current. During EIS, the impedance is measured for a range of frequencies to perturb the electrochemical system and to help determine the equivalent circuit component values (e.g. R_{ct}, C_{dl}, etc.). EIS has been used to monitor the migration of biological cells [51], cell density [54], and particle sizing [55], and can be a rapid way to assess the electrochemical environment in which sensing electrodes are immersed.

1.6 Dissertation organization

This dissertation presents three techniques that advance engineering at the interface between bacteria and electronics, all working towards the integration of bacteria into hybrid biosensing platforms. In Chapter 2, we discuss embedding current-producing bacteria inside a conductive polymer matrix to enhance current generation in a microbial electrochemical system for bioelectronics. In Chapter 3, we discuss observing large numbers of chemotactic bacterial flagellar motor behavior to infer environmental conditions. In Chapter 4, we demonstrate our progress towards a method to electronically monitor BFM rotation over time for electrochemical biosensing. These methods aim to form a more perfect union between the silicon- and carbon-based worlds existing in a future that is briefly imagined with the parting words in Chapter 5.

Chapter 2

Fabricating multilayer conductive bacterial films

The content of this chapter was adapted with permission from an early manuscript of the following paper:

- "PEDOT:PSS-based multilayer bacterial-composite films for bioelectronics" by T.J. Zajdel*, M. Baruch*, G. Méhes*, E. Stavrinidou, M. Breggren, M.M. Maharbiz, D.T. Simon, and C.M. Ajo-Franklin [56]

2.1 Prelude: Building bioelectronic structures

By electronically coupling microbes and devices, bioelectrochemical systems combine the capabilities of the living world with those of advanced electronics. However, while we can precisely control the structure of the non-living electronic components, bioelectrochemical systems often rely on natural biofilm formation, limiting their applications. In this chapter, we co-opt an organic conductive polymer, PEDOT:PSS, to electronically interface and structure bacteria into 3D conductive biofilms to our specifications. By packing the bacteria more densely into a biofilm while maintaining nutrient flow and electrical conductivity, we increase the current density by 20x. Moreover, we demonstrate that the bacterial cells transfer electrons to the organic conducting polymer using two of the most common electron transfer mechanisms – the first time such mechanisms have been elucidated for this class of materials. Thus, this work provides the mechanistic understanding and methodology to structure cells into 3D biofilms that will be applicable to virtually any electroactive microorganism. This advance enables these systems to access the full range of microbial diversity and previously inaccessible 3D structures of microbes, opening a swath of new engineering possibilities in bioelectrochemical systems.

2.2 Fabricating multilayer conductive bacterial films

Electroactive bacteria commonly used for biosensing, including *S. oneidensis* and engineered *Escherichia coli*, do not form thick biofilms [57], [58] and may produce relatively low currents [41], [59] and therefore feature a small signal-to-noise ratio for the small anode volumes desired in environmental deployment. Because the anode of a microbial electrochemical system (MES) interfaces directly with bacteria, it is of great interest to develop a modification scheme that increases the density of cell-anode attachment beyond that of natural biofilms and also ensures that all cells are able to transfer electronic charge to the anode effectively. To ensure deployability, any modification should not significantly increase the anode's volume or reduce analyte permeability.

Because the anode's effective surface area limits the number of bacteria that make electrical contact, many modification approaches aim to maximize the anode's surface area-to-volume ratio. These methods include the use of high effective area porous carbon structures such as carbon felt (CF) [60], carbon cloth [61], carbon nanotubes [62], graphene foam [62], or precious metals such as gold nanoparticles [63] and graphene-gold composites [64]. However, the inherent hydrophobicity of carbon-based structures is incompatible with robust microbial adhesion [65], and these methods are also restricted to use with species that are capable of producing a robust biofilm. Polymer-based materials, such as polyaniline or polypyrrole (PPy), have also been used in an attempt to increase power density in MESs [66], [67]. In addition, encapsulation of *S. oneidensis* by PPy has also been recently demonstrated to enhance the electron transfer rate from bacteria to anodes while maintaining bacterial viability [68]. However, these materials do not significantly increase the density of the thin biofilm naturally formed by *S. oneidensis* [69].

The highly conducting and biocompatible organic polymer, poly(3,4-ethylenedioxythiophene) (PEDOT), has seen broad adoption in biological-electronics interfaces [70]–[74]. PEDOT has become a de facto standard material for organic bioelectronics due to its well-defined redox properties, large volumetric capacitance, mixed electronic/ionic conduction, and stability in water when mixed with poly(styrenesulfonate) (PSS) as a dopant. Chemically-polymerized and electrospun PEDOT has been used to increase the surface area and conductivity of anodes in MESs and microbial fuel cells (MFCs) [75]–[77]. Thin films (500–900 nm thick) of gram-negative bacteria on indium-tin-oxide (ITO) have also been produced using PEDOT [78], but live electroactive bacteria were only located on the outermost layers, limiting the density of current production. Therefore, a method of embedding viable electroactive bacteria in a thick multilayer conductive biofilm would increase the bacterial density at the anode and increase the generated signal level beyond that of present methods.

To address this need, we have developed a multilayer conductive bacterial film (MCBF) produced by the nutrient-permeable embedding of living *S. oneidensis* MR-1 in electropolymerized PEDOT:PSS and its simultaneous immobilization on a porous carbon felt substrate. The resulting MCBFs show a 20-fold increase in steady-state current production over unmodified CF anodes when used in standard MESs. The scalable anode fabrication process, improved electron transfer through a 3D conductive biomatrix, high viability, and the abil-

Table 2.1: Strains used for MCBF preparation.

Strain	Background	Genotype	Phenotype	Reference
MFm005	MR-1	WT	wild type *S. oneidensis*	[79]
MFm042	MR-1	Δ*mtrB*	current-deficient *S. oneidensis*	[38]
MFm070	MR-1	Δ*bfe*	flavin-deficient *S. oneidensis*	[80]

ity to use strains that do not form thick native biofilms demonstrate an important advance towards establishing advanced, field-deployable anode modifications for MESs.

2.3 Methods

2.3.1 Strains and growth conditions

All strains used in these experiments were derived from wild type *S. oneidensis* MR-1 [79] and are listed in Table 2.1. For the remainder of this chapter, strains are referred to by their genotype. Δ*mtrB* lacks the transmembrane porin MtrB that facilitates the interaction between MtrA and MtrC, and therefore is deficient in current production [38]. Δ*bfe* lacks the bacterial flavin adenine dinucleotide [FAD] exporter, which results in a severe decrease in extracellular riboflavin levels [80].

Cultures were inoculated from frozen glycerol stocks into 250 mL Erlenmeyer flasks, containing 50 mL Luria-Bertani (LB) medium and grown overnight at 30 °C with 250 rpm shaking. After overnight growth, the cells were harvested by centrifugation at 5200 rcf at 4 °C for 10 minutes and washed twice with M9 medium. Finally, the cell pellet was resuspended in M9 medium to the desired cell density for its use.

2.3.2 Testing *S. oneidensis* ability to transfer electrons through PEDOT:PSS

Gold and PEDOT:PSS test anodes were prepared to test the ability of *S. oneidensis* to transfer electrons through PEDOT:PSS. Glass microscope slides were coated with 10 nm Ti, then 10 nm Au using a standard electron beam physical vapor deposition (EBPVD) process (for more information, refer to Appendix A). To prepare the electropolymerization solution, poly(sodium 4-styrenesulfonate) (PSS) and EDOT were dissolved together in 35 mL M9 medium, to a final EDOT concentration of 10 mM and EDOT/PSS weight ratio of 0.05. Three of these slides were coated by PEDOT:PSS by immersion in the electropolymerization solution followed by being held at 1 V versus a Ag/AgCl reference electrode for 2 hours. After electropolymerization, the thickness of the PEDOT:PSS film was measured with a Dektak 3030 surface profiler. Additionally, the Au and PEDOT:PSS films were imaged with a Zeiss Gemini scanning electron microscope set to an extra high tension voltage level of 1.5 kV, under vacuum (5.0×10^{-5} mbar), with a working distance of 2 mm.

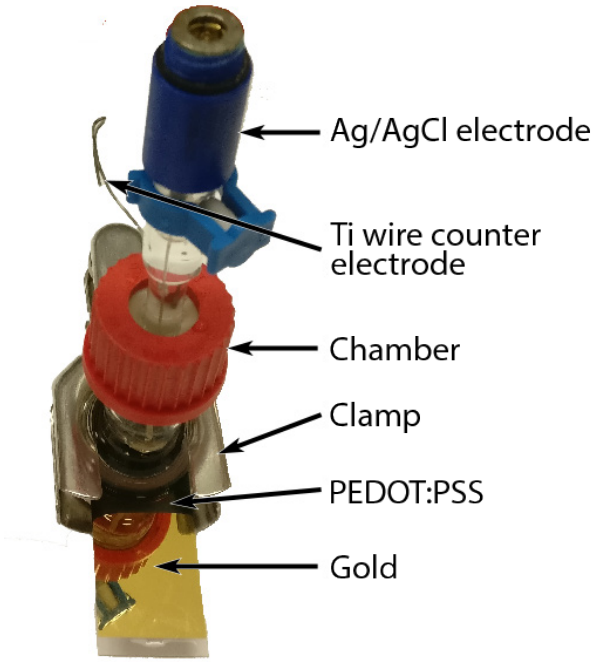

Figure 2.1: Reactor for measuring current transfer to gold and PEDOT:PSS thin films.

Then, each film was tested in a three-electrode single chamber bioelectrochemical reactor with a 10 mL solution volume as shown in Figure 2.1. The reactors consisted of a glass cylinder clamped to the microscope slide and film under test, sealed by an O-ring. A Ti wire was used as the counter electrode and a Ag/AgCl electrode was used as the reference.

Reactors were filled with M9 medium and the film under test was set to 200 mV above the reference with a BioLogic VMP-300 multipotentiostat. After a half hour to allow the current to stabilize, lactate was added to the reactors to 40 µM, and bacteria was injected to $OD_{600} = 1.7$. The experiment was done with WT *S. oneidensis* MR-1, $\Delta mtrB$, and Δbfe. After 20 hours of incubation, 10 µM riboflavin was added to the Δbfe reactors to saturate the culture with electron shuttles.

2.3.3 Embedding *S. oneidensis* into electropolymerized PEDOT:PSS

Preparation of the electrodes was performed at 4 °C to maintain the viability of the bacteria throughout the electropolymerization process. Briefly, EDOT/PSS solution was mixed with a concentrated *S. oneidensis* MR-1 suspension immediately before introduction to a carbon felt anode immobilized in an agarose gel and poised at 1 V versus a Ag/AgCl electrode, as illustrated in Figure 2.2. As a result, bacteria were embedded by a PEDOT:PSS film in proximity to the carbon felt anode.

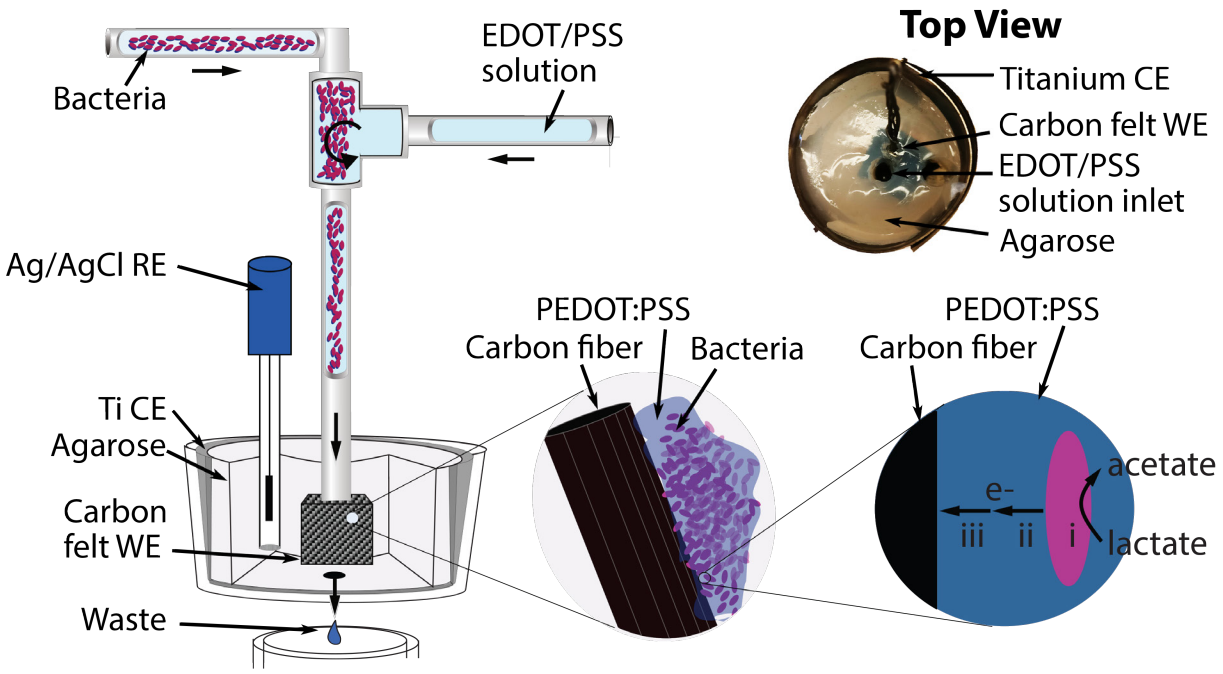

Figure 2.2: Schematic of the electropolymerization system, including a photograph of a single well. The electron flow in the final structure is (i) reduction of lactate to acetate by bacteria, (ii) transfer of electrons from bacteria to the PEDOT:PSS scaffold, and (iii) conduction of electrons through PEDOT:PSS scaffold to carbon felt substrate.

To prepare the electropolymerization solution (EPS), poly(sodium 4-styrenesulfonate) (PSS) (Sigma Aldrich) and EDOT (Sigma Aldrich) were dissolved together in 200 mL M9 medium, to a final EDOT concentration of 10 mM and EDOT/PSS weight ratio of 0.05. Then, electrodes were cut from 6.35 mm thick CF (Alfa Aesar) into 1.0 cm x 1.0 cm squares, and each one was soaked in 1 mL of M9. Each carbon felt electrode was lightly compressed to remove trapped air bubbles.

The electropolymerization platform consisted of a 6-well cell culture plate and custom 3D-printed stage for holding the electrodes, a peristaltic pump for the infusion of EPS, and a multi-syringe pump for infusion of bacterial culture, as shown in Figure 2.3. Holes 2 mm in diameter were drilled through the center of each well to promote drainage. This setup allowed for the preparation of six anodes in parallel.

Pieces of 0.25 mm thick titanium foil (Sigma Aldrich), sheared to a 25 mm by 150 mm strips, were wrapped into cylindrical shapes and inserted into each well to act as a counter electrode. To slow the diffusion of EPS and bacteria from the carbon felt during electropolymerization, 20 mL of melted 1% agarose in M9 medium was added to each well. A carbon felt electrode square was then placed in the center of each well together and a titanium wire was inserted into the carbon felt electrode before the agarose solidified. The Ti wire

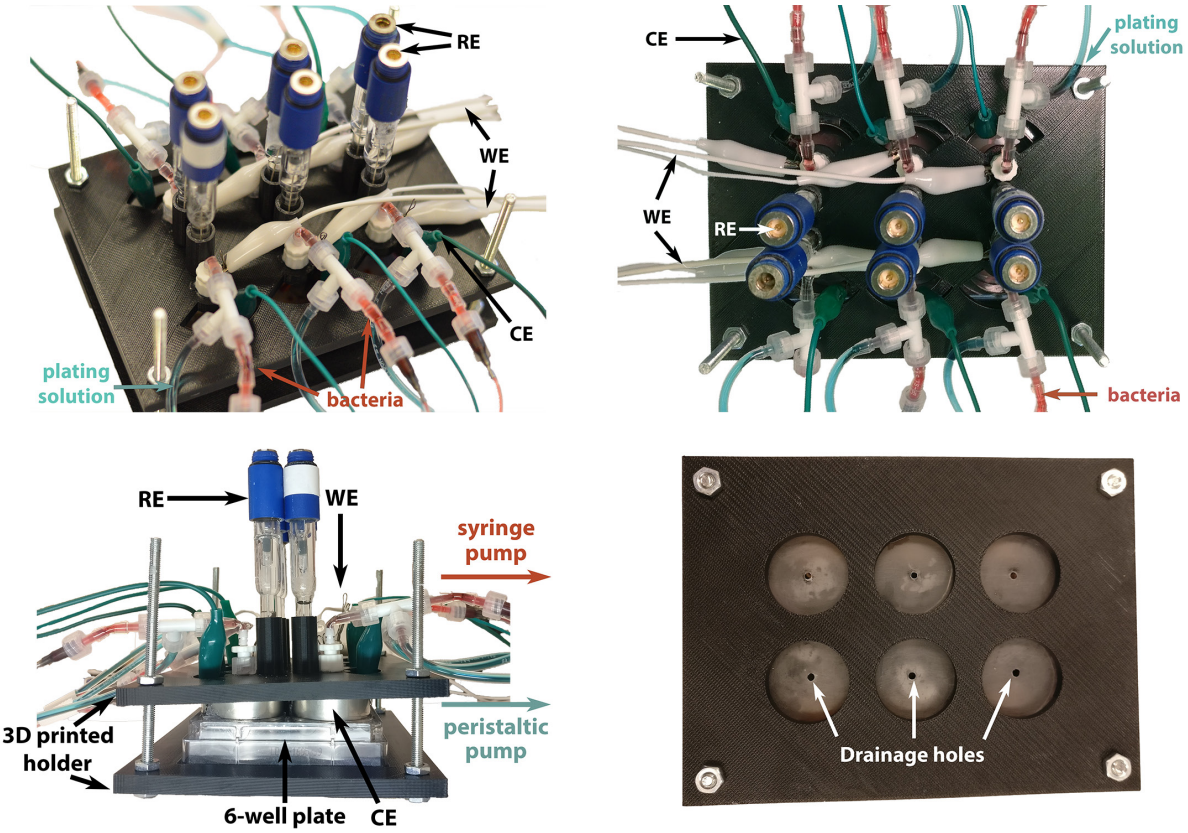

Figure 2.3: Isometric and orthogonal views of the complete MCBF preparation station for parallel electropolymerization of six bio-anodes.

facilitated electrical connection to the potentiostat working electrode channel. After the agarose hardened around the CF electrode, a circular plug was removed from the agarose up to the electrode using a 4 mm biopsy punch connected to an aspirator. The plug removal left behind a small fluid reservoir above the CF enabling EPS to be directly introduced to the surface of the CF electrode. To promote drainage, a second hole was removed from the backside of the electrodes using a 2 mm biopsy punch connected to an aspirator. Finally, an Ag/AgCl reference electrode was held in contact with the agarose/M9 gel of each well, held into place by the custom stage.

A peristaltic pump was used to continuously introduce of fresh EPS during the overnight electropolymerization procedure. Each well had an independent line running to it from the central EPS reservoir. After priming the lines, the flow rate was set to 1.5 mL/hour to slowly introduce new EPS to the reservoir directly above each electrode. A separate line was used to introduce the bacteria into a fluidic T-junction near the wells for mixing and to minimize time in contact with monomer EDOT. A multi-syringe pump was used to deliver the bacteria to the fluidic T-junction, set to an infusion rate of $100\,\mu L\,h^{-1}$. The large discrepancy in flow

rates between the EPS and bacterial suspension ensured a high PEDOT-to-bacteria ratio as well as facilitated fluid mixing in the T-junction.

Once flow was established, a potentiostat set to chronoamperometry mode was used to energize the working carbon felt electrode to 1.0 V versus the reference. The current was recorded as the electropolymerization proceeded for 12—18 hours, and typically deposited over 1500 mC cm^{-3}. When the electropolymerization was completed, the electrodes were disconnected, and the modified anode was cut out of the agarose with a scalpel. Excess agarose gel was removed from the sides of the anode, leaving behind an agarose shell approximately 2 mm thick to improve the mechanical stability of the prepared electrode.

2.3.4 Viability assays

To test the toxicity of EDOT monomer, *S. oneidensis* was grown to $OD_{600} = 1.0$, washed and resuspended in M9, then resuspended in either plain M9 or M9 with 10 mM EDOT added. Colony forming units (CFUs) were measured from each sample using a plated dilution series taken just after preparation and after incubation at 4 °C for 16 hours.

Immediately after electropolymerization, live/dead analysis was performed on randomly selected MCBF samples. The anode was removed from the agarose well, and the excess agarose was removed by careful shaving with a scalpel. The anode was cut in two by a razor blade, and each half was gently washed with M9 medium to remove EPS and unbound bacteria. The samples were then immersed in 1.0 mL of M9 in a microcentrifuge tube. One of these tubes was submerged into a water bath at 70 °C for 15 minutes to heat-kill the bacteria, while the other tube remained at room temperature. Once the heat treatment was complete, the samples were moved to a glass-bottom 6-well plate (Mattek Corporation, P06g-1.5-20-F) for staining and subsequent imaging.

A LIVE/DEAD® BacLight™ Bacterial Viability Kit (Thermo Fisher Scientific, Product number L13152) was used to stain the bacterial films attached to the anodes. SYTO 9 dye and propidium iodide were both added to M9 to 10 µM and 60 µM, respectively. Then, 1 mL of the mixed dye solution was pipetted onto each sample and incubated in the dark at room temperature for 15 minutes. Fluorescent images were acquired on a Zeiss LSM710 confocal microscope with an Axio Observer Z1. Two objectives were used: a 20x EC Plan-Neofluar objective (NA 0.3) with the pinhole set to 30 µM and a 40x EC Plan-Neofluar objective (NA 0.3) with the pinhole set 30 µM. SYTO 9 labeled all bacteria and was excited with a 488 nm Argon laser, and the emission was detected over the range 493–556 nm (I_{SYTO9}). Propidium iodide labeled only those bacteria with damaged cell membranes, i.e. dead cells, and was excited using a 561 nm DPSS laser and its emission was collected between 593–719 nm (I_{PI}). All samples were imaged with the same light intensity and detector gain. The heat-killed samples were used to set the laser intensity, exposure time, and pinhole size threshold for determining whether the bacteria were dead or alive in the test samples.

2.3.5 Electrochemical characterization

Cyclic voltammetry and electrochemical impedance spectroscopy were performed using a BioLogic VMP-300 multipotentiostat. The anodes were scanned in the 6-well plates as described earlier. The anode was scanned from -0.5 V to 0.5 V with a scan rate of 40 mV/sec. Four scans were measured, and the final scan was used to calculate the effective capacitance. Impedance spectra were collected with a stimulus of 10 mV peak-to-peak from 100 kHz to 32 mHz. Electrodes were characterized immediately before electropolymerization. After electropolymerization, the electrodes were gently washed with M9 and characterized again.

2.3.6 Confocal laser scanning microscopy characterization

Slices of the modified anode were gently washed with M9 medium to remove EPS and unbound bacteria and then cut and immersed in 4% (v/v) formaldehyde solution in water. Samples were washed three times with milliQ water and allowed to sit for 5 minutes in milliQ water between each wash. Then, samples were placed in Tissue-Tek O.C.T. Compound (Sakura Finetek USA Inc.) and subsequently immersed in a dry ice ethanol bath for freezing. Samples were stored in a $-80\,^{\circ}\mathrm{C}$ freezer prior to imaging. When samples were ready to be imaged, they were removed from the freezer and allowed to warm while being sectioned into thin slices by a razor blade.

These sections were stained in 14.3 µM DAPI (Thermo Fisher) and 1 µM Cy5 (Thermo Fisher) in M9 medium for 10 minutes. The DAPI stain labeled individual bacteria by their nucleus and the Cy5 provided a nonspecific agarose stain to enhance contrast with the carbon fibers. Each stained section was then placed on a glass coverslip and imaged either with a 20x EC Plan Apochromat objective (0.8 NA) or 63x Plan Apochromat oil immersion objective (1.4 NA). Confocal stacks of the sample were obtained using a 405 nm diode laser to excite DAPI and a 633 nm HeNe laser to excite Cy5, both using a 30 µM wide pinhole. Images were falsely colored to visualize the carbon fibers.

2.3.7 Scanning electron microscopy characterization

Slices of the modified anode were gently washed with M9 medium to remove EPS and unbound bacteria and then cut and immersed in 4% (v/v) formaldehyde solution in water. Samples were washed three times with deionized water and allowed to sit for 5 minutes in deionized water between each wash. Samples were then set into a vacuum desiccator for 48 hours to dry before imaging in the field emission scanning electron microscope. The microscope used was the FESEM Ultra 55 set to an extra high tension voltage level of 2 kV, under vacuum (5.0×10^{-5} mbar), with a working distance of 4–5 mm. Samples were held into place by conductive double-sided adhesive carbon tape (Electron Microscopy Sciences).

2.3.8 Microbial fuel cell setup and biotic current measurement

To compare the performance of MCBFs to native biofilms, a film of *S. oneidensis* MR-1 was grown on the surface of an unmodified CF electrode. A three-electrode single-chamber bioelectrochemical reactor with a 250 mL solution volume was used. Reactors were filled with M9 and autoclaved at 121 °C for 20 min. A CF working electrode, 2.5 cm x 2.5 cm x 0.635 cm was inserted and connected to the potentiostat by a Ti wire threaded along its length. The counter electrode was a segment of Ti wire and the reference was an Ag/AgCl electrode. The potential was kept at 200 mV above the reference with a BioLogic VMP-300 multipotentiostat. The reactor was made anaerobic by continuous sparging of nitrogen gas. Once the reactor was prepared, a concentrated culture of MR-1, grown overnight to a final OD_{600} of 2.0 in 50 mL 2xYT medium (Sigma Aldrich) at 30 °C with 250 rpm shaking, was washed thrice in M9 and injected into the reactor. This culture was maintained for two days at room temperature to allow the bacteria to form a native biofilm on the surface of the unmodified CF. Then, the electrode was removed and gently dipped into M9 to wash unattached cells before starting chronoamperometry and cut to 1.0 cm by 1.0 cm dimensions to be comparable to the MCBF size.

To compare the performance of the MCBF to a native biofilm, chronoamperometric measurements of the anodes were carried out in triplicate in three-electrode single-chamber bioelectrochemical reactors with 140 mL volumes. The working electrode used was either a modified MCBF-CF electrode or a native biofilm on unmodified CF as prepared by the method in the previous paragraph. Bioreactors were continuously purged with nitrogen gas to establish anaerobic conditions, lactate was added to 40 mM, and the reactors were moved to 30 °C. Current was averaged and measured every 30 seconds. At the end of the experiment, the OD_{600} of a sample of supernatant was measured to ensure that no growth or major detachment of biomass occurred during chronoamperometry.

2.4 Results

2.4.1 *S. oneidensis* transfers metabolic current through PEDOT:PSS

The large majority of cells are embedded within the PEDOT:PSS matrix without any direct contact with the CF, as revealed by the SEM investigations. To establish whether or not *S. oneidensis* MR-1 is capable of electron transfer through PEDOT:PSS, we measured the metabolic current transferred to thin PEDOT:PSS films. The PEDOT:PSS was electropolymerized on Au as described in the Experimental methods section and an image of the surface is shown in Figure 2.4. The charge deposited during electropolymerization was $0.206\,\mathrm{mC\,cm^{-2}}$ as shown in Figure 2.5.

Surface profilometry determined that the thickness of the PEDOT:PSS layers varied between 120 to 220 nm. Scanning electron micrographs of the films were taken in order to

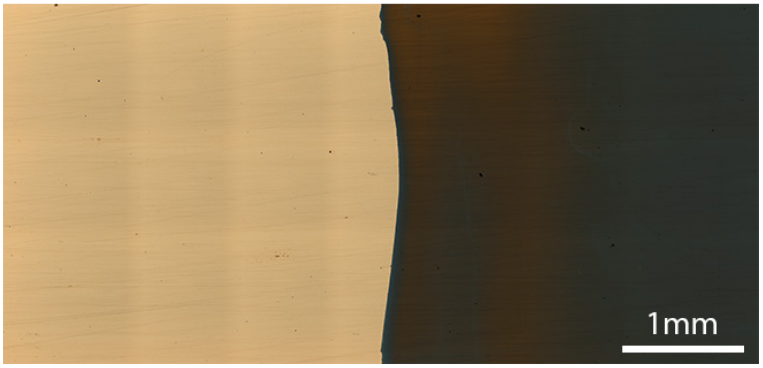

Figure 2.4: Light microscope image of a gold film partially coated with PEDOT:PSS.

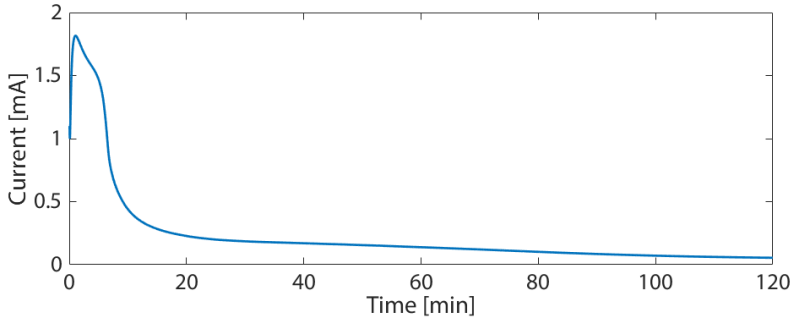

Figure 2.5: A representative electropolymerization current during potentiostatic PEDOT:PSS deposition on a gold thin film.

confirm coverage of the Au surface and are shown in Figure 2.6. The PEDOT:PSS had a bulbous structure that completely covered the smooth Au, meaning that during the bioreactor experiments, all current generated by the bacteria had to be transferred to the potentiostat through the PEDOT:PSS.

To probe the mechanism for electron transfer through PEDOT:PSS, we compared the current produced by three strains: wild type, the riboflavin-deficient mutant Δbfe, and the current-deficient mutant $\Delta mtrB$ on both gold and PEDOT:PSS set to 200 mV versus the Ag/AgCl reference electrode. The results are shown in Figure 2.7. The baseline current just before addition of bacteria was subtracted from the steady-state current produced 12 hours from the injection for comparison as presented in Figure 2.8.

The $\Delta mtrB$ strains did not produce appreciable current above the background, which rules out abiotic current production by PEDOT:PSS or riboflavin. Wild type cultures, which export electron-shuttling riboflavin, transferred 4-fold more current to both gold and PEDOT:PSS than flavin-deficient Δbfe transferred, which is consistent with the knowledge that roughly 70-80% of external electron transfer in *S. oneidensis* MR-1 is flavin-mediated [80]. Roughly 30% more current was transferred through the PEDOT:PSS films, suggesting that

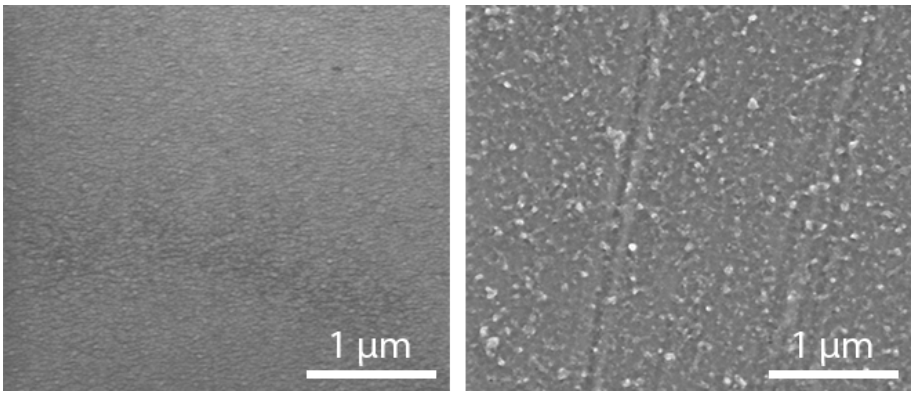

Figure 2.6: PEDOT:PSS completely covers the gold film. (Left) SEM of gold thin film surface and (Right) SEM of PEDOT:PSS film.

the rough structure and higher effective surface area of PEDOT:PSS may enhance external electron transfer. When riboflavin was added to the Δbfe reactors in excess, current sharply rose 36-fold on gold and 87-fold on PEDOT:PSS, suggesting that flavin-mediated transfer to PEDOT:PSS is also effective. The ability for *S. oneidensis* MR-1 to transfer current directly to PEDOT:PSS films, with or without riboflavin shuttles, makes PEDOT:PSS a candidate material to use to enhance volumetric current production.

2.4.2 A scalable process for bacteria encapsulation that preserves viability

To improve the volumetric current density produced by whole cell sensors, we sought to develop a method to embed *S. oneidensis* into a three-dimensional matrix of PEDOT:PSS around carbon felt (CF) (Figure 1a). This method needed to meet several key requirements: i) the vast majority of the bacteria must remain viable, ii) each bacterial cell should be connected by conductive material to the CF surface, iii) the matrix must permit rapid ion mobility and small molecule diffusion, and iv) it should permit parallel and reproducible fabrication.

Initial experiments showed that exposure of *S. oneidensis* to 10 mM EDOT for 16 hours at 4 °C reduced the viability to below 50% (Figure 2.9). Therefore, we developed a new electropolymerization protocol that minimized bacterial exposure to EDOT monomer. We used separate reservoirs for the EDOT/PSS precursor solution and bacterial suspension, pumped them so that they mixed in a T-junction just before their introduction to the preparation well, and allowed excess non-polymerized solution to exit this well through a small drainage hole. Additionally, we carried out the electropolymerization at 4 °C to keep the bacteria in a dormant state. These precautions were taken to maximize bacterial viability throughout the extended electropolymerization process.

To ensure PEDOT:PSS was electropolymerized around each cell sufficiently while simul-

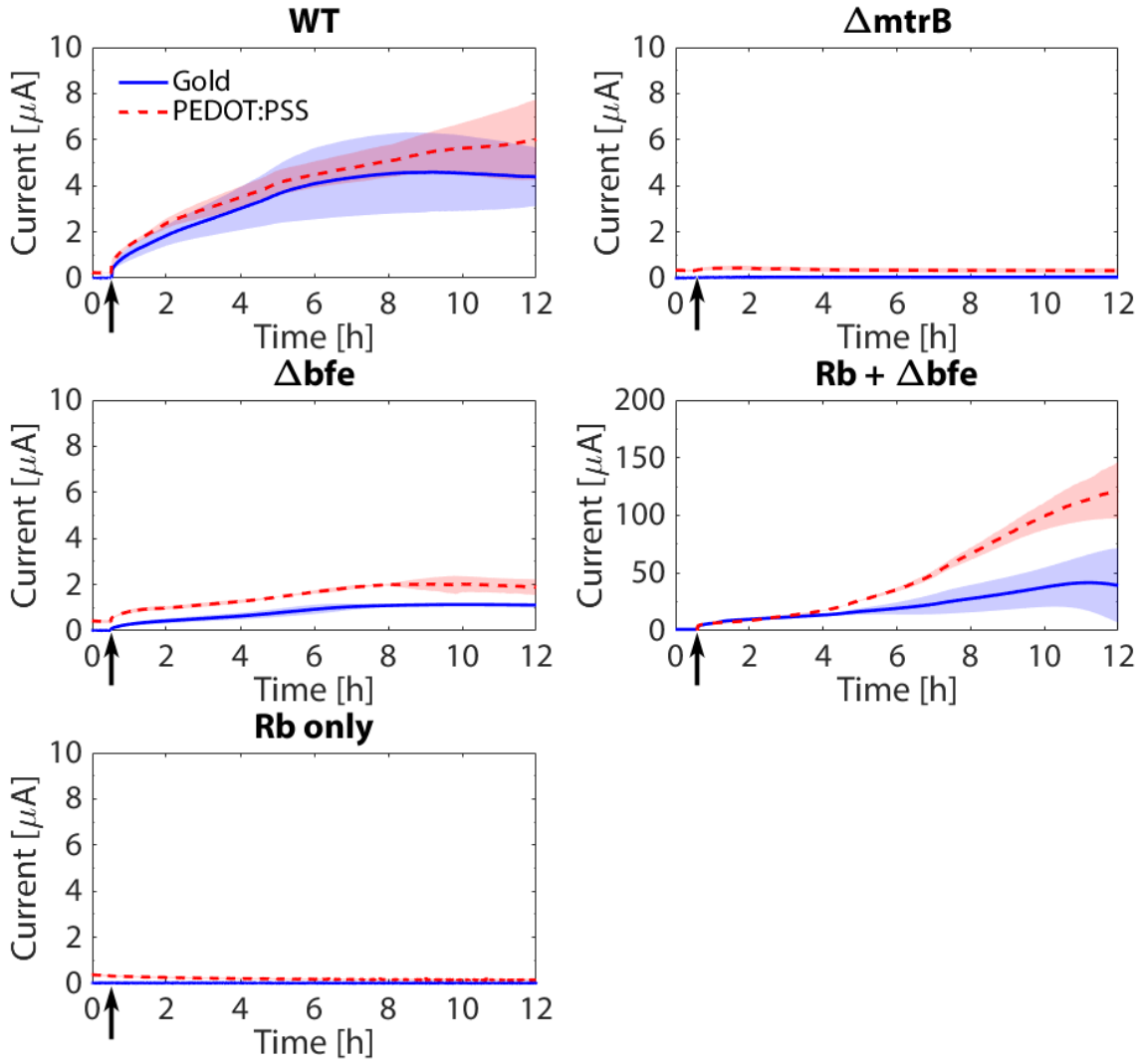

Figure 2.7: *S. oneidensis* transfers current to PEDOT:PSS directly and through riboflavin-mediated electron transfer. Chronoamperometric characterization of MESs based on MCBF (red) and UCF (blue) using *S. oneidensis* (wild type, Δ*mtrB*, and Δ*bfe*) metabolizing lactate. Riboflavin (Rb) was added to the Δ*bfe* reactor and another reactor without bacteria. Light red and blue colored bands indicate the standard deviation in current from two bioreactors, respectively. Arrows denote the addition of bacteria (WT, Δ*mtrB*, and Δ*bfe*) or Rb (Rb + Δ*bfe* and Rb only).

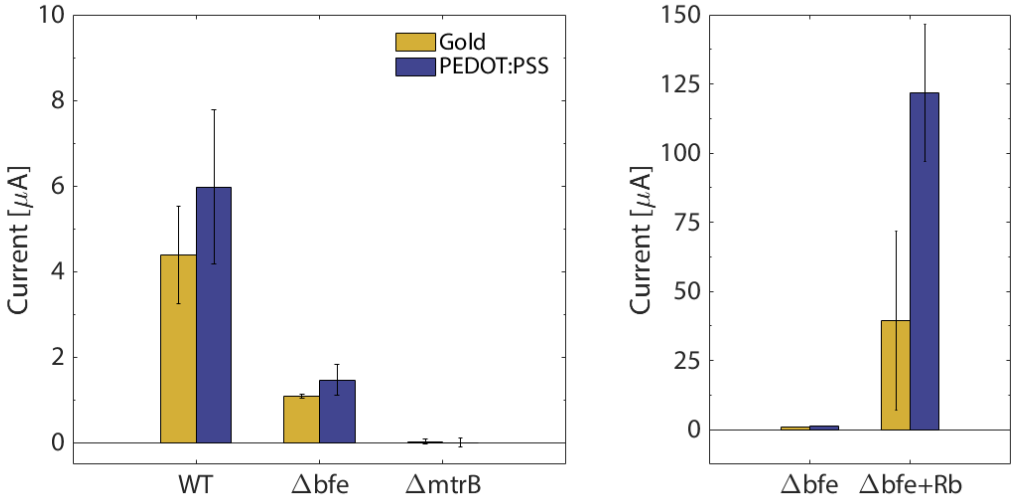

Figure 2.8: (Left) Average current after 12 hours for wild type, Δ*mtrB* and Δ*bfe* strains on gold and PEDOT:PSS films, and (Right) the Δ*bfe* current production before 12 hours after addition of 10 µM riboflavin. The error bars denote standard deviation.

taneously confining the bacteria to the CF surface, we introduced a concentrated mixture of EDOT/PSS solution and bacteria directly to the anode. More specifically, the electropolymerization solution was introduced at a volumetric flow rate 15 times higher than that of the bacterial solution. As a result, a large volumetric charge of 1562 mC cm^{-3} was delivered during the electropolymerization process as shown in Figure 2.10, corresponding to the oxidation of EDOT and the subsequent formation to PEDOT, as well as to the charge doping of PEDOT [81]. A permeable agarose gel surrounding the CF slowed diffusion, confining both bacteria and the electropolymerization solution to the CF during electropolymerization.

Lastly, to make the modification process more scalable, we built an MCBF preparation station (Figure 2.3) capable of simultaneously producing six MCBFs with equal flow-and deposition rates. As a control, bacteria can be omitted and PEDOT:PSS electropolymerized around the CF, resulting in an abiotic multilayer conductive film (MCF). Our setup is a step towards a platform that scalably fabricates multiple bio-anodes for MESs. The end result of the electropolymerization process was a set of functional electrodes consisting of *S. oneidensis* embedded in a PEDOT:PSS-covered CF bulk, the whole electrode being encircled by a 2 mm-thick layer of agarose gel for mechanical support.

2.4.3 Electropolymerization yields viable bacteria encapsulated in MCBFs

To probe the viability of the bacterial cells embedded in the MCBFs, we sliced the MCBF with a scalpel immediately after the electropolymerization process and performed a live/dead

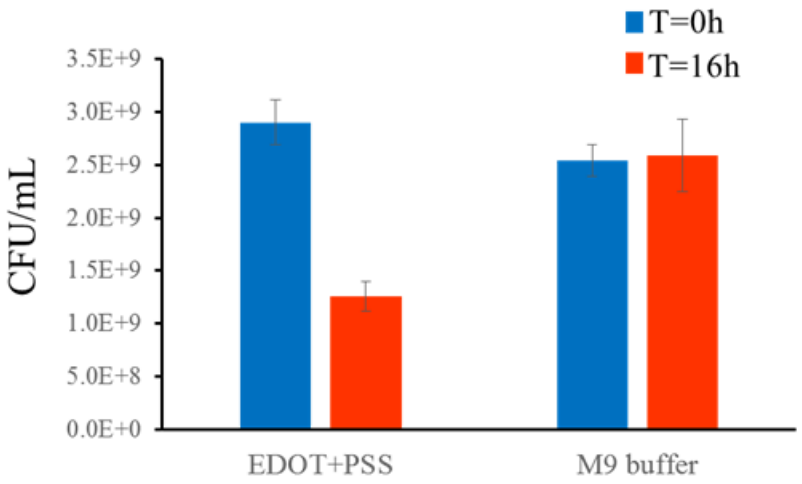

Figure 2.9: Prolonged 10 mM EDOT monomer exposure reduces *S. oneidensis* MR-1 viability. Colony forming units (CFUs) measured before and after 16 hours of exposure to EDOT/PSS precursor and M9 buffer at 4 °C.

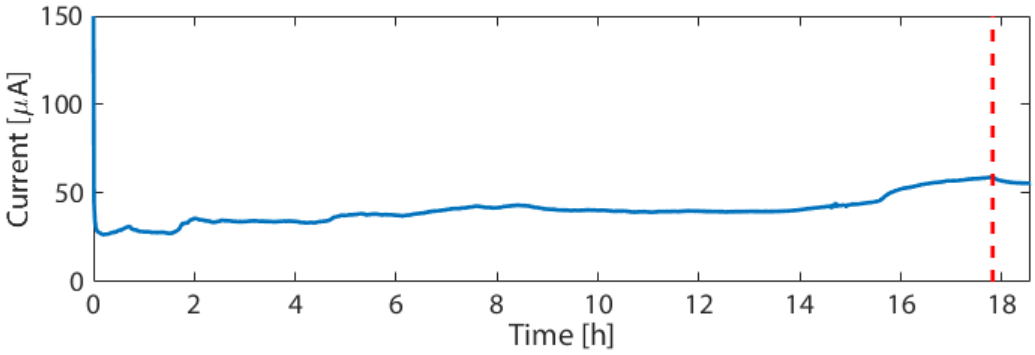

Figure 2.10: A representative electropolymerization current during potentiostatic PEDOT:PSS deposition during MCBF preparation. The dashed red line denotes when the flow of fresh electropolymerization solution was halted.

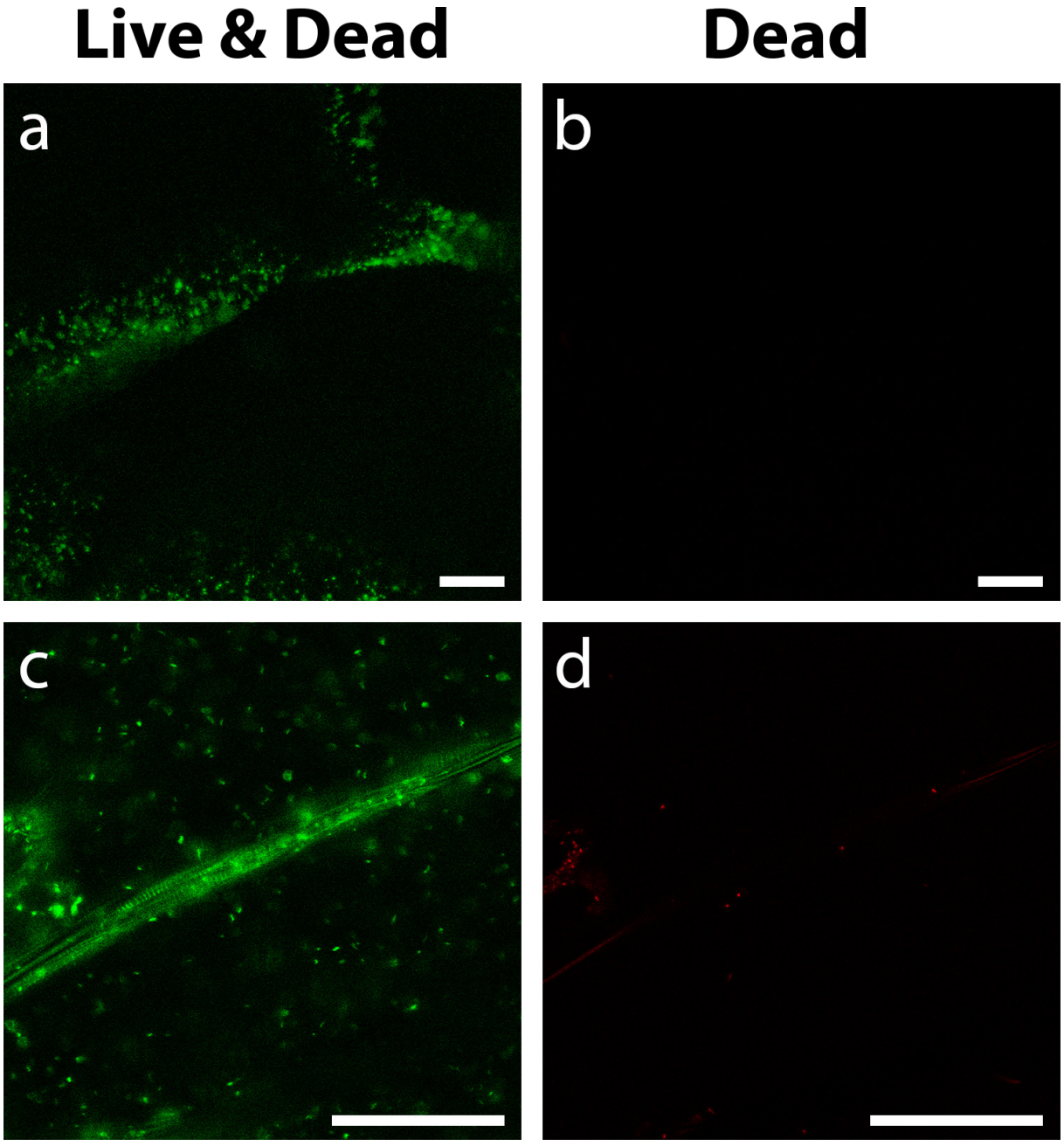

Figure 2.11: *S. oneidensis* MR-1 is viable after incorporation into MCBFs. Confocal microscopy images of a cross-sectioned MCBF stained by a live/dead assay at 20x magnification (a, b) and 40x magnification (c, d). Green fluorescence labels all bacteria (live and dead), red fluorescence labels only dead cells. Scale bars are 50 µm.

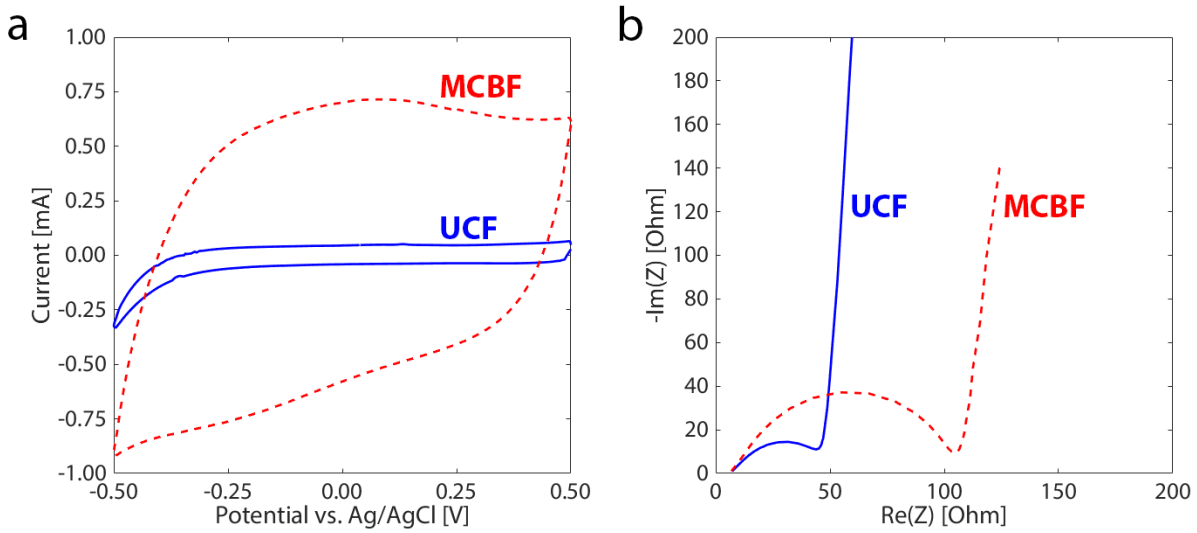

Figure 2.12: Electropolymerization greatly increases the specific capacitance in MCBFs relative to UCFs. (a) Cyclic voltammograms and (b) Nyquist plots measured for unmodified CF before (blue), and for MCBF after the electropolymerization process (dotted red).

viability stain as shown in Figure 2.11. The bacterial viability at this stage was 91% ± 5% across three biological replicates. Thus, the PEDOT:PSS electropolymerization method preserves high bacterial viability, meeting the first key requirement for the MCBF structure. We suggest that limiting the exposure of *S. oneidensis* to EDOT monomer increased overall viability from 50% to over 90%.

2.4.4 Electropolymerization increases the electrochemically active volume

Our electropolymerization process was designed to generate a large electrochemically active volume on the bio-electrode. To estimate the electrochemically active surface area, we used cyclic voltammetry (CV) to measure the capacitive current of untreated CF anodes (UCFs), abiotic multilayer conductive films (MCFs), and MCBFs, each with the same approximate volume of 0.635 cm^3. The UCF had a capacitive current (Figure 2.12a) corresponding to a calculated volumetric capacitance of 1.75 $mF\,cm^{-3}$, indicative of surface-only electroactivity. To estimate the change in double layer capacitance and effective surface area resulting from the electropolymerization process, cyclic voltammetry (CV) was performed. The capacitance was estimated from the CV by the following formula adapted from other studies [82]–[85]:

$$C_v = \frac{\frac{1}{2}\oint i d\psi}{\nu \Delta\psi}\frac{1}{V} \tag{2.1}$$

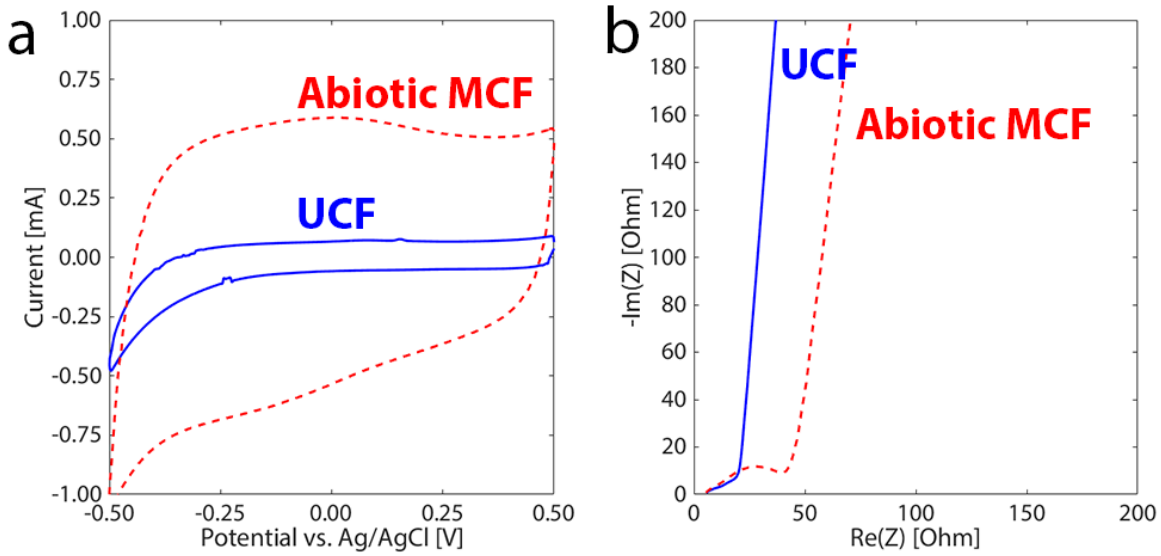

Figure 2.13: (a) Cyclic voltammograms and (b) Nyquist plots measured for unmodified CF before (blue), and for abiotic MCF after (dotted red) the electropolymerization process.

In Equation (2.1), C_v is the volumetric capacitance [F cm^{-3}], i is the current [A], ν is the scan rate [V/s], ψ is the potential [V], and Vis electrode volume [cm^3]. This equation estimates the capacitance by computing the average charge stored by the double layer capacitance throughout one full cycle of the CV, dividing by the potential window ($\Delta\psi$), and normalizing the result to the electrode volume. The electrode volume used in this study was 0.635 cm^3.

In contrast, both the abiotic MCF and MCBF samples featured significantly higher CV currents (Figures 2.12a and 2.13 after electropolymerization, corresponding to representative volumetric capacitances of 19.21 and 20.37 mF cm^{-3}, respectively. This 11-fold increase in volumetric capacitance is consistent with the formation of a thick PEDOT:PSS layer with high PSS contents on the UCF surfaces and in the voids between individual fibers, where the high PSS to PEDOT contents can be derived from the volumetric capacitance value of PEDOT [86], [87]. Indeed, high capacitive currents are typical for thick PEDOT:PSS-based electrodes due to the mixed electronic-ionic conduction of PEDOT:PSS films [72], [88]. Moreover, the almost negligible difference between the volumetric capacitance values of MCF and MCBF indicate that the presence of bacteria did not influence the electrochemically active surface area.

An ideal anode would have a very low charge transfer resistance (R_{CT}) to ensure good electron transfer. To determine R_{CT} values, we performed electrochemical impedance spectroscopy (EIS) on the same samples analyzed by CV. We note that the trends in EIS data before and after electropolymerization did not differ between MCBFs and MCFs (Figure 2.13) therefore, the effect of bacteria on these data is not considered here. The Nyquist plot

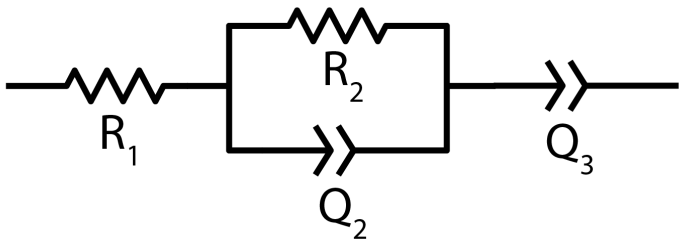

Figure 2.14: Equivalent circuit used to model the interfaces measured by EIS.

Table 2.2: Parameters from EIS spectra fit to equivalent circuit model.

Parameter	**Units**	**Before Modification**	**After Modification**
R_1	Ω	6.99	6.9
R_2	Ω	42.72	102.7
Q_2	$F\ s^{(\alpha-1)}$	1.188×10^{-4}	5.855×10^{-5}
α_2	-	0.683	0.743
Q_3	$F\ s^{(\alpha-1)}$	8.345×10^{-4}	1.040×10^{-2}
α_3	-	0.965	0.94

of a UCF shows the typical semicircle and tail indicative of both capacitive and resistive contributions to the impedance (Figure 2.12b).

To determine the effective resistance change of the anode after electropolymerization, EIS spectra were measured from 100 kHz to 32 mHz with a stimulus amplitude of 10 mV. Four data points were averaged for each frequency collected. Figure 2.14 shows the equivalent circuit used to fit the spectra both before and after electropolymerization.

The element R_1 models the solution resistance, R_2 and Q_2 model the anode-solution interface, and Q_3 models the low frequency behavior of the interface. Q_2 and Q_3 are modeled as constant phase elements (CPEs) with electrical impedance given by equation 1.7. The equivalent circuit model was fit to the EIS spectra using the ZFit functionality of BioLogic's EC-Lab Express software. The built-in randomized simplex optimization was used with 20000 iterations and randomization. The resulting parameter values fit to the representative sample are shown in Table 2.2. In Figure 2.15, a Bode plot of the experimental impedances are plotted alongside these fits. From this plot, a reasonable fit is observed. The chi-square values for the fits are 0.0227 and 0.0604 for before and after electropolymerization, respectively.

In the case of a representative MCBF, we see an increase in R_{CT} from 43 to 103 Ω. This small increase in R_{CT} may indicate a series resistance caused by the incorporation of PEDOT:PSS clusters. In any case, this minor increase in R_{CT} would not affect measured biocurrents with MCBFs for current levels practically achievable in small-volume MESs. Thus, we conclude that the volumetric capacitance of MCBFs increased dramatically related to UCFs while only showing a negligible increase in electrical resistance. Together

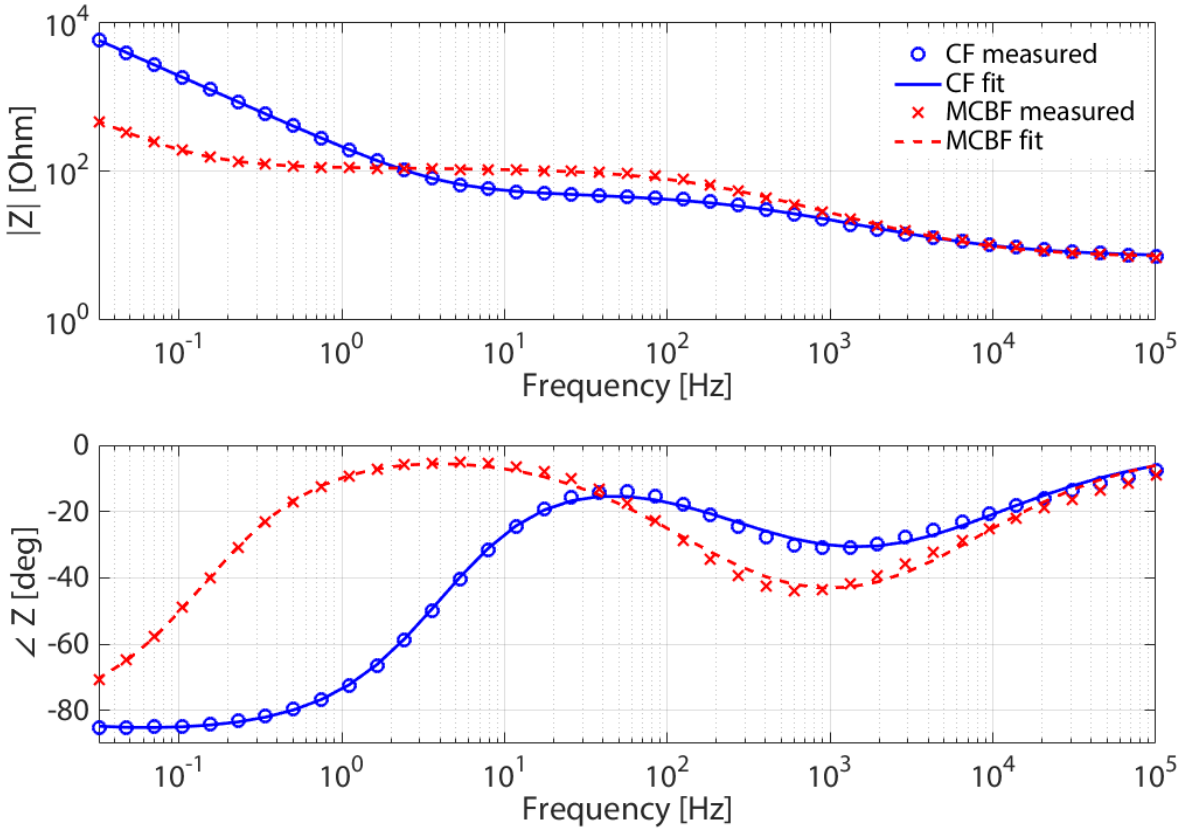

Figure 2.15: Bode plot of EIS spectra and fits before and after electropolymerization.

these properties should ensure a higher biocurrent in MCBF-based MESs compared to those possible to achieve in UCF-MESs.

2.4.5 Electropolymerization embeds a high density of bacteria

To understand how bacteria are embedded inside of the PEDOT:PSS bulk, we examined slices of a UCF with a native biofilm and an MCBF via a confocal microscope. These images reveal that bacteria were covering the UCF fibers with low densities that varied locally (Figure 2.16a,c, bacteria in blue). In addition, the UCF fibers contained large voids which were not filled by bacteria. This limited coverage of the volume by bacteria within the UCF electrode was a result of surface-only monolayer attachment, frequently settling into the deep transverse grooves along the length of each fiber. In contrast, many more bacteria were present in the MCBF, and they were concentrated in large clusters (Figure 2.16b,d). Moreover, the encapsulated bacterial clusters were both on the CF fibers and in the voids between the CF fibers to form high density multilayer bacterial structures up to 80 µm thick as measured on the confocal images as the distance from the carbon fiber to

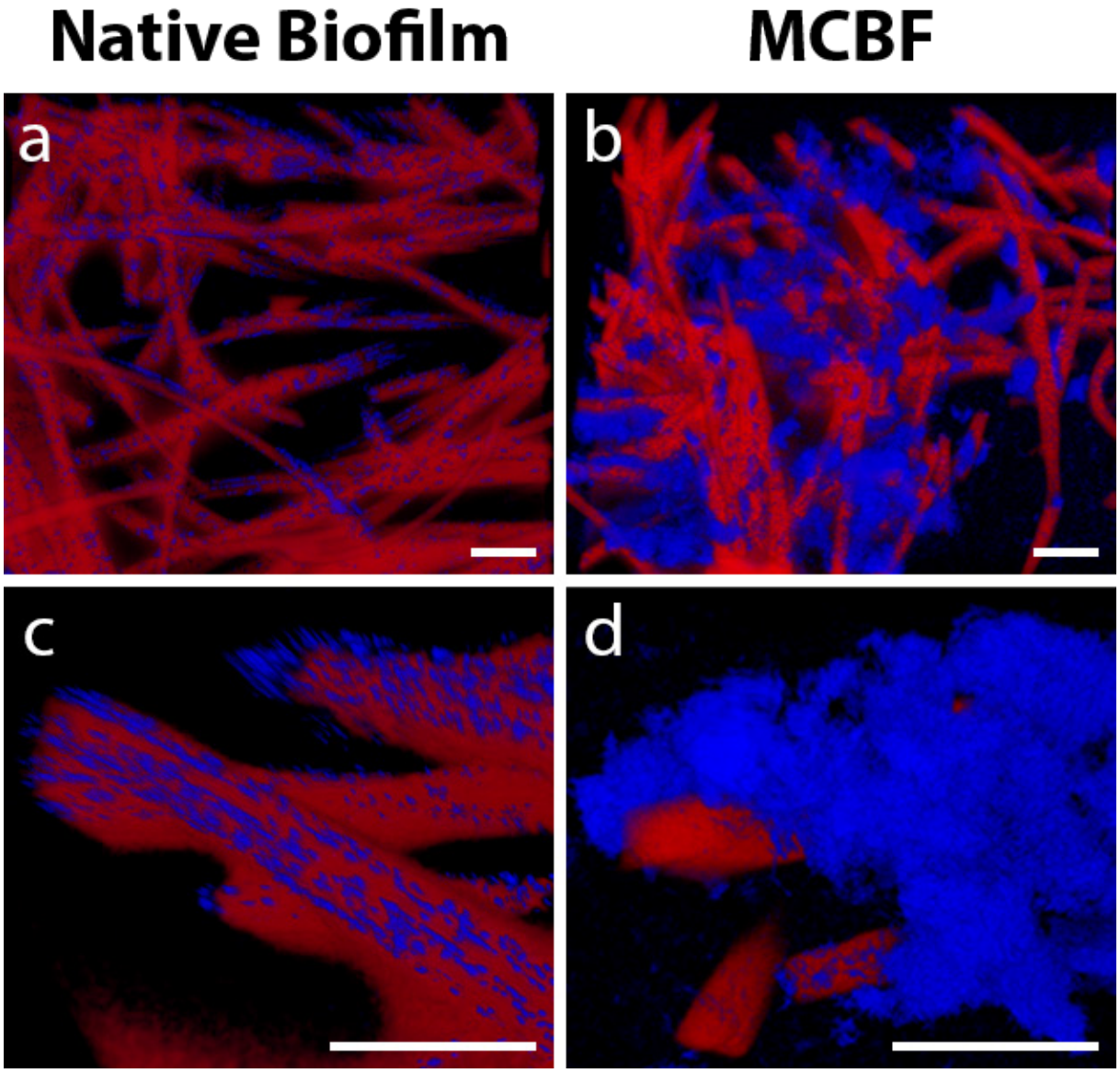

Figure 2.16: Multilayer conductive bacterial films (MCBFs) are thicker than native *S. oneidensis* MR-1 biofilms on unmodified CF (UCF). Confocal microscopy images of cross sections (a and c) of native biofilm on UCF and (b and d) MCBF. Red color indicates CF and blue indicates *S. oneidensis*. Scale bars 50 µm.

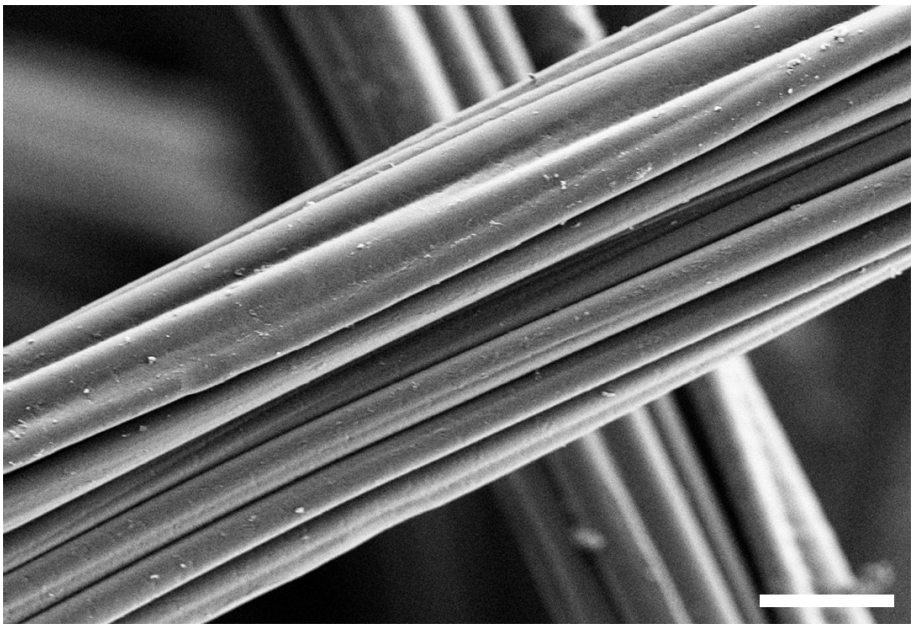

Figure 2.17: Scanning electron micrograph of unmodified carbon fiber. Scale bar is 5 µm.

the point of farthest radial extent on the MCBF structures. Thus, the process described above demonstrates the enclosure of bacteria into a three-dimensional matrix thicker than its native biofilm.

2.4.6 A multilayer bacterial structure is revealed by SEM

To probe the morphology within the multilayer structures on the sub-micron level, we desiccated and sectioned three abiotic MCF and three MCBF electrodes and examined them by scanning electron microscopy. Normally, fibers of UCF are held together in well-separated thick bundles (Figure 2.17). The native biofilm formed by *S. oneidensis* MR-1 on untreated CF shows that the bacteria adhere inside the grooves that run along the length of the fibers (Figure 2.18). In contrast, a close look at an abiotic MCF section reveals smooth solid structures with uniform cross sections stretching between fibers of CF (Figure 2.19a,c). Since the layers do not charge quickly during electron microscopy, we interpret these conductive structures as layers of PEDOT:PSS. Additionally, SEM of the MCBF reveals a porous and rough internal surface replete with rod-shaped cavities that are roughly 1–2 µm in dimension (Figure 2.19b, d). We interpret these cavities as the imprints of embedded bacteria after they dehydrated and shrank during the SEM sample preparation process. The flat, dehydrated *S. oneidensis* MR-1 structures are easily seen on the top surface of the MCBF films and comparable in size to the cavities within the section (Figure 2.19b). Thus, we conclude that bacteria in the MCBF are encapsulated by PEDOT:PSS layers, creating closely positioned, highly integrated, multilayer bacterial films. Consequently, our MCBF preparation process

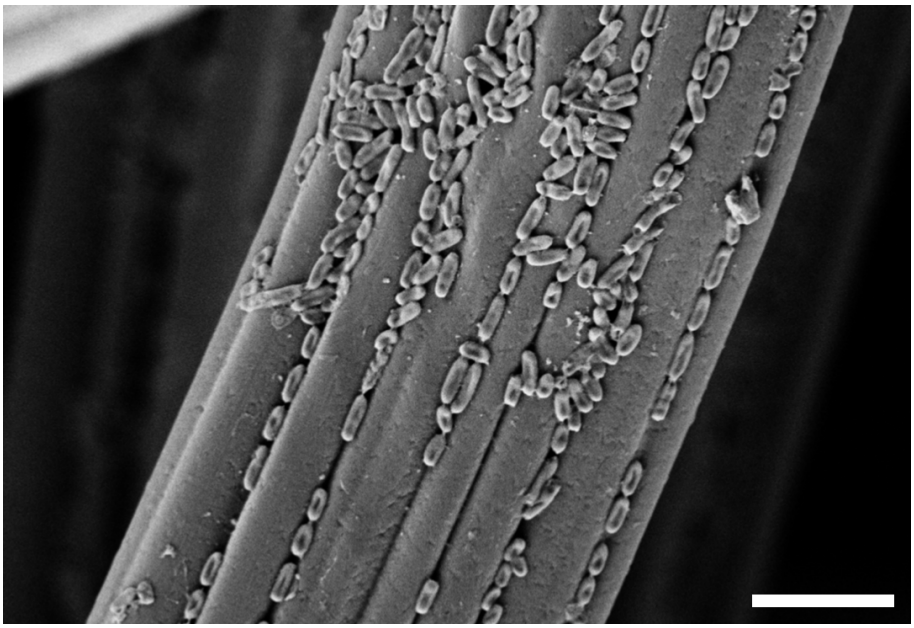

Figure 2.18: Scanning electron micrograph of native *S. oneidensis* MR-1 biofilm on unmodified carbon fiber. Scale bar is 5 µm.

does not only encapsulate high densities of bacteria into a three-dimensional matrix, but also embeds them into a conductive multilayer structure.

2.4.7 PEDOT:PSS electrodeposition increases biotic current

To determine the improvement that our electrode modification process made on overall current output, we tested three samples of each MCBF-and UCF anodes with native biofilm growth, in standard three-electrode MES configurations (MCBF-MES and UCF-MES, respectively). The electrodes under test were poised at constant 200 mV versus the Ag/AgCl reference electrode collecting the current originating from the bacterial electron transfer, while lactate served as the metabolic substrate. Under these conditions, UCF-MES delivered a steady state current of 1.5 µA (Figure 2.20). In contrast, MCBF-MESs produced significantly higher current, with a 20-fold increase at steady state. The evolution of the current in the PEDOT-based bioanode followed a continuous increase with time, peaking between 14 and 15 hours of operation. During this time, there was no significant change in the planktonic bacterial density as measured by OD_{600} which remained under detectable levels after 16 hours in both the MCBF-MESs and UCF-MESs. Furthermore, *S. oneidensis* MR-1, a facultative anaerobe, did not grow aerobically in M9 with lactate at 30 °C with 250 rpm shaking (data not shown), suggesting that under these anaerobic conditions, *S. oneidensis* MR-1 would not grow. Therefore, we attribute the current increase not to bacterial growth, but rather adaptation of MCBF-MESs to anaerobic conditions at 30 °C from its preparation

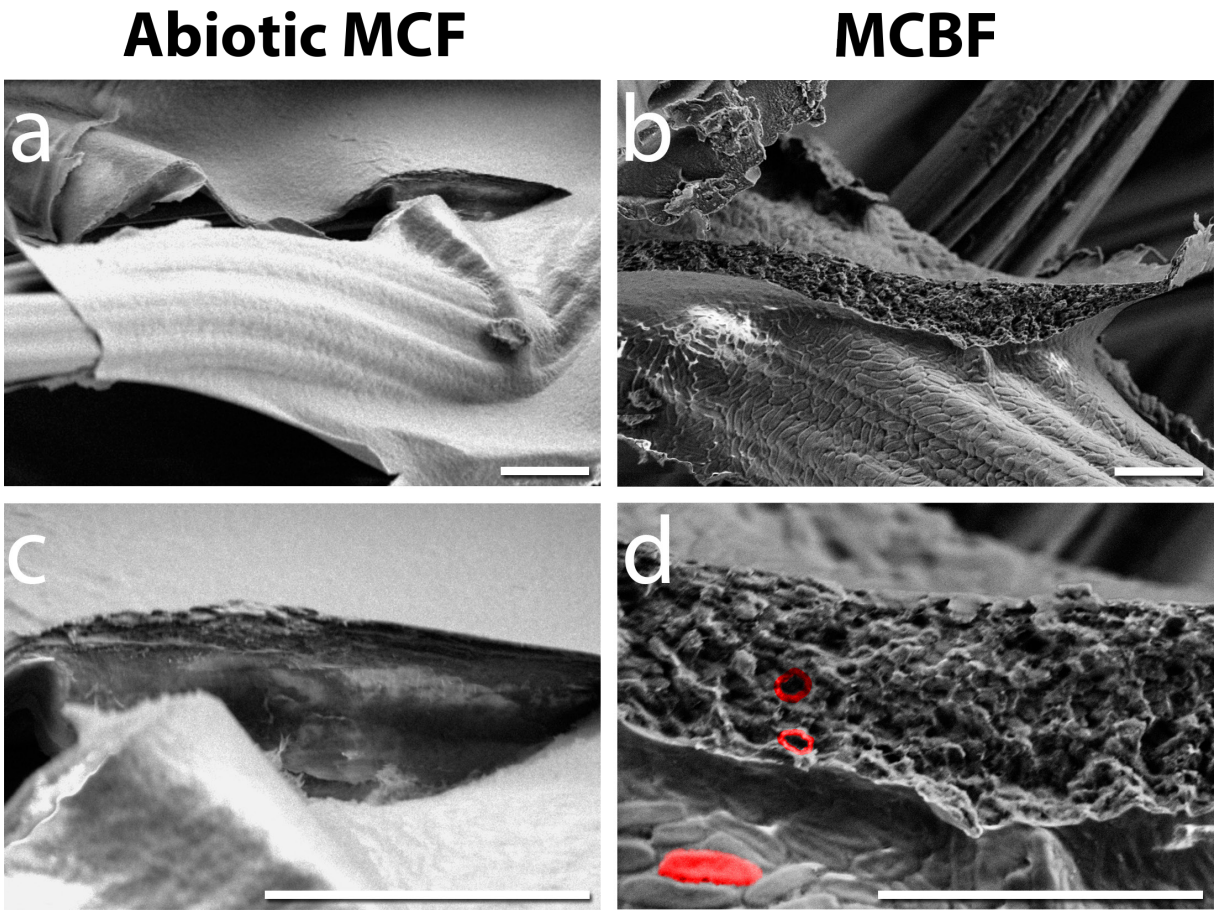

Figure 2.19: Electropolymerization of living *S. oneidensis* MR-1 embeds the bacteria inside a multilayer conductive film. Scanning electron micrographs (SEMs) of a section (a and c) of an abiotic multilayer conductive film (MCF) showing smooth internal surfaces of PEDOT:PSS on CF, and (b and d) of an MCBF showing high density of bacteria within PEDOT:PSS layers, respectively. (d) One bacterium on the external surface of the MCBF is shaded in red, while two bacteria-sized voids internal to the MCBF are outlined in red. Scale bars are 5 µm.

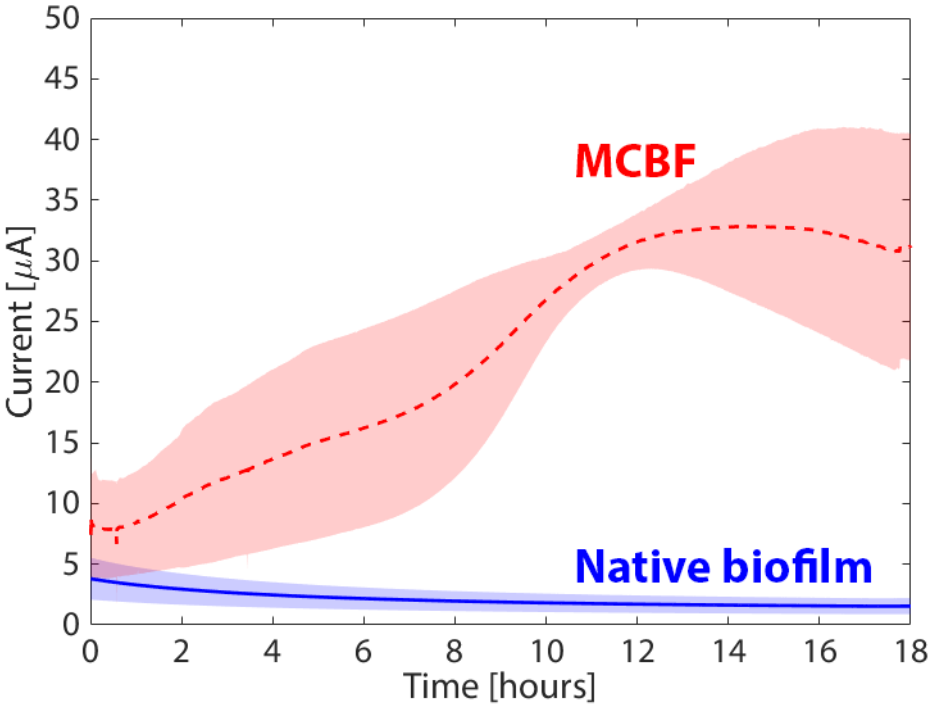

Figure 2.20: MCBF bioreactors produce greater biotic current than those using a native biofilm on unmodified CF. Chronoamperometric characterization of MESs based on MCBF (red) and UCF (blue) using *S. oneidensis* MR-1 metabolizing lactate. Light red and blue colored bands indicate the standard deviation in current from three bioreactors, respectively.

at 4 °C under aerobic conditions. Supporting the above claim, signals measured in native biofilm-based MESs exhibited no increase over time [63], [68]. The slight current decrease observed over time might be explained by the gradual desorption of surface-bound electron-shuttling flavins [89] or detachment of the cells themselves from the CF. The MCBF-MESs produced significantly higher current than CF-MESs with the same macroscopic volumetric form factor. We suggest that this improvement was achieved due to the added high electroactive volume of the PEDOT:PSS conductive matrix and the incorporation of a dense biomass of viable bacteria embedded within this 3D matrix. The MCBF's increased current within the same form factor makes it better suited for deployment in environmental biosensing systems than unmodified CF, since the same compact volume produces a larger current signal.

2.5 Discussion

2.5.1 PEDOT:PSS is a nutrient-permeable conductive scaffold

We have demonstrated a new method for encapsulating electroactive bacteria into dense, multilayer conductive bacterial films (MCBFs) that feature a 20x higher current-per-volume ratio than a native biofilm. We achieved this performance by embedding bacteria into high-density nutrient-permeable conductive multilayer films that allow bacteria from inner layers to contribute to current generation as well as those attached to the outer surface. The scaffold used in our design, PEDOT:PSS, is a material with high molecular permeability, enabling materials as large as 200 Da to readily diffuse through [90], ensuring that lactate (90 Da) and other nutrients would be available to the innermost bacteria. The 20:1 weight ratio of PSS dopant to EDOT used, is expected to yield PEDOT:PSS layers with higher PSS content compared to commercially available formulations [91], ensuring high porosity structures. Furthermore, the large improvement in biocurrent indicates that the electropolymerization process resulted in a high-conductivity percolation network connecting bacteria throughout the multilayer structure with the CF substrate. This conductive path is efficient in collecting electrical charges from bacteria despite the relatively small volume of PEDOT deposited during the process ($0.48\,\mathrm{mm}^3$, calculated based on the ratio of volumetric capacitance gained after electropolymerization, to that of PEDOT [86], [87]). *S. oneidensis* MR-1 is known to secrete riboflavin as an electron shuttle to mediate electron transfer, and as much as 70% of charge transfer in biofilms is flavin-mediated [92]. By surrounding bacteria by conductive material, we constrain flavin shuttling to short distances to further enhance electron transfer rate, thereby reducing its diffusion limitation. Additionally, parallel preparation of multiple anodes is possible with the MCBF preparation station, and viability of bacteria is preserved by the process. These characteristics are vital to increase current production beyond superficial electron transfer to volumetric current production throughout the film.

The 20x improvement of steady-state current production by the MCBF over the native biofilm suggests that the bacteria embedded throughout the film are contributing to current production, and that electrons are conducted through PEDOT:PSS to the CF substrate. Evidence of direct electron transfer to PEDOT:PSS makes this more likely, since the internal bacteria are surrounded by a conductive matrix that transfers their electrons to the CF substrate. In fact, *S. oneidensis* MR-1 could transfer electrons equally well to PEDOT:PSS as gold films, with or without riboflavin export. This means that the conductive PEDOT:PSS matrix does not necessarily need to be permeable to riboflavin, which is a relatively large molecule (376 Da), since internal bacteria can perform direct external electron transfer to PEDOT:PSS. The flexibility of PEDOT:PSS to accept both direct electron transfer and electron shuttles makes it well-suited for use with other bacterial species.

2.5.2 Comparing the MCBF to prior art

Our method extends prior work to build a thick bacterial film, resulting in a high volumetric current density without reliance on a native biofilm for adhesion to the anode. The most commonly used electroactive bacterial species, *S. oneidensis* and *Geobacter sulfurreducens*, produce biofilms of a monolayer thickness [69] and up to 50 µm thick [61], respectively, when grown anaerobically on CF electrodes. A recent strategy increased current production by enhancing native biofilm conductivity by either encapsulation of bacteria by conductive polymers [68] or incorporation of Au nanoparticles [63], then allowing the bacteria to form a biofilm. These studies report increases of current density between 1.4-fold to 4.8-fold over the native biofilm. Our method is unique in that it does not rely on biofilm formation, instead depositing a high-density film onto CF, allowing us to use species that do not produce robust biofilms. Moreover, the films we produce are up to 80 µm thick in places, and our electropolymerization preparation method has easily modifiable parameters, such as EPS and bacterial suspension flow rates, substrate material, and polymerization potential, allowing for further optimization to control film morphology. It is also noteworthy that the MCBF structures can be formed significantly faster compared to methods utilizing the growth of native biofilms (hours versus days, respectively), further increasing the time efficiency of the process. Finally, the materials are more cost efficient for large-scale production than methods using precious metals [63], [64].

2.5.3 Applications of the MCBF to environmental sensing

The high volumetric current density offered by this new fabrication method will open new opportunities to further miniaturize portable MES platforms for environmental biosensing. Due to the tight encapsulation of bacteria by PEDOT:PSS in the MCBFs, cell detachment from the electrode surface has been minimized, preventing performance loss over extended operations. In addition, the agarose gel outer layer of the anode defines a solid structure that can be further enclosed by other methods to exclude any foreign competing microbes entering the sensing platform, while remaining permeable to analytes of interest. For example, a recently reported portable bioelectronic sensing system (BESSY) [42], [93] uses a micrometer-thick porous silica membrane to exclude foreign microbes and prevent environmental contamination. The BESSY anode uses a mixed conductive agarose matrix blended with *S. oneidensis* and shredded carbon fiber 2.0 cm^3 in volume, but only produces a baseline signal level of 6.31 µA cm^{-3}, whereas the MCBF achieves 32.87 µA cm^{-3}. Therefore, the MCBF would offer the same SNR if it were reduced to a volume of 0.38 cm^3, a 5.2x reduction in anode volume from BESSY. Further optimization of the MCBF preparation process to increase the current density by another order of magnitude, by adjusting bacterial density, scaffold material, electropolymerization conditions, or other parameters, could someday enable millimeter-scale microbial reactors, reducing power consumption to enable persistent environmental sensing.

2.6 Conclusions

In this chapter we presented a functional multilayer bacteria-PEDOT:PSS-CF-agarose electrode that can electrically interface with bacteria regardless of their ability to form biofilms. This hybrid anode produces 20-fold higher current density compared to standard porous CF-based MESs employing *S. oneidensis* MR-1 in steady state operation. The presented method opens the door to miniaturized, field-deployable MESs for biosensing and energy production. Despite this advance, most bacteria-based biosensors that feature an amperometric output are slow to respond due to their reliance on transcription and translation processes. A sensor that can detect a faster biological response is still desired.

Chapter 3

Drawing inference from flagellar observation

The content of this chapter was adapted with permission from the following papers:

- "Probing the dynamics of the proton-motive force in *E. coli*" by T.J. Zajdel, M.A. TerAvest, B. Rad, C.M. Ajo-Franklin, and M.M. Maharbiz [94]
- "Applying machine learning to the flagellar motor for biosensing" by T.J. Zajdel, A. Nam, J. Yuan, V.R. Shirsat, B. Rad, and M.M. Maharbiz [95]

3.1 Prelude: Observing the experts

Bacterial chemotaxis is *fast*. Since the bacterium has to make real-time decisions to bias its movement towards nutrients, chemotaxis uses rapid kinase-based signaling for signal transduction. Despite the high speed and sensitivity inherent in chemotaxis, no engineered system approaches the same performance with the volume of a cell. In this chapter, we will review the extensively analyzed chemotaxis system in *Escherichia coli*. We will then present a preliminary study that aims to draw inference from observed motor behavior.

The primary question motivating the technique presented in this chapter is "*How many bacteria must be observed to make a conclusion about their environment?*" Individual bacteria have differing characteristics due to stochastic variations in gene expression, so a single cell cannot speak for an entire population. On the other hand, observation of a large population in aggregate discards important differences between individual cells. The ideal case is to take a single cell measurement for enough individual bacteria to deal with natural variations. In this study, we do exactly this by observing the motor response of many bacteria responding to chemoattractants under microscope observation.

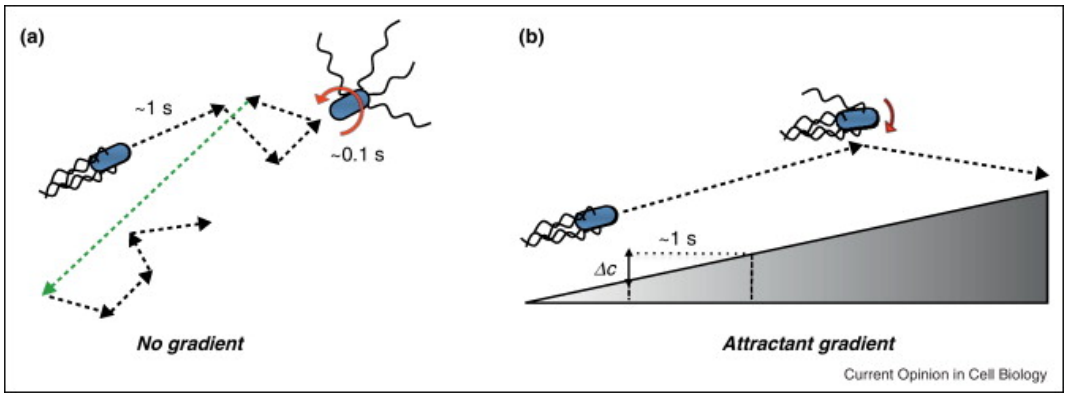

Figure 3.1: Bacterial chemotaxis in *E. coli*. (a) Run and tumble swimming in the absence of a chemical gradient leads to foraging in the environment. (b) In the presence of a chemical gradient, runs are biased in the direction of the gradient. Reproduced with permission from Sourjik and Wingreen [96].

3.2 Bacterial chemotaxis

The chemotaxis pathway in *E. coli* and other bacteria is the most studied sensory pathway in prokaryotes, with an epic arch of work that reaches back over three centuries [97]. Chemotaxis is remarkably fast; large step changes in the chemoattractant L-serine affect motility within 300 ms [36]. Chemotaxis is also sensitive; the detection limit for the chemoattractant L-aspartate is 3.2 nM, which given the cell volume of 1 fL, corresponds to the detection of 3 molecules [29]. This balance places chemotaxis near the fundamental Berg-Purcell limit for the ideal biosensor (Section 1.3.2).

E. coli motility follows a random walk pattern, alternating between straight "runs" (1 second on average) and randomly reorienting "tumbles" (0.1 seconds on average). In the absence of any stimulus, the bacterium will forage the space surrounding it, monitoring its chemoreceptors as it runs and tumbles. If the cell begins to detect an increase in chemoattractant, as one would in the presence of a chemical gradient, it will bias the lengths of its runs to climb the chemical gradient. In this way, bacteria can direct their motion towards nutrients, also known as chemoattractants. In the same way, bacteria can adjust their tumbling frequency to move away from so-called chemorepellents.

The remainder of this section will review each component of the chemotaxis system, identifying opportunities for biosensing along the way:

1. Bacterial flagellar motor
2. Chemoreceptors
3. Biochemical processing network
4. Proton-motive force

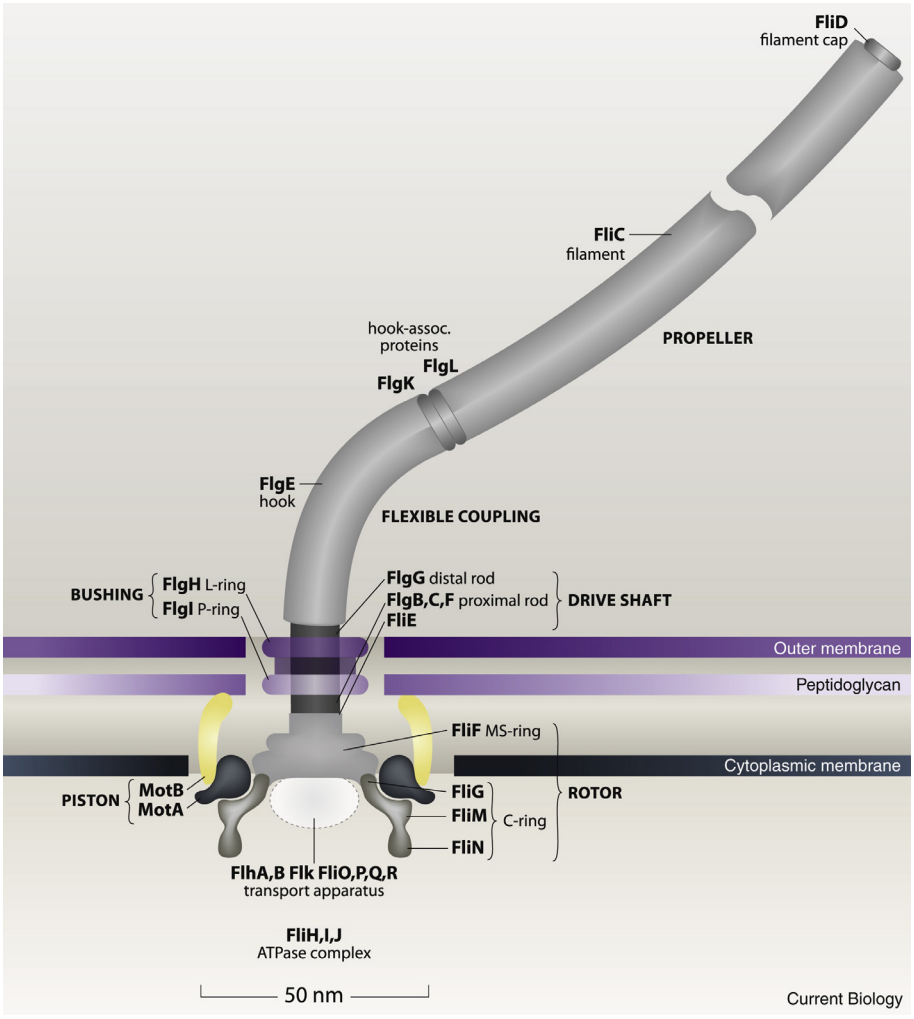

Figure 3.2: The flagellar motor of *E. coli*. Reproduced from Berg [99] with permission.

3.2.1 Bacterial flagellar motor

The bacterial flagellar motor is the actuator for locomotion in *E. coli* and [9] its movement is the output of the chemotaxis pathway. It is one of the smallest rotary motors known to science, with a diameter of about 50 nm [98], [99]. The motor consists of the basal body, hook, and flagellum, which serve as the motor, joint, and filament, respectively [100] as illustrated in Figure 3.2.

The motor drives a whip-like filament called the flagellum at up to 300 Hz [101]. *E. coli* is peritrichously flagellated, meaning that its multiple flagella are distributed around its entire surface [102]. The number of flagella per cell varies with growth conditions, but it is typically in the range of 6–8 per cell. The translocation of protons through stator protein MotA generates torque through electrostatic interactions between amino acid side chains

Table 3.1: Chemotaxis receptors used by *E. coli*.

Receptor	**Target**	**References**
Tar	aspartate, other amino acids, maltose	[122]–[124]
Tsr	serine, other amino acids	[122], [124], [125]
Tap	dipeptides, pyrimidines	[126], [127]
Trg	ribose, galactose	[126], [128]
Aer	oxygen, redox state	[129], [130]

[103], driven by the proton-motive force [104] (Section 3.2.4). The motor's stall torque is approximately $1260\,\mathrm{pN}\cdot\mathrm{nm}$ [105]. The motor either rotates clockwise or counter-clockwise, and its direction is under the control of the chemotaxis biochemical network (Section 3.2.3) [9], [98].

When these filaments all rotate together in the counter-clockwise direction, the flagella bundle together due to hydrodynamic forces and the cell travels forward in a run. If any single motor changes direction, the filaments splay apart and a tumble begins [106]. Due to spatial correlation among signaling molecules inside the cell, multiple flagella often switch simultaneously, making swimming behavior robust against variations in flagellar number [107]. Therefore, tracking the rotation of a cell body tethered by a single flagellum, as in Block et al. [108], provides substantial information about the cell's overall trajectory.

3.2.2 Chemoreceptors

E. coli has five different receptors that feed into its biochemical chemotaxis network: Tar, Tsr, Tap, Trg, and Aer (Figure 3.3, Table 3.1) [109], [110]. These are the known methyl-accepting proteins (MCPs) in *E. coli* and provide the primary senses for the real-time chemotaxis response. These receptors are organized in clusters [111]–[113] and inter-receptor communication among these receptor teams lead to signal amplification [114]–[117], broaden responses to a broad range of stimuli [118], [119], and facilitate the adaptation response [120].

The ligand-binding MCPs Tsr, Tar, Trg, and Tap have the same basic structure. Each MCP spans the inner membrane, consisting of a sensory periplasmic domain for ligand binding, and a cytoplasmic kinase control domain for processing by the chemotaxis biochemical network [131]. The dimeric kinase CheA is closely associated with dimeric MCP pairs, and its output is modulated the presence of bound ligand and the methylation state of the MCP. When ligand binds a pocket in the sensory domain, conformational changes transduce the signal to the cytoplasmic kinase control domain, which downregulates the activity of the kinase CheA in response. MCPs can be methylated and demethylated on a number of cytoplasmic sites, and this methylation state modulates the activity of the kinase CheA [132]. The methylation state changes slowly, so it acts as a memory for the receptor, allowing it to adapt to a stimulus over time [133].

Many thousands of MCPs are known among the bacterial genomes [134], making *E. coli* seem poorly-featured in comparison to its bacterial brethren. For example, the *Shewanella*

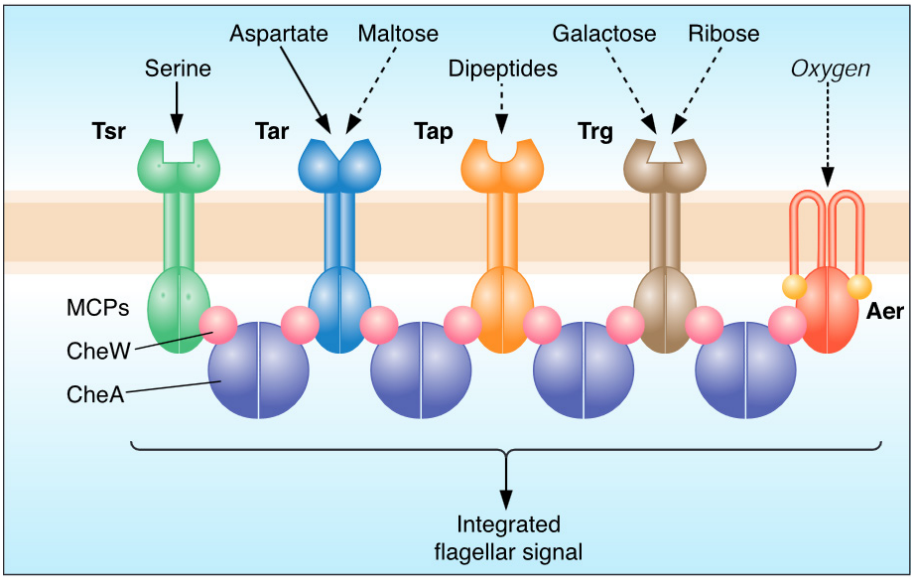

Figure 3.3: The five chemoreceptors in *E. coli*. Solid lines denote direct interactions while dashed lines denote indirect sensing, via periplasmic binding proteins or metabolic effects. Reproduced from Parkinson [121] with permission.

oneidensis genome encodes 27 MCPs [135] and the *Vibrio cholerae* genome encodes 43 MCPs [136]. The great abundance of MCPs in nature presents an opportunity to create hybrid chemoreceptors that mix and match ligand-binding extracellular sensory domains with cytoplasmic processing domains. One such functional hybrid receptor has been developed by fusing the *E. coli* cytoplasmic domain to the sensory domain of NasR from *Klebsiella oxytoca*, resulting in *E. coli* with a new sensitivity to $NaNO_3$ [131]. Rational engineering of chemoreceptor proteins will only improve as protein engineering techniques advance, making the spectrum of potential analytes for chemotaxis-based sensors nearly limitless.

3.2.3 Biochemical processing network

The chemotaxis biochemical network links the chemoreceptors to bacterial flagellar motor through a series of signaling interactions as shown in Figure 3.4. The system architecture is well-conserved across prokaryotes and consists of two parts: a sensory module and an adaptation module.

The sensory module detects chemicals and rapidly adjusts motor rotation to control swimming direction. The chemotaxis biochemical network uses a two-component signaling system to integrate these signals and establish the concentration of a phosphorylated signaling protein, CheY-P, which ultimately sets the probability that the flagellar motor will rotate in a counterclockwise direction, resulting in a straight run, or switch to clockwise, resulting in a tumble [132]. The steep dependence of motor direction on CheY-P concentration results

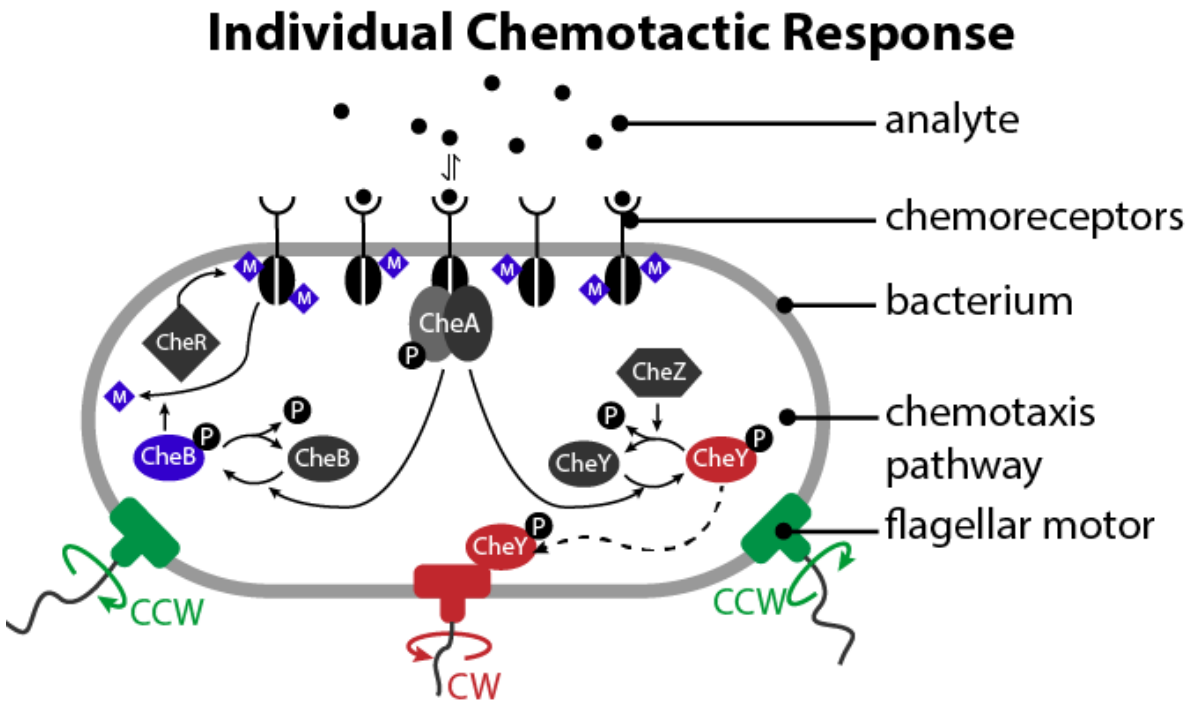

Figure 3.4: The chemotaxis biochemical processing network. Absence of analyte increases CheA kinase activity, which phosphorylates CheY and CheB. The sensory module tunes the level of phosphorylated CheY (CheY-P) to adjust motor bias. CheY-P, when bound to the flagellar motor, reverses its direction. Therefore, a large increase in chemoattractant will quickly suppress CheY-P and encourage counterclockwise motor rotation for an extended run. The adaptation module adjusts the methylation state of the chemoreceptors, which tunes CheA kinase activity. Receptor methylation is mediated by CheB and CheR, and adjusts on a slower timescale than CheY-P signaling.

in a large gain that allows the cell to detect minute changes in receptor occupancy [137]. The result is high sensitivity, with a detection limit reported as low as 3.2 nM for L-aspartate [29]. The response time of the chemotaxis system to a rapid step change in concentration of L-serine averages 250 ms, with the the diffusion of CheY-P from the receptor cluster to a motor being the rate-limiting step [36].

The adaptation module readjusts the response sensitivity on a slower timescale, enabling the system to gradually adapt to more constant conditions. CheB and CheR adjust the methylation state of the chemoreceptors, upregulating or downregulating their activity in response to slow changes in background analyte concentration. This modulation of methylation state effectively implements integral feedback, allowing the system to perfectly adapt to background analyte levels [138].

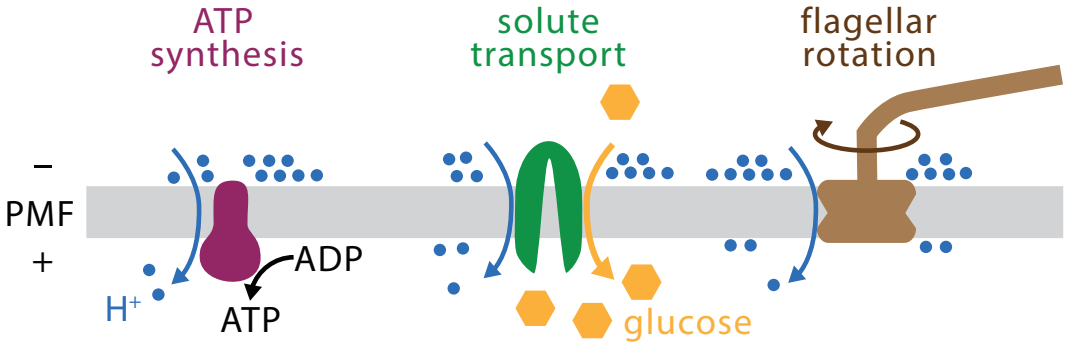

Figure 3.5: The relationship between PMF and bacterial processes. The proton current into the cell supplies the work that synthesizes ATP, transports molecules against gradients, and rotates the flagellar micromotor. Reproduced from Zajdel et al. [94] with permission.

3.2.4 Proton-motive force

The flagellar motor is powered by the proton-motive force (PMF). The PMF is an electrochemical gradient of hydrogen ions (in the form of hydronium) that is maintained across the cell membrane by metabolic processes. This force drives the translocation of protons across the membrane to perform chemical, osmotic, and mechanical work [139]. Metabolic processes maintain this gradient by pumping protons across the cell membrane. The following equation models PMF at room temperature [140]:

$$\Delta p = \Delta\psi + 59\Delta\text{pH} \tag{3.1}$$

In Equation (3.1), Δp is the PMF, $\Delta\psi$ is the cell's membrane potential, ΔpH is the difference in pH across the membrane (pH_o - pH_i), and Δp and ΔpH are in millivolts [mV]. Typical PMF for *E. coli* during aerobic respiration is about $-200\,\text{mV}$, but it decreases in magnitude during fermentation and anaerobic respiration [141]. Since solute transport, ATP generation [140], and flagellar motility [98], [104], [142] are tightly coupled to the PMF (Figure 3.5), the PMF is an indicator of overall cell health.

Despite its widespread importance in understanding the cell, direct measurement of PMF is cumbersome and difficult for small cells. Patch clamping, which has been used to great effect in studying neuronal physiology, is possible on a single bacterium, but quickly becomes intractable for large numbers of cells due to the small amount of membrane area available. Molecular probes such as tetraphenyl phosphonium (TPP+) can only be used to monitor slow changes in PMF [141]. Membrane-binding voltage-sensitive dyes (VSDs) are of limited use in *E. coli* due to the presence of the outer membrane [143], [144]; furthermore, VSDs rely on ratiometric methods because they do not directly report membrane potential [145].

A fluorescent protein reporter for the PMF called PROPS (proteorhodopsin optical proton sensor) has more recently been used in PMF studies [94], [143]. PROPS is a retinal pigment-bound membrane protein whose fluorescence signal strength is correlated with the PMF, likely due to the protonation of a cytoplasmic amino group (Figure 3.6). Stronger

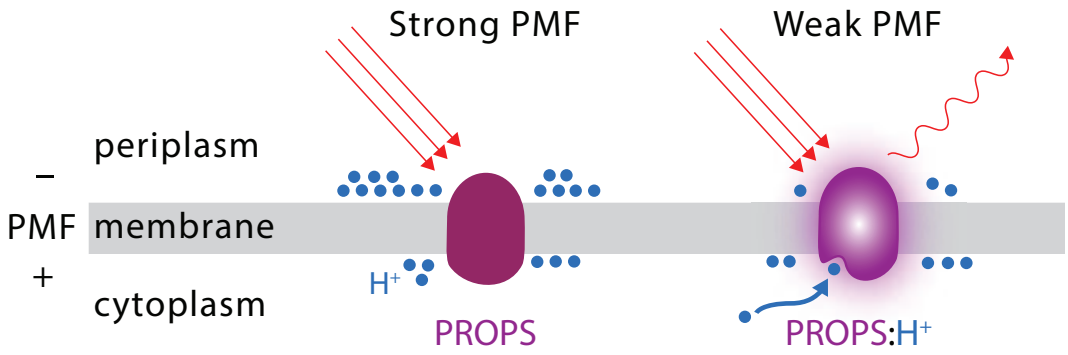

Figure 3.6: Depiction of PROPS sensing model, which is more fluorescent when the presence of a weaker membrane potential or lower internal pH increases the likelihood of protonation of a key amino group. Reduced PMF leads to increased fluorescence. Reproduced from Zajdel et al. [94] with permission.

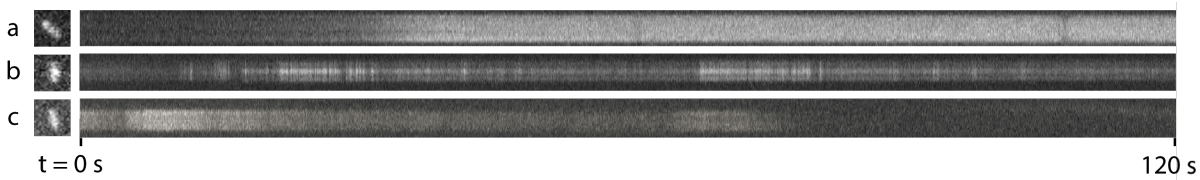

Figure 3.7: The raw PROPS fluorescence signal for a representative selection of cells under the following conditions: (a) after FCCP was added at t=0 sec, (b) during aerobic conditions, and (c) during the addition of nitrogen. Reproduced from Zajdel et al. [94] with permission.

PMF is correlated with reduced PROPS fluorescence. Though PROPS has been used to image rapid dynamics of the PMF [94] (Figure 3.7), its reliance on a high-power fluorescence microscope limits its utility for environmental sensing applications. A label-free and microscope-free assay for PMF would be ideally suited for deployable sensing platforms, and would avoid the problems of existing PMF measurement methods.

3.3 Drawing inference from flagellar observation

With the high speed and sensitivity of bacterial chemotaxis, it is an attractive system to incorporate into a biosensor. However, surprisingly few studies have attempted to draw inferences based on observed *E. coli* behavior. One study observed swimming trajectories [146] while another used fluorescence resonance energy transfer (FRET) to directly report chemoreceptor kinase activity [147], which is an invasive single-cell technique that requires a sensitive microscope. Additionally, high variability between individual bacteria in a population requires responses to be recorded in large numbers, which is cumbersome.

In this study, we utilize an established flagellar stub tethering protocol [148] to moni-

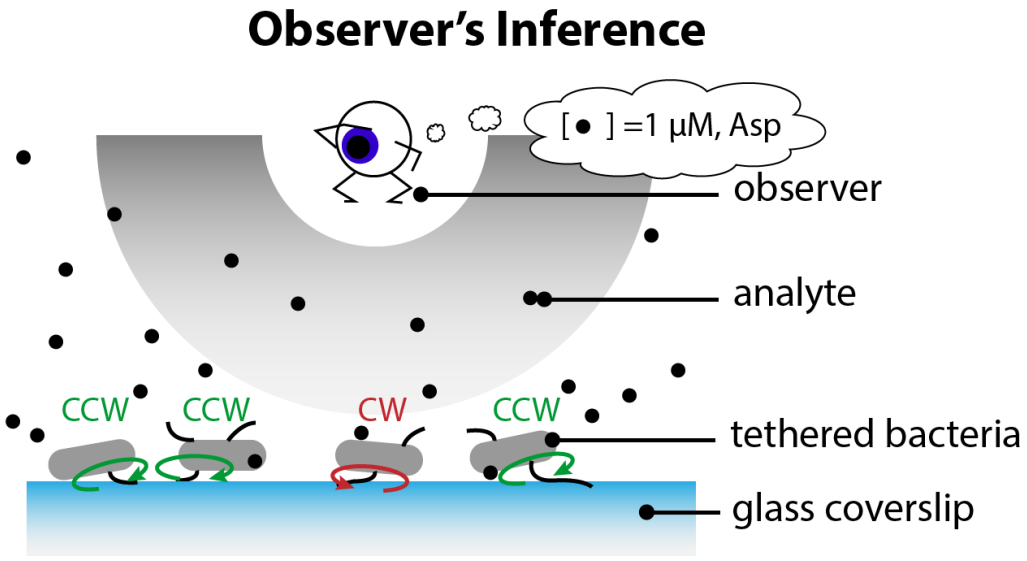

Figure 3.8: Observing the flagellar motor for biosensing. The *E. coli* chemotaxis system rapidly adjusts motor bias in response to analytes and then slowly adapts to background conditions. Observation of motor behavior of a large population of bacteria enables inference of analytes in their environment.

tor the chemotactic motor state of a large number of *E. coli* flagellar motors (Figure 3.8). A microscope is used to observe the motor response of tethered bacteria to dilution series of two amino acid analytes: L-aspartate (Asp), a chemoattractant; and L-leucine (Leu), a chemorepellent. The software we have developed includes an image processing algorithm that extracts the motor's direction as a function of time for the recorded bacteria. The data are then used to train support vector classifiers (SVCs) [149] that can reliably detect different concentrations of Asp as well as differentiate between Asp and Leu. The SVCs are scored with 3-fold cross-validation and inference confidence is characterized. These methods are a step towards the development of chemotaxis-based biosensors, which are attractive due to the adaptability of chemoreceptor systems, demonstrated by ongoing efforts to engineer novel chemoreceptors [131]. Such study also informs attempts to incorporate chemotactic bacteria as the front-end for electrochemical biosensors for microbiorobotics [150].

3.4 Methods

3.4.1 Flagellar tethering and optical microscopy

The SYC12 *E. coli* strain used in this work was provided by Yoshiyuki Sowa. It constitutively expresses sticky flagellin [151] from its genome (genotype: $\Delta fliC::fliC^{st}$) and is derived

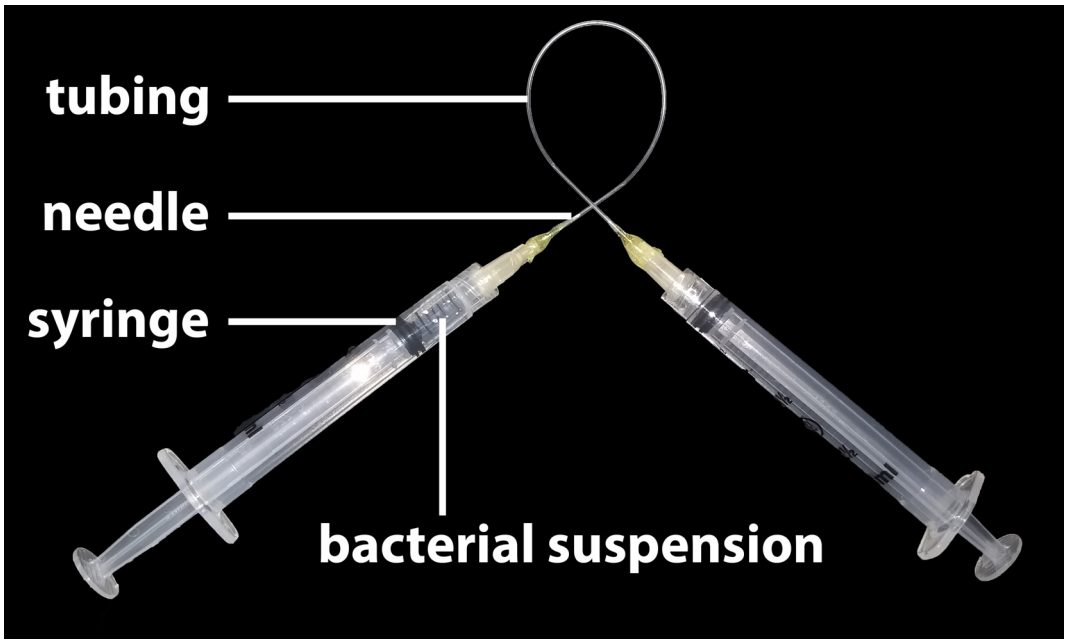

Figure 3.9: Flagella shearing apparatus.

from the wild type chemotactic strain RP437 [121]. Bacteria were prepared by diluting 50 µL of stationary culture into 3 mL T-broth (1 % w/v tryptone, 0.5 % w/v NaCl). Growth commenced at 30 °C with 250 rpm shaking until the culture had an OD_{600} of 0.4-0.6. Then the bacteria were pelleted by centrifugation at 1000 rcf for 1 min and washed twice in motility medium (10 mM KPO_4, 0.1 mM EDTA, 1 mM L-methionine, pH 7.0). The cell suspension was passed 45 times through blunt 26-gauge needles and 10 cm of polyurethane tubing with 0.58 mm inner diameter [108] to shear the flagella to sticky stubs. This shearing apparatus is pictured in Figure 3.9. The cells were then washed once more in motility medium and resuspended to an OD_{600} of 1.0.

The sheared bacterial suspension was injected into a disposable flowcell (Sticky Slide VI 0.2 Luer, Integrated Bio Diagnostics, Martinsried, Germany) attached to a glass coverslip measuring 25 mm by 60 mm (VWR International, Radnor, PA) as shown in Figure 3.10. As supplied, the coverslips had a mildly hydrophobic surface to which the flagellar stubs readily adhered. The bacteria were allowed to tether to the glass for twenty minutes. After this time, 100 µL of motility medium (10 mM KPO_4, 0.1 mM EDTA, 1 mM L-methionine, pH 7.0) was gently flowed through to remove untethered bacteria.

Phase contrast images were taken with an EMCCD camera (iXon+, Andor, Belfast, Northern Ireland) at 40X magnification with a 32 ms sampling period and a square imaging field of 550 by 550 µm (Figure 3.10). Motility medium with dissolved Asp or Leu (concentrations between 100 nM to 1 mM) was flushed through the flowcell and imaging immediately commenced for 120 seconds. To give the bacteria time to return to their baseline adaptation, the channel was flushed with clean motility medium and was left for 10 minutes before the

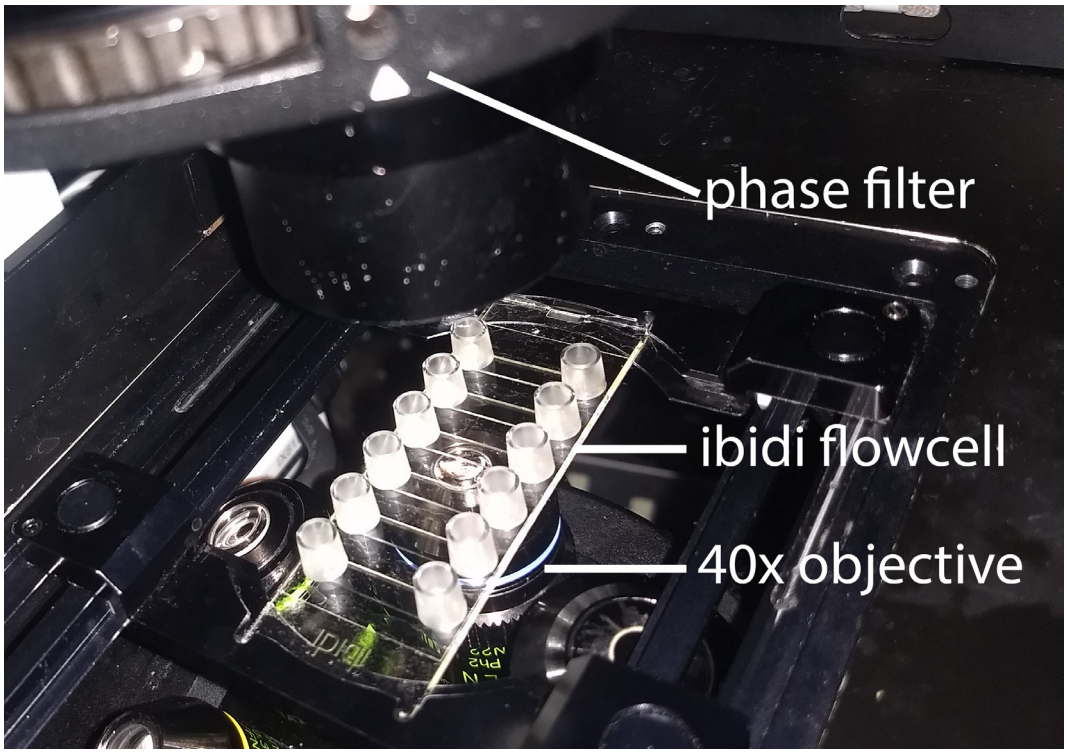

Figure 3.10: Microscopy setup for imaging tethered spinning cells.

introduction of a new condition.

3.4.2 Data processing

Image segmentation and processing

The image segmentation and feature extraction algorithm is pictured in Figure 3.11. Microscopy image streams were first segmented by an ImageJ macro [152]. Each image was denoised by replacing each pixel with an average of its 3 by 3 neighborhood. Then, an unsharp mask was applied to strengthen the borders between the bacteria and their background. Then the image was binarized using an isodata thresholding algorithm [153] and despeckled by a 3 by 3 median filter.

A Python script was used to extract rotation information and compute motor behavior features of interest. The tether point of each spinning cell was detected semi-automatically: a user selected a spinning cell, the binarized image was averaged across 100 frames, and the pixel with the lowest average brightness was deemed the tether point. For each frame, a flood fill originating at the tether point determined the extent of the cell body. The angle between the tether point and the farthest connected point was recorded as the cell's heading. More details about the data processing code can be found in Appendix B.

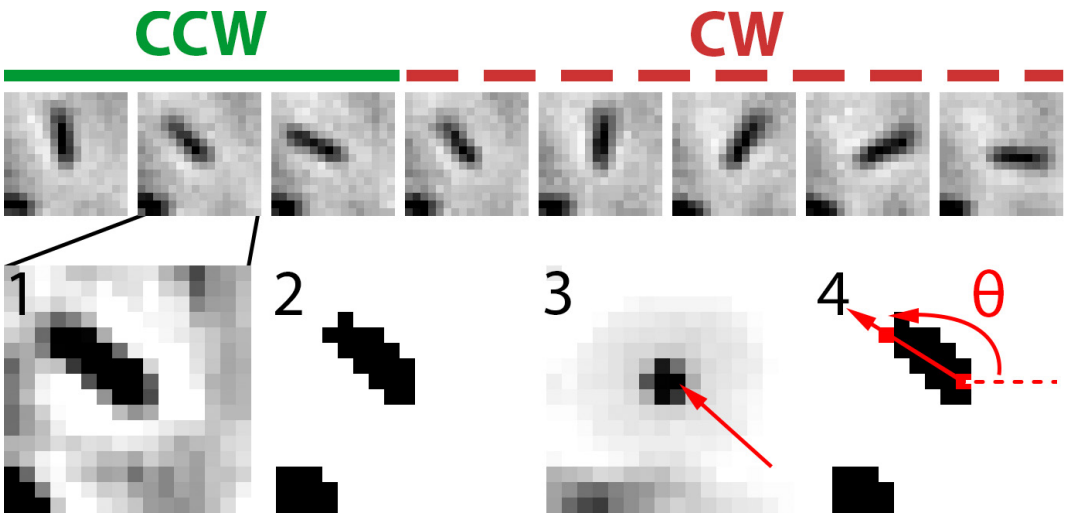

Figure 3.11: Example time lapse microscopy and image processing of a tethered spinner cell (top). The time between frames is 32 ms. A switch in motor direction is evident between the third and fourth frame. In order to extract the cell's orientation over time, the following image processing is done on each frame: (1) smoothing and unsharp mask contrast enhancing, (2) isodata thresholding, (3) averaging to find tether point, (4) flood fill to find farthest point and calculate heading.

Once a large number of heading time series were collected for each experimental condition, features of interest were extracted from the bacteria in aggregate. Each heading trace was smoothed by a 250-ms moving average filter. Then, the rotational velocity was calculated by convolving the one-dimensional derivative kernel $k = [0.5, 0, -0.5]$ across the heading. One example trace is shown in Figure 3.12.

Finally, all the calculated speed traces were passed through a quality control program, which presented the user with a hysteresis-thresholded prediction of cell direction. This allowed the user to reject poor traces, and, if necessary, adjust the thresholds to ensure a good quality match between the calculated trace and the labeled motor directions as shown in Figures 3.13. Thresholding used the following process:

1. Compare velocity ω at a given time point to the upper and lower thresholds (T_{high} and T_{low})
   - if $\omega < T_{low}$, then the direction is CW
   - if $\omega > T_{high}$, then the direction is CCW
   - if $T_{low} < \omega < T_{high}$, then use the direction from the previous time point
2. Proceed to next ω value and repeat until the entire trace is processed

The traces that passed through quality control were used in further analysis.

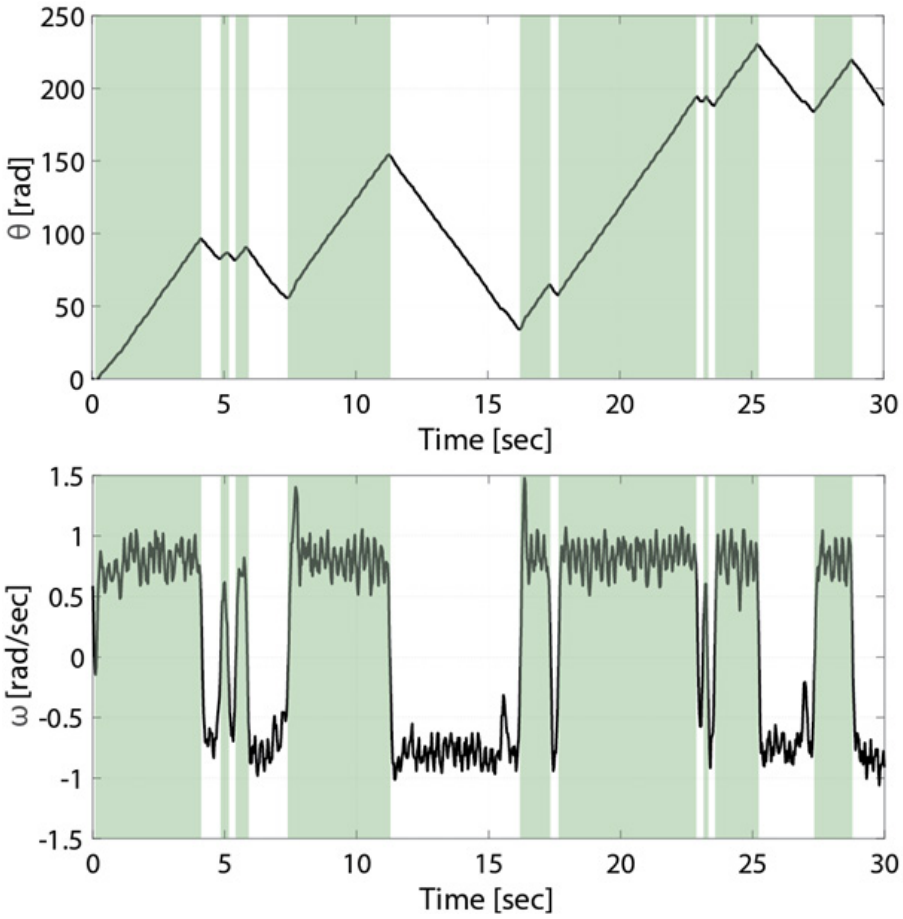

Figure 3.12: Sample rotational position and velocity series for a tethered bacterium in motility medium. Counterclockwise intervals, where rotational velocity is positive, are shaded in green.

Feature extraction

The features that we extracted from these traces were the motor bias B and number of switches N_s. Each of these features were calculated for every bacterium in each condition. The motor bias was computed as the ratio of the total time spent rotating in the counterclockwise (CCW) direction over the length of the analysis window T, as formulated in Equation (3.2).

$$B = \frac{T_{ccw}}{T} \tag{3.2}$$

Hence, motor bias is the average time the motor is rotating in the CCW direction and ranges between 0 and 1. A higher bias typically indicates the presence of a chemoattractant signal, since longer CCW rotation results in longer runs that bias the cell's movement toward the signal [108]. Since B is averaged over a period of time, two cells may have the same bias

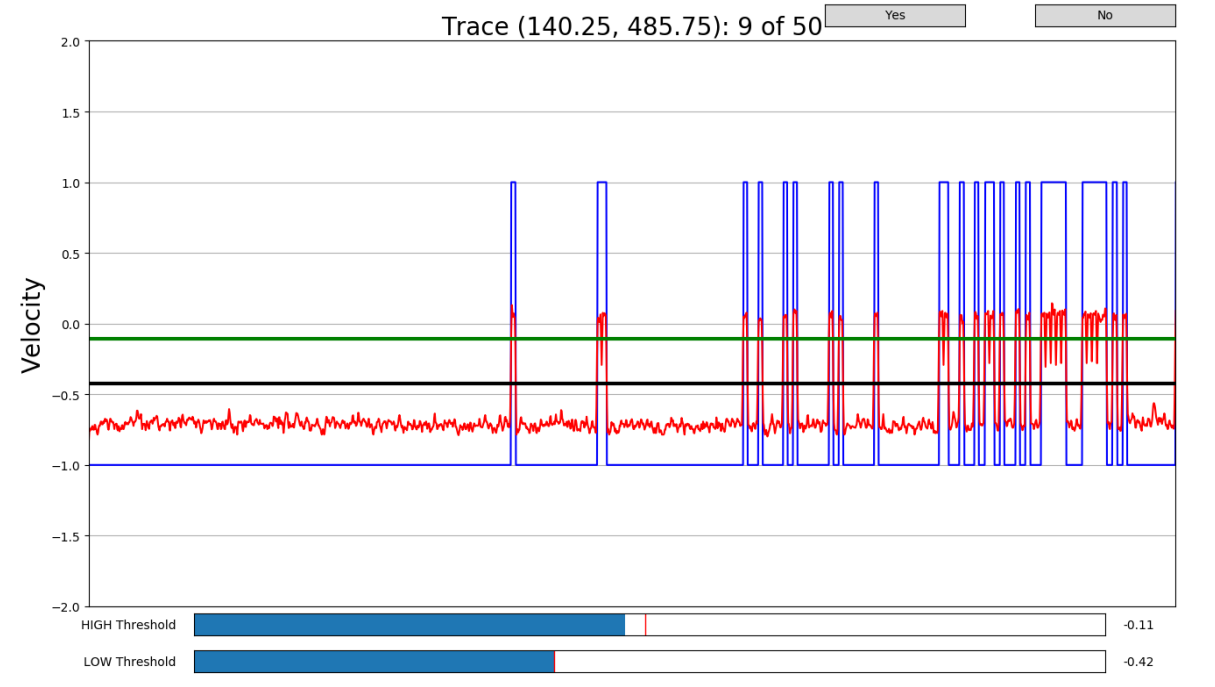

Figure 3.13: Example screen capture of quality control program used to adjust thresholding. The red trace is the velocity time series to be thresholded. The green horizontal line denotes the high threshold while the black horizontal line denotes the low threshold. The user has control over the placement of these thresholds using the bars underneath the x-axis. The blue outline shows the direction assumed by the two thresholds.

despite having different switching profiles. To further disambiguate responses, the number of motor switches N_s was also tracked.

Since the wild type *E. coli* used in this study adapt to chemotactic signals, we were interested in the relationship that these features have with respect to time and concentration. In this pilot study, these relationships were established by fitting a least squares curve to the average data of each condition. $B(T)$ and $N_s(T)$ were fit to Asp and Leu order-of magnitude titrations between 100 nM and 1 mM. Additionally, $B([c])$ and $N_s([c])$ for both Asp and Leu were determined for analysis windows $T = 30, 60,$ and 120 seconds.

3.4.3 Support vector classifiers for per-bacterium labeling

Two classification problems were considered in this study: determining Asp concentration and differentiating between Asp and Leu. For each case, a support vector classifier (SVC) was trained to label individual bacteria as belonging to one group or another. We used the Python scikit-learn library [154] to train and evaluate our SVCs.

Briefly, an SVC makes a prediction by discriminating between objects belonging to one

of a number of categories. The objects are parameterized by a number of features. The classification aims to keep a large margin separating the objects inside each category based on their features. A polynomial kernel attempts to improve separation by drawing a nonlinear boundary between each group. For more information, refer to Ben-Hur et al. [155].

We studied trends in the average population results to identify candidate features to train our SVCs toward these goals. We performed 3-fold cross-validation on each model and calculated the average subset accuracy, which corresponds to the probability that a given bacterium is classified correctly.

3.4.4 Confidence from a consensus among bacteria

Since individual bacteria have high variance in their responses, a practical observer must measure the response of a number of bacteria to have confidence in its inference. A cautious observer watching N bacteria responding to the same conditions could require a consensus of at least $N/2$ of the population to have the same classification to make a statement about the conditions. If the classifier has a per-bacterium success rate of p, then the number of successfully labeled bacteria for a given population N will follow the binomial distribution. We denote the observer's confidence C as the probability of $N/2$ being correctly labeled:

$$C = 1 - F(N/2; p, N) \tag{3.3}$$

In Equation (3.3), $F(x; p, N)$ is the cumulative distribution function for the binomial distribution evaluated at x, which is expanded in Equation (3.4). When $x = N/2$, this term represents the probability that the majority of bacteria are not correctly classified. As the population size N increases, the confidence C also increases, from 0 to 1.

$$F(N/2; p, N) = \sum_{i=0}^{N/2} \binom{N}{i} p^i (1-p)^{(n-i)} \tag{3.4}$$

3.5 Results

3.5.1 Motor features shift with time due to motor adaptation

The experimental conditions tested and the number of good traces from each condition are listed in Table 3.2. These results came from six experimental repeats for each condition taken on three different days. A two-minute experiment yielded a maximum of 50 usable motor traces, but a typical yield was between 20 to 30 traces.

This survey of features revealed a few trends. For illustrative purposes, the histogram in Figure 3.14 plots B and N_s for $T = 30, 60,$ and 120 seconds for all bacteria subjected to 100 nM Asp. From this plot, the large variance in individual motor responses is evident. However, the population mean has a clear trend over time. B drops from 0.83 to 0.62 over this interval as the population adapts. N_s increases with time as expected, growing at a

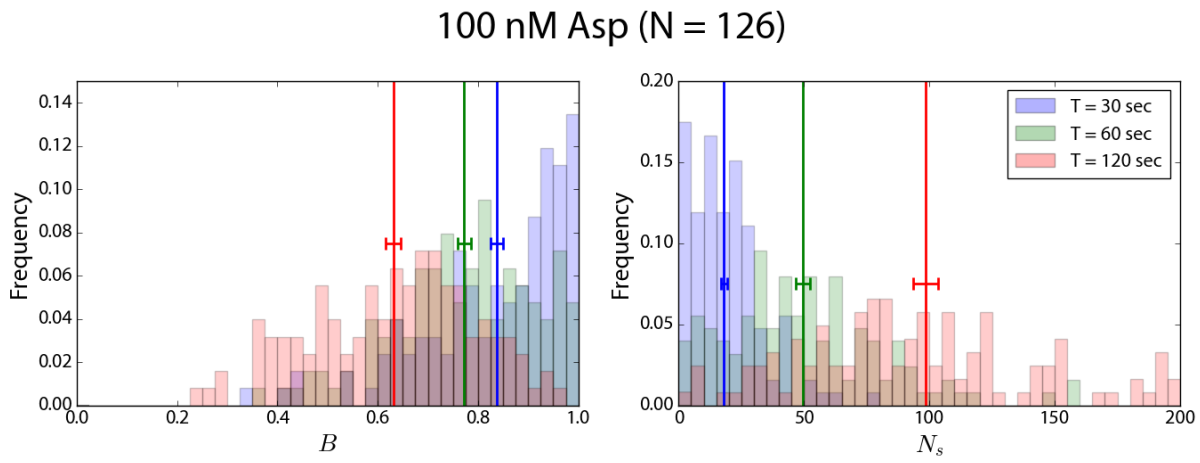

Figure 3.14: Example distribution of bias and number of switches for N=126 wild type chemotactic bacteria perturbed with 100 nM Asp. Features were calculated for $T = 30, 60,$ and 120 second windows, colored blue, green, and red respectively. Each feature mean is denoted by a vertical line and the error bars mark the standard error.

relatively constant rate.

The adaptation time of the chemotaxis system is known to be on the order of 30 to 60 seconds [108]. Wild type cells will adapt rapidly to their conditions, but the kinetics of this adaptation vary with the level of perturbation. Figure 3.15 plots $B(T)$ and $N_s(T)$ across four concentrations tested for both Asp and Leu. A linear trend line successfully fit to B and N_s as a function of T for both chemoeffectors at concentration $[c] = [0$ M, 100 nM, 10μM, and 1 mM].

$$B(T) = B_0 + B_d T \tag{3.5}$$

$$N_s(T) = f_N T \tag{3.6}$$

In Equation (3.5), B_0 is the initial bias immediately after perturbation and B_d is the bias decay rate in sec^{-1}. In Equation (3.6), f_N is the switching rate. These linear relationships fit the population averages well, with the largest root mean square error (RMSE) of 0.0054 for all $B(T)$ fits, and RMSE under 0.535 for all $N_s(T)$ fits (Table 3.3).

The trends suggest a method for determining the concentration of an Asp sample: mon-

Table 3.2: Bacteria count per condition used in spinner analysis.

	Concentration [M]					
	0	10^{-7}	10^{-6}	10^{-5}	10^{-4}	10^{-3}
Asp	146	126	70	207	57	139
Leu	146	132	89	72	41	41

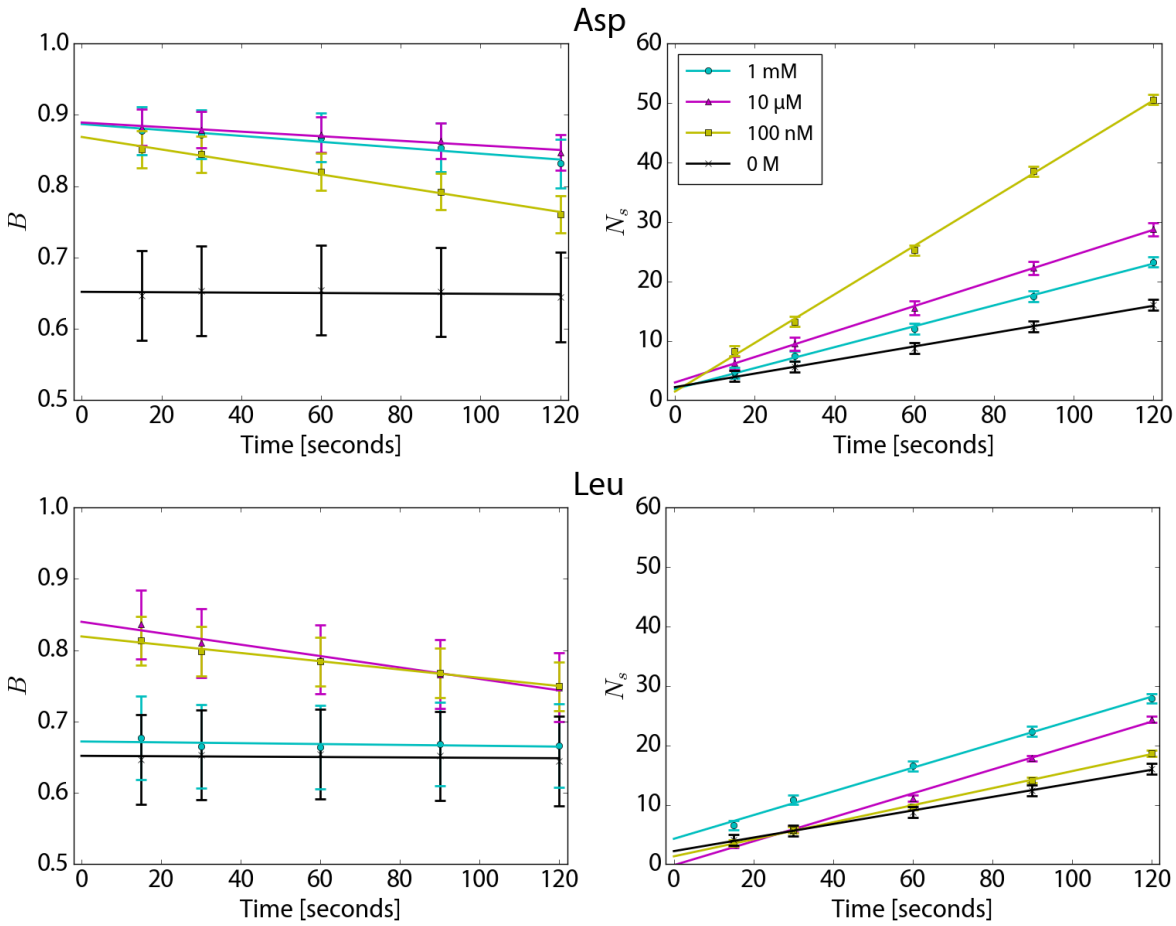

Figure 3.15: $B(T)$ and $N_s(T)$ over time for Asp and Leu at 1 mM, 10 µM, 100 nM, and 0 M with linear fits.

itor $B(T)$ for an unknown sample and determine the bias decay rate, which is the slope of the line of fit. Since this decay is similar for Asp concentrations at or above 1 µM, the sample could be serially diluted until the response for 100 nM is replicated to determine the concentration of the initial sample.

3.5.2 Motor features shift with concentration due to sensing characteristics

We also fit parameters to the trends describing B and N_s as a function of concentration as shown in Fig 3.16. The trend established in our tests was different between Asp and Leu. Motor bias versus Asp concentration $B_{Asp}([c])$ followed a four-parameter sigmoidal

Table 3.3: RMSE for fits for the evolution of B and N_s over time.

Chemoeffector	Feature	RMSE of fit for each $[c]$ 0 M	10^{-7} M	10^{-5} M	10^{-3} M
Asp	$B(T)$	.0036	.0023	.0024	.0045
	$N_s(T)$	.147	.535	.140	.265
Leu	$B(T)$	.0036	.0020	.0054	.0044
	$N_s(T)$	.147	.167	.459	.468

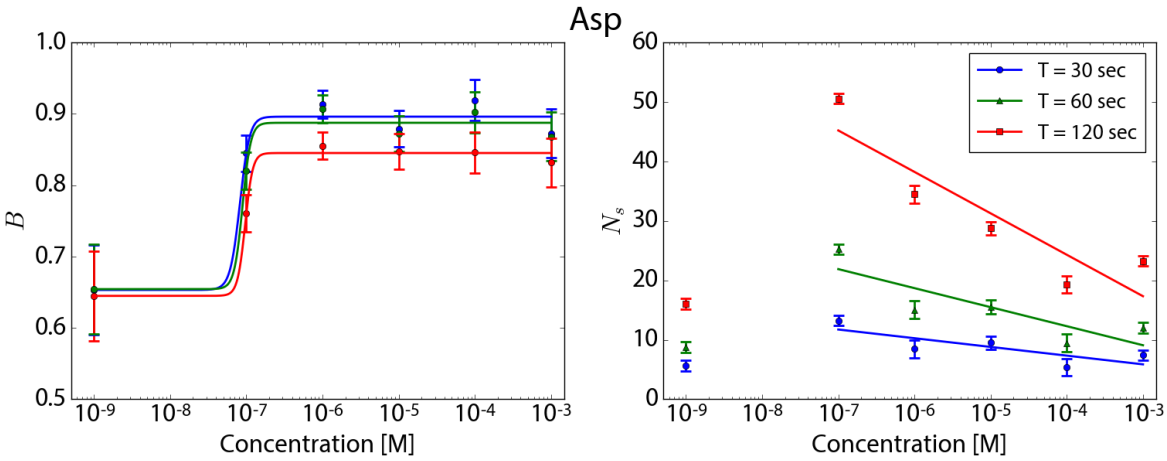

Figure 3.16: $B([c])$ and $N_s([c])$ over time for Asp at $T = 30, 60,$ and 120 seconds with fits.

relationship described by Equation (3.7):

$$B_{Asp}([c]) = B_{max} + \frac{B_0 - B_{max}}{\left[1 + \left(\frac{\log_{10}[c]}{B_{1/2}}\right)^n\right]} \tag{3.7}$$

The $T = 30$ second response saturated to 0.90 at concentrations higher than 1 µM. This sigmoidal response persisted while the responses adapted over the 120 second window, as seen in the green and red fit lines, relaxing to $B_{max} = 0.85$ at the end of the interval. This response was expected because Asp is a known chemoattractant. The cell has a low threshold for detecting Asp (3.2 nM) so $B_{Asp}([c])$ saturates at higher concentrations.

On the other hand, the motor bias for Leu $B_{Leu}([c])$ (Figure 3.17) followed a roughly quadratic relationship described by Equation (3.8), although with low significance:

$$B_{Leu}([c]) = A_\theta \log_{10}^2[c] + B_\theta \log_{10}[c] + C_\theta \tag{3.8}$$

The parameters A_θ, B_θ, and C_θ have a physical interpretation when one considers that the bias is maximized to $B_{max} = C_\theta - \frac{B_\theta^2}{4A_\theta}$ when $\log_{10}[c]_{max} = \frac{-B_\theta}{2A_\theta}$. Since Leu is a known

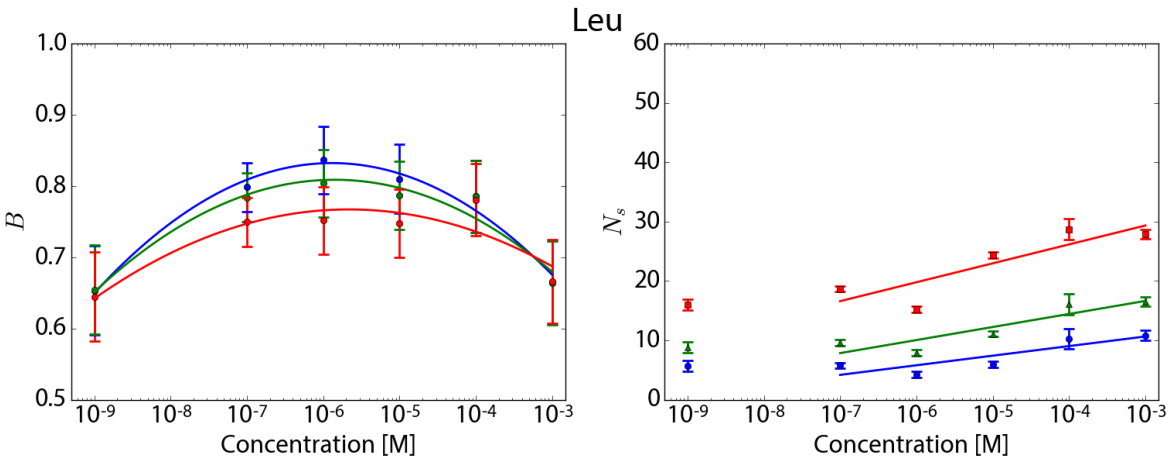

Figure 3.17: $B([c])$ and $N_s([c])$ over time for Leu at $T = 30, 60,$ and 120 seconds with fits.

chemorepellent, B_{Leu} was expected to decrease monotonically with increasing concentration. Interestingly, $B_{Leu}([c])$ rose to a maximum of 0.83 at $[c]_{max}$ 1 µM. This response adapted quickly, dropping back to within 15% of the baseline in 120 seconds. It has been reported that although Leu is a chemorepellent, it acts as an attractant at low concentrations [29], which complicates analysis. As a result, concentration prediction was not attempted for Leu in this initial study.

An apparent difference between Asp and Leu responses emerges when N_s is plotted against $\log_{10}[c]$ (Figure 3.18). A linear trend results for both Asp and Leu (RMSE is given in Table 3.4), with N_{sAsp} decreasing with increasing $\log_{10}[c]$ and N_{sLeu} increasing with increasing $\log_{10}[c]$. Therefore, two samples could be differentiated into Asp or Leu by determining $N_s([c])$ for each and establishing if it is increasing or decreasing.

Table 3.4: RMSE for fits for B and N_s as a function of concentration $[c]$.

		RMSE of fit for each T		
Chemoeffector	Feature	30 sec	60 sec	120 sec
Asp	$B([c])$	.0167	.0151	.0219
	$N_s([c])$	1.455	2.732	4.459
Leu	$B([c])$	.0109	.0151	.0219
	$N_s([c])$	1.207	1.404	2.451

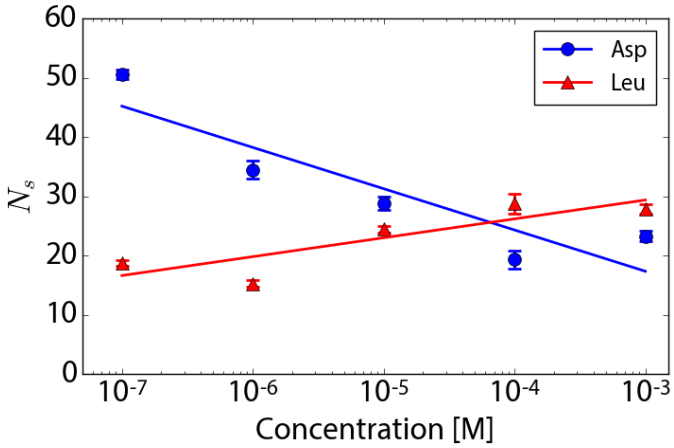

Figure 3.18: $N_s([c])$ over time for Leu and Asp at $T = 30, 60,$ and 120 seconds with fits.

3.5.3 SVC training and validation

Determining Asp concentration

E. coli is very sensitive to Asp concentration so its motor bias remains saturated near 1 µM, even after 120 seconds. Therefore, motor bias is not a good feature to use to differentiate Asp concentrations between 1 µM and 1 mM. However, the $B(T)$ response is distinct between 0 M, 100 nM, and 1 µM. We randomly selected 120 cells labeled as either '0 M', '100 nM', or '1 µM' to populate the label vector $\mathbf{y}_{120\times 1}$. Given the distinct linear trends in $B(T)$, we populated our feature matrix $\mathbf{X}_{120\times 4}$ with rows consisting of the $B(T)$ of the corresponding cell in the label vector at $T = 30, 60, 90, 120$ seconds:

$$\mathbf{X}_{120\times 4} = \begin{bmatrix} B(30\text{s}) & B(60\text{s}) & B(90\text{s}) & B(120\text{s}) \\ \vdots & \vdots & \vdots & \vdots \end{bmatrix}$$

$$\mathbf{y}_{120\times 1} = \begin{bmatrix} \{0, 100\text{n}, 1\mu\} \\ \vdots \end{bmatrix}$$

The data was split into three groups of 40 for 3-fold cross-validation, and the SVC was trained with a polynomial kernel of degree 3. The computed subset accuracy (average fraction of correct labels) was 69%, reflecting the high variance in individual cell response. The confusion matrix is presented in Figure 3.19, demonstrating the best accuracy (77%) was for 1 µM Asp, the highest concentration used in the classification. Careful optimization of data acquisition could increase the accuracy further, but inherent variability in gene expression will always produce a range of sensitivities in a given population.

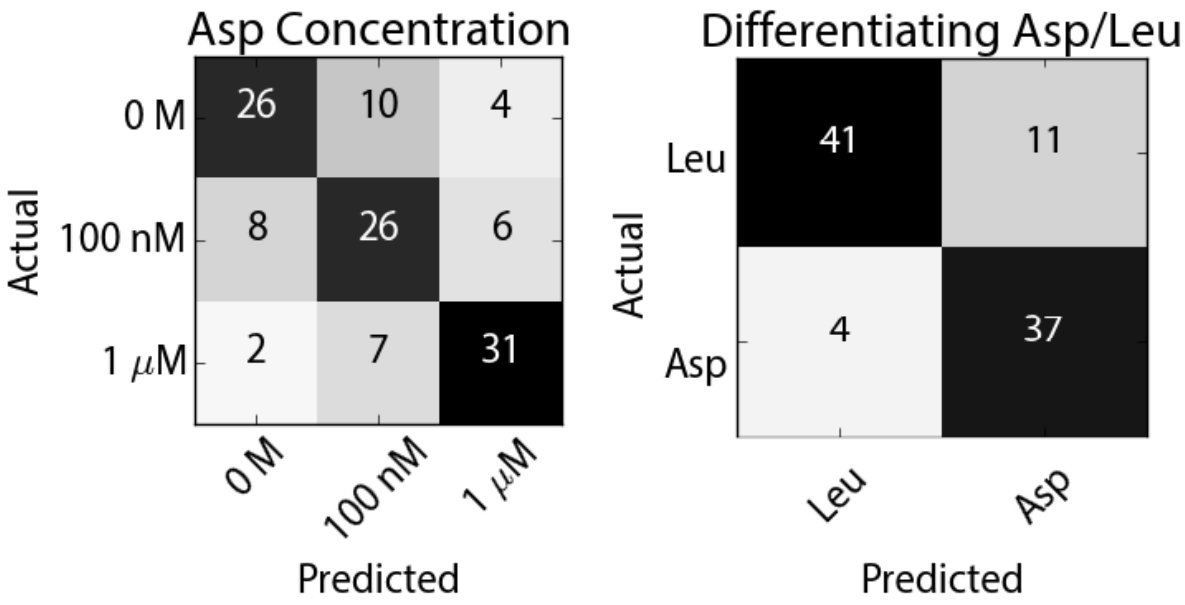

Figure 3.19: The confusion matrices resulting from cross-validation of the classifiers.

Differentiating between Asp and Leu

E. coli responds differently to Asp and Leu since the former is a chemoattractant and the latter is a chemorepellent. Leu generally induces more motor switching in *E. coli* as its concentration is increased, while Asp suppresses motor switching as its concentration is increased. We randomly selected 90 cells labeled as either 'Asp' or 'Leu' to populate the label vector $\mathbf{y}_{90\times 1}$. Given the distinct trends in $N_s(c)$, we populated our feature matrix $\mathbf{X}_{90\times 3}$ with rows consisting of $N_s(c)$ of the corresponding cell in the label vector at $c = 10^{-7}, 10^{-5}, 10^{-3}$ M:

$$\mathbf{X}_{90\times 3} = \begin{bmatrix} N_s(10^{-7}\text{M}) & N_s(10^{-5}\text{M}) & N_s(10^{-3}\text{M}) \\ \vdots & \vdots & \vdots \end{bmatrix}$$

$$\mathbf{y}_{90\times 1} = \begin{bmatrix} \{\text{Asp}, \text{Leu}\} \\ \vdots \end{bmatrix}$$

The data was broken into three groups of 30 for 3-fold cross-validation, and the SVC was trained with a polynomial kernel with degree 3. The subset accuracy was 83%. The confusion matrix is presented in Figure 3.19 and reflects this high subset accuracy.

3.5.4 Number of cells required for high prediction confidence

Following Equation (3.3) and the subset accuracies achieved by the SVCs, the majority-label confidence was calculated as a function of number of bacteria N. A confidence of

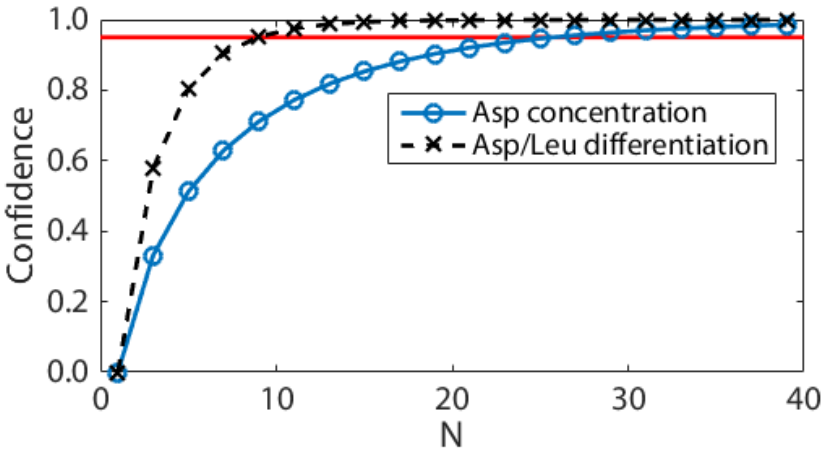

Figure 3.20: Confidence versus the number of cells classified, assuming that the bacteria reach a majority consensus. A confidence of 0.95 (marked with horizontal red line) occurs at $N = 27$ when determining Asp concentration and $N = 9$ when differentiating between Asp and Leu.

95% is achieved at $N = 27$ for determining Asp concentration and $N = 9$ for Asp/Leu differentiation, as seen in Figure 3.20. These population sizes are easily achieved in one experiment, and only 120 seconds of data need to be recorded.

3.6 Discussion

3.6.1 Adaptability of this method to other analytes

These preliminary results provide a framework for using observed flagellar motor responses to infer environmental changes that can be readily expanded by biological engineering. Synthetic biologists have designed chimeric chemoreceptors that confer new sensing ability to *E. coli* [131]. Receptors can be knocked out, resulting in orthogonal responses from different cell populations, and could make it easier to differentiate between chemicals. Protein engineering techniques allow for fine tuning of the sensitivity of chemotaxis to different concentration ranges [156], expanding the range of detectable concentrations beyond those in this study. However, incorporating more labels would likely require more data to properly train the SVCs and require a higher N, more features, or multiple strains of *E. coli* to properly assess conditions.

3.6.2 Tracking the proton-motive force

The speed of the motor could also be tracked, allowing for real time monitoring of the proton-motive force (PMF), which responds to a number of other environmental signals and

powers the motor's rotation [94]. This signal can be used to follow the health of a bacterium, since a lower PMF often indicates respiratory stress. The load of the cell body on the flagellar motor can be estimated based on the cell's length, so the PMF can be extracted quickly for many individual bacteria.

3.7 Conclusion

In this chapter, we proposed using observations of the bacterial flagellar motor to identify and quantify bioanalytes. The chemotaxis system couples chemoreceptor measurements to the motor response, which we characterized for a large number of cells using our image processing suite. We then demonstrated inferring aspartate concentration and differentiating between leucine and aspartate by training SVCs to classify motor responses. This analysis suggests that tens of cells are enough to make strong conclusions about analytes for simple differentiation, and upwards of a few hundred cells would likely be necessary for more complex analysis. Since the chemotaxis system is readily adaptable, there is potential for bottom-up design of new biosensors that work on this principle.

Chapter 4

Towards electronic flagellar observation

The content of this chapter was adapted with permission from the following paper and unpublished manuscript:

- "Towards a biohybrid sensing platform built on impedance-based bacterial flagellar motor tachometry" by T.J. Zajdel, A.N. Walczak, D. Sengupta, V. Tieu, B. Rad, and M.M. Maharbiz [150]
- "Electronic observation of flagellar rotation for biosensing" by T.J. Zajdel, M. Lester, A. Nam, T. Pilizota, B. Rad, and M.M. Maharbiz

4.1 Prelude: A brief history of flagellar motor observation

Due to the importance of the bacterial flagellar motor (BFM) in motility and chemotaxis, myriad genetic and physical tools have been developed to observe its operation. The process began in the early 1670s, when Antoni Leeuwenhoek discovered what he called "animalcules" by observing lake water with his home-built microscope [157]. Since then, the motility of microscopic organisms has fascinated biologists and physicists alike [97], [158]. Nearly two hundred years later, Theodor Engelmann showed that *Chromatium*, bacterial species isolated from the Rhine river, would swim towards oxygen and certain wavelengths of light [159], the first recorded observations of aerotaxis and phototaxis. At nearly the same time, Wilhelm Pfeffer introduced a microcapillary assay that he used to quantitatively measure the chemotaxis response to varying concentrations of chemoeffectors [160]. Then, in the 1960s, Julius Adler began to apply the tools of *Escherichia coli* genetics to bacterial motility and started to unravel the components of the chemotaxis biochemical signaling system [161], [162]. Then in 1972, experiments by Howard Berg, Rober Macnab, and Doug Koshland demonstrated the canonical run-tumble behavior in *E. coli* using time-lapse microscopy and automated

tracking [32], [163]. At this point, Berg and Anderson proposed that *E. coli* swims by rotating its flagellar filaments, but they lacked definitive proof [164].

Because the diameter of the flagellar filament (20 nm) is far below the optical diffraction limit [100], flagellar rotation in *E. coli* had not been imaged in live cells. Then in 1974, Silvermann and Simon tethered flagella from different cells to each other with anti-flagellin (FliC) antibodies [165], observing the cell bodies move in a rotational precession that confirmed the rotary nature of the bacterial flagellar motor. About a decade later, a spontaneously sticky version of flagellin, FliCst, emerged [151]. FliCst has since been used to directly tether bacteria to hydrophobic substrates by a sheared flagellar stub [166] or to attach a spherical latex bead to the stub [167], [168], without the expense of antibodies. To remove the dependency of these bead assays on flagellar stub length, a biotinylated flagellar hook was developed to enable binding to streptavidin-coated beads 1 micron or less in diameter [169], utilizing the high-affinity streptavidin-biotin bond. The radius of rotation of each of these bead assays is small (<0.5 µm) and the rotational velocities are fast (up to 100 Hz), so high power microscope objectives (>60x) with high frame rates (>100 fps) are required to resolve flagellar rotation.

Although optical observation has been used extensively to study signaling and biophysics of the BFM, such methods are not easily incorporated onto mobile sensing platforms. Light sources consume far more energy than electrochemical measurements, and high-power objectives are not easily miniaturized. In this chapter, we propose a new method for BFM observation that uses electrochemical impedance measurements to report flagellar motor behavior to enable integration with electronic biosensing platforms.

4.2 Electronic flagellar observation: Opportunities and challenges

There is an opportunity to use bacteria as the front-end for a biohybrid sensor with a fast response time, but this requires real-time observation of chemotaxis. A number of microfluidic devices monitor bulk migration of *E. coli* for quantitative and qualitative assays [170]–[173]. These methods all share a common drawback in that they wait for observable population-scale movement, which often takes tens of minutes to establish. Other studies use more promising individual BFM or cell-signaling measurements to make inferences [95], [146], [147], [174], but these methods have been exclusively limited to optical microscopy, since established methods for observing an individual BFM all require the use of a microscope [106], [148], [175]. A method for electronic observation of the BFM is not presently available, but would use far less power and would be more readily integrated in a mobile sensing system than optical methods.

Electrochemical impedance measurement methods have developed to the point of detecting single dielectric beads or cells in microfluidic channels by the Coulter counter principle [55], [176]–[182] and could enable electronic observation of the BFM. These systems use

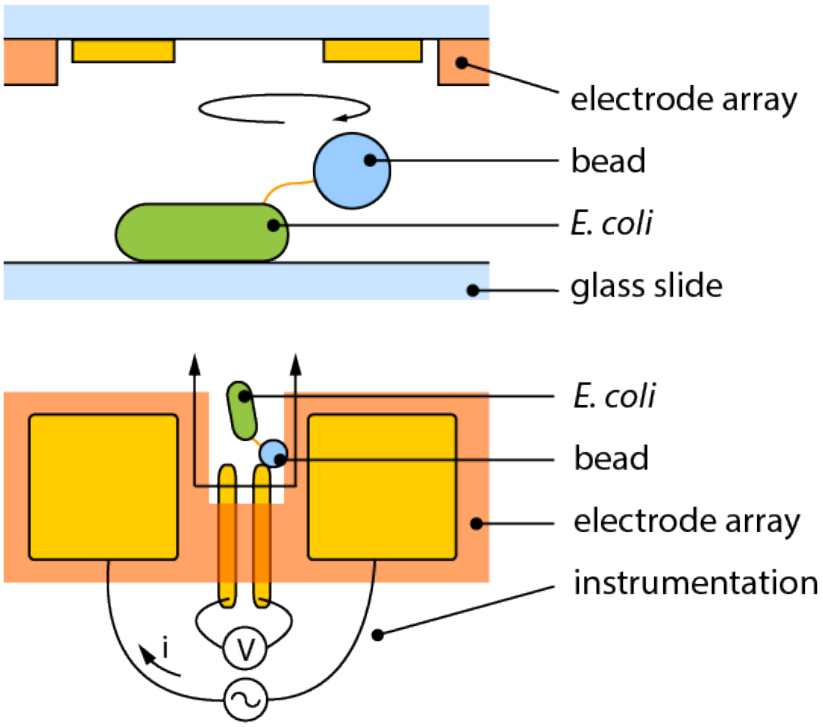

Figure 4.1: Overview of impedance-based electronic observation of bacterial flagellar motor rotation. A flagellum-driven bead rotates in close proximity to a pair of microelectrodes that continuously monitors the solution impedance. As the bead perturbs the electric field, the electrodes continuously monitor the impedance.

impedance spectroscopy to detect changes in electrical impedance with biological or diagnostic relevance. These methods often use relatively large electrodes, on the order of 400 μm^2 or larger, in order to bypass the screening effect of the double layer impedance [50], [183] and are not well suited to monitor BFM rotation that occurs over a 1-3 µm diameter. Other methods use flow focusing [184] or very small microfluidic channels [55], [176], [179], [182] to increase the SNR of the measurement, but these methods require samples to be delivered across the electrodes by continuous flow. A more persistent two-dimensional imaging technique has been demonstrated to monitor epithelial cell migration over scales of 30-500 µm [51], [185], but localized impedance monitoring with a spatial resolution relevant to BFM rotation remains a challenge [150]. Electrochemical sensing systems have been miniaturized to the extent that persistent environmental deployment will soon be possible [42], and sensors with rapid response times that require minimal power consumption are desired.

In this chapter, we present an attempt to observe bacterial flagellar motor (BFM) rotation in *E. coli* electronically (Figure 4.1). Our method labels the flagellar filament with a polystyrene bead and then uses micromaniuplators to deliver the motor-driven rotating bead

in proximity to a microelectrode array that monitors for changes in solution impedance. The three main achievements we present are:

1. Detecting localized impedance changes within a microscale recording site
2. Labeling BFM rotation with dielectric beads
3. Delivering a labeled BFM to the recording site with micrometer precision

In the end, while each individual component was successful in isolation, when integrated together, they were not sufficient to observe BFM rotation electronically due to what were ultimately weak perturbations in impedance caused by the bead's rotation. The remainder of this chapter describes the methods we developed, addresses the remaining outstanding problems, and outlines a few potential solutions for moving forward.

4.3 Detecting localized impedance changes

To enable measurement of localized impedance changes, a four-point microelectrode array was fabricated onto a transparent silica substrate using standard lithographic techniques (Figure 4.1). This array was designed to detect changes in impedance within a microscale region, since the flagellar motor does not have the torque output to rotate an arbitrarily large bead. The electrode arrays we built consisted of a pair of 4 µm by 4 µm potential sense electrodes and a pair of 100 µm by 100 µm current injection electrodes. In this section, we discuss the fabrication, modeling, electrical characterization, and testing of these arrays.

4.3.1 Microelectrode array fabrication and assembly

The microelectrode array fabrication process is outlined in Figure 4.2. The arrays were fabricated on 500 µm thick 6″ diameter fused silica wafer substrates (University Wafer, South Boston, MA). First, the electrodes were patterned by a standard lift-off process. Briefly, the pattern was exposed by a stepper lithography tool (ASML 5500/300) onto lift-off resist (LOR-3A, MicroChem, Westborough, MA) and a standard DUV photoresist (UV210-0.6, Dow chemical, Midland, MI), and developed. Then, a metalization layer of 5 nm Ti and 145 nm Au was deposited by electron beam physical vapor deposition (EBPVD) (Solution evaporator, CHA Industries, Fremont, CA). Finally, the substrate was immersed in Remover 1165 for lift off (Dow Chemical, Midland, MI). Next, a 2.8 µm layer of polyimide precursor (PI 2610, MicroChem, Westborough, MA) was spun on to insulate the traces. The polyimide was then cured for 30 minutes at 450 °C under nitrogen in a vacuum oven (Yield Engineering Systems, Livermore, CA). Afterwards, a 75 nm Al hard mask was deposited and patterned using the EPCVD and liftoff process described above. The polyimide was etched by O_2 plasma (Plasma-Therm PK-12 RIE, 100 mTorr, 80 sccm O_2, 150 W RF power, 25 min) to expose the wire bond pads and recording sites. Afterwards, the Al hard mask was removed by a wet etch in Aluminum Etchant Type A at room temperature (80% H_3PO_4 + 5% HNO_3

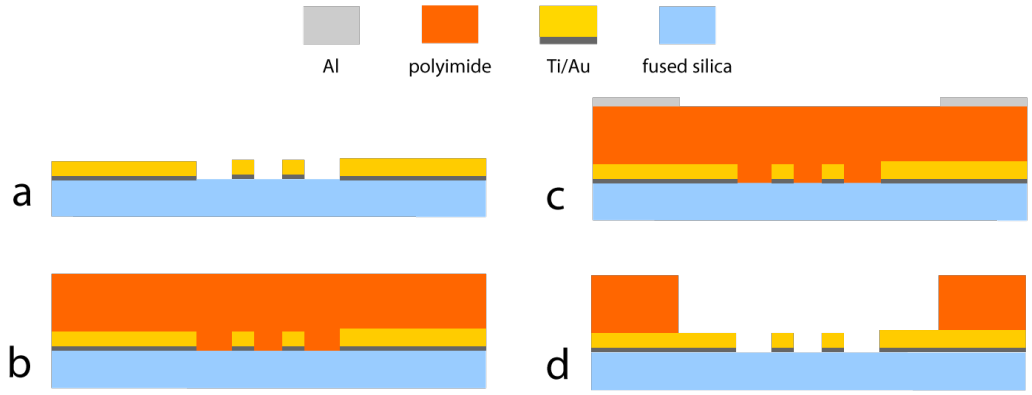

Figure 4.2: Microelectrode array fabrication process. (i) Start with a fused silica wafer and define metalization of 5 nm Ti and 15 nm Au via photolithography and liftoff. (ii) Spin coat 2.8 µm polyimide precursor and cure at 450 °C. (iii) Pattern 75 nm Al hard mask on polyimide via lithography and liftoff. (iv) Dry etch polyimide with O_2 plasma to expose bond pads and recording sites, then remove Al by a wet etch.

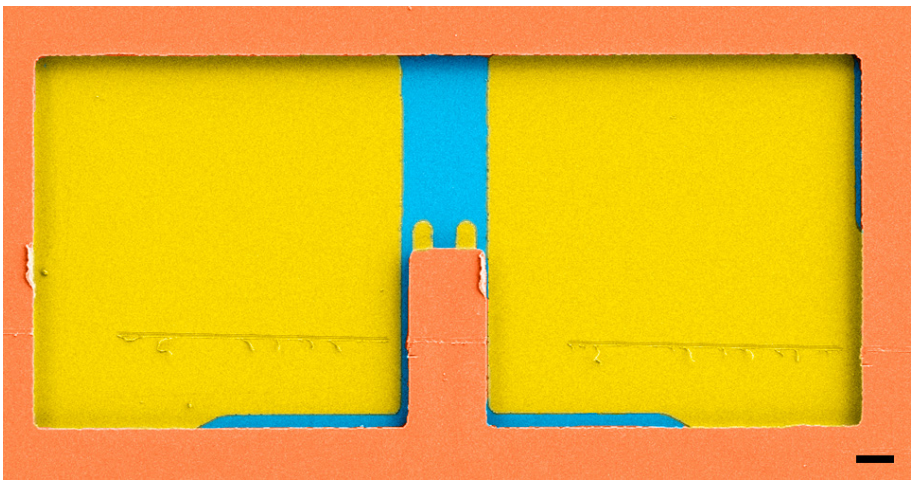

Figure 4.3: False colored SEM of four-point measurement array. Blue regions denote the fused silica substrate, orange regions denote polyimde, and gold regions denote the Au electrodes. Scale bar is 10 µm.

+ 5% CH_3COOH + 10% H_2O). Finally, the devices were singulated into individual dies with a dicing saw (DAD3240, Disco Corp., Santa Clara, CA). An SEM of the completed array (after 10 nm Au sputtering to prevent charging) is shown in Figure 4.3. More fabrication process details are presented in Appendix A.

Each die was then assembled onto an integrated optical and impedance measurement platform shown in Figure 4.4. A single die was affixed to an interface board with Crystal-

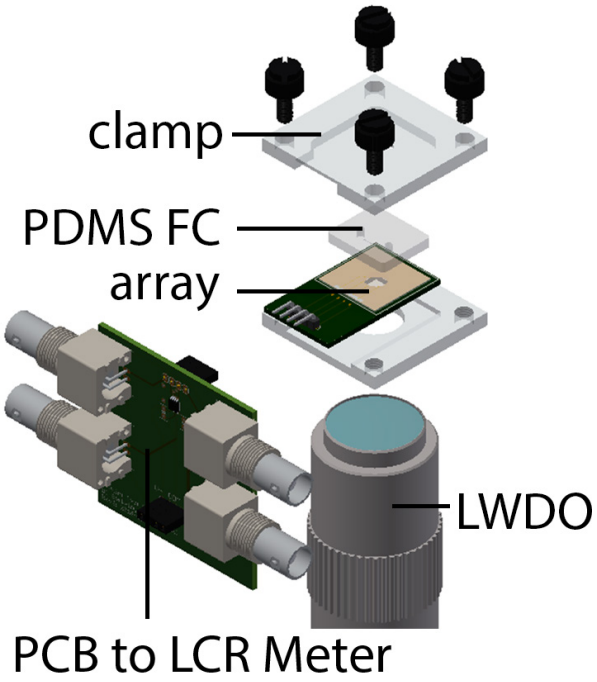

Figure 4.4: Exploded assembly of the instrumentation used for synchronized microscopy and impedance measurements for validation. PDMS FC: polydimethylsiloxane flowcell; LWDO: long working distance 50X objective.

bond (SPI Supplies, Camden, NJ), then aluminum wedge wire-bonded to complete electrical connections. A polydimethylsiloxane (PDMS) gasket molded from a standard SU-8 soft lithography process defined a 15 µm microfluidic channel and was clamped into place for imaging.

4.3.2 Four-point impedance measurements

Equivalent circuit model

The equivalent circuit model for four-point impedance measurements is shown in Figure 4.5 [51], [150]. This system was designed to detect the movement of a polystyrene bead near the recording site. The resistance R_{sol} should increase slightly as the bead displaces the conductive solution between the pick-up electrodes, so R_{sol} is the primary parameter of interest. R_{spread} is the spreading resistance between the electrodes, with an analytic solution available in the literature [186], [187]. Solution capacitances are assumed to be very low and are ignored in our model for simplicity.

Following the technique presented by Linderholm et al. [51], an instrumentation amplifier (AD8221, Analog Devices) was used with unity gain to provide a large input impedance (1 GΩ) to the pick-up electrodes and feed the difference between them to a Keysight E4980AL

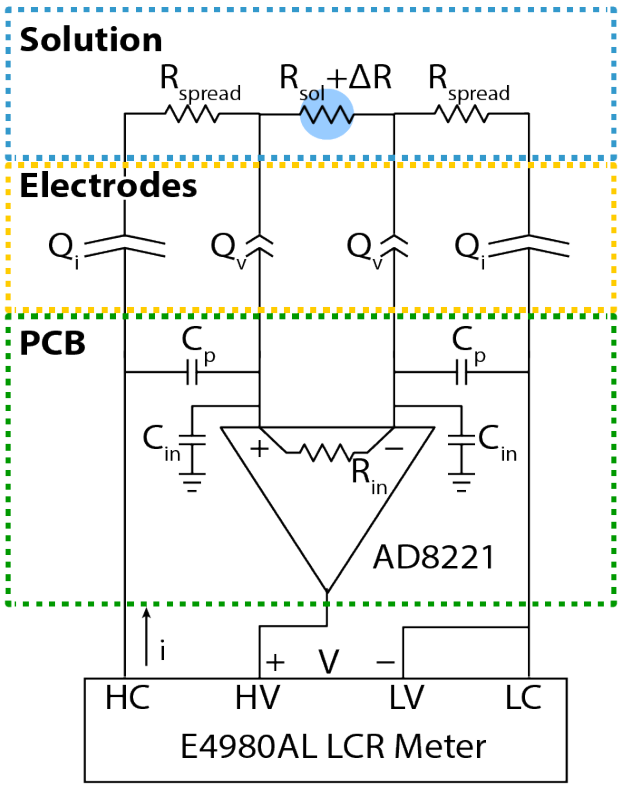

Figure 4.5: Equivalent circuit model for four-point impedance measurements. An instrumentation PCB provides a high-impedance interface from the electrode array to a Keysight E4980AL impedance analyzer. A dielectric bead passing between the pick-up electrodes causes an incremental change in measured solution resistance.

impedance analyzer. The custom printed circuit board implementing this interface is shown in Figure 4.6. The stray capacitances between circuit traces C_p (roughly 10 pF) and the input capacitance of the amplifier C_{in} (10 pF) provided an upper bound to the frequency used to measure R_{sol}, since at high frequencies these parasitics would short the measurement (about 100 kHz). The electrical double layer that would form at each electrode/solution interface, denoted by constant phase element Q_i or Q_v, was approximated as a capacitance following Equation (1.4). Assuming a solution ionic strength of 20 mM (the ionic strength of motility medium), the larger electrodes would have a C_{dl} of 44 pF and the smaller electrodes would have a much smaller C_{dl} of 70 fF. At low frequencies, the interfacial impedances would be prohibitively high, preventing the system from measuring R_{sol}. For example, the interface impedance for the larger electrodes is over 3 MΩ at 1 kHz, while R_{sol} is expected to be only 20 kΩ. A reduction in this interfacial impedance would allow for a wider range of R_{sol} measurement frequencies.

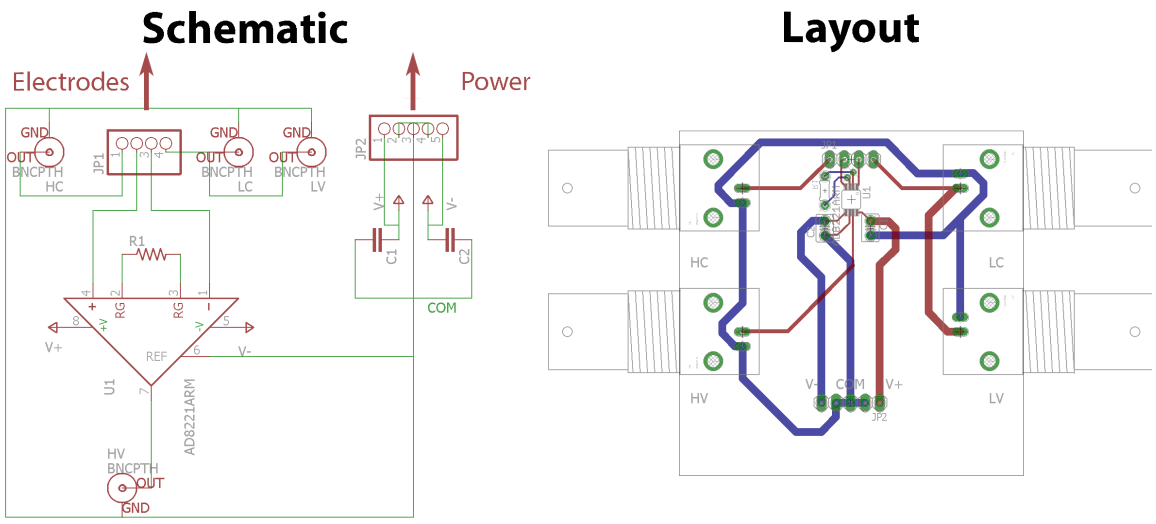

Figure 4.6: Printed circuit board schematic and layout for instrumentation used to interface between the microelectrode array and impedance analyzer.

Reducing interface impedance with PEDOT:PSS deposition

In order to reduce the electrical double layer impedance, the conducting polymer poly(3,4-ethylenedioxythiophene):poly(styrene sulfonate) (PEDOT:PSS) was electropolymerized on the surface of the geometrically smooth current-injection electrodes. PEDOT:PSS deposited in this way typically forms a porous, high effective surface area structure that reduces the double layer impedance [188], [189]. To prepare the electropolymerization solution, monomer 3,4-ethylenedioxythiophene (EDOT) was dissolved to a molarity of 10 mM in deionized water and PSS was added to a PSS/EDOT mass ratio of 1.5:1. The electrodes were covered by a droplet of the electropolymerization solution, and a Keithley 2400 SourceMeter (Keithley, Beaverton, OR) drove a 50 nA current between the electrode to be coated and a tungsten probe tip used as a counter electrode for 30 seconds, with a potential that varied from 0.8 V to 1.2 V. This process was repeated for each 100 µm square current-injection electrode. A microscope image of the electrodes after PEDOT:PSS deposition is in Figure 4.7, showing the deposited dark blue PEDOT:PSS film.

4.3.3 Electrical characterization

Impedance spectra were measured with an E4980AL impedance analyzer (Keysight Technologies, Santa Rosa, CA) from 100 Hz to 100 kHz in 10 mM KCl before and after PEDOT:PSS deposition and the results are shown in Figure 4.8. Before PEDOT:PSS was deposited, the measured impedance had a phase angle of $-70°$ to $-90°$ between 1 kHz and 100 kHz, indicating that the measurement was dominated by the interface impedances with

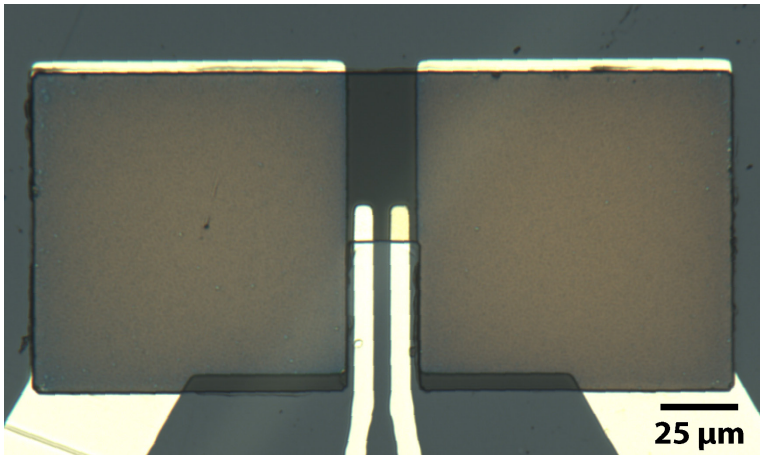

Figure 4.7: Microscope image of electrode array after electrodeposition of PEDOT:PSS, which has a dark blue color. The untreated electrodes are still gold.

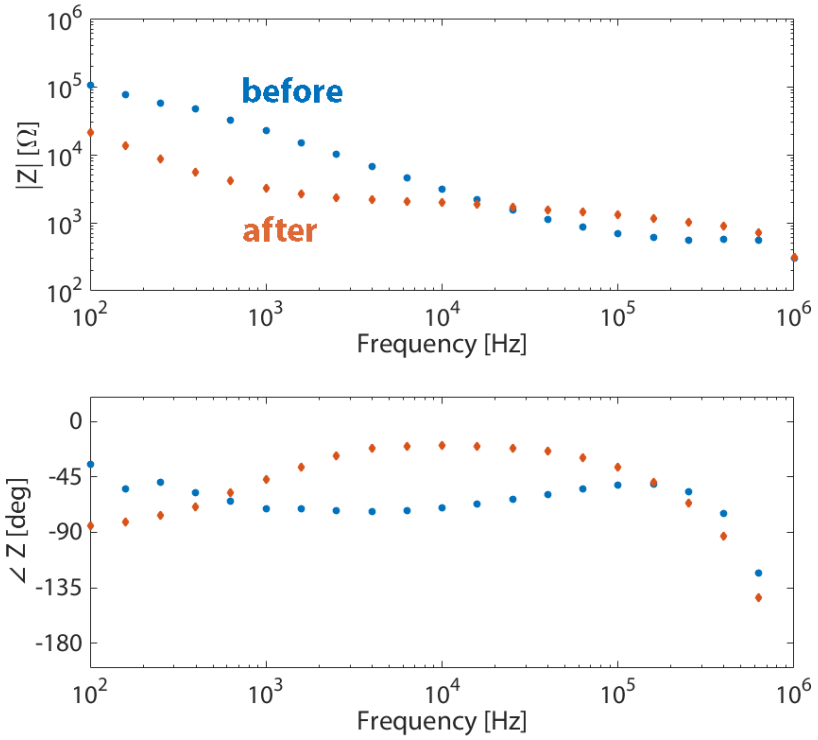

Figure 4.8: Impedance spectra for the electrode array immersed in 10 mM KCl before (blue circles) and after (red diamonds) PEDOT:PSS deposition. A 200 mV amplitude stimulus was used.

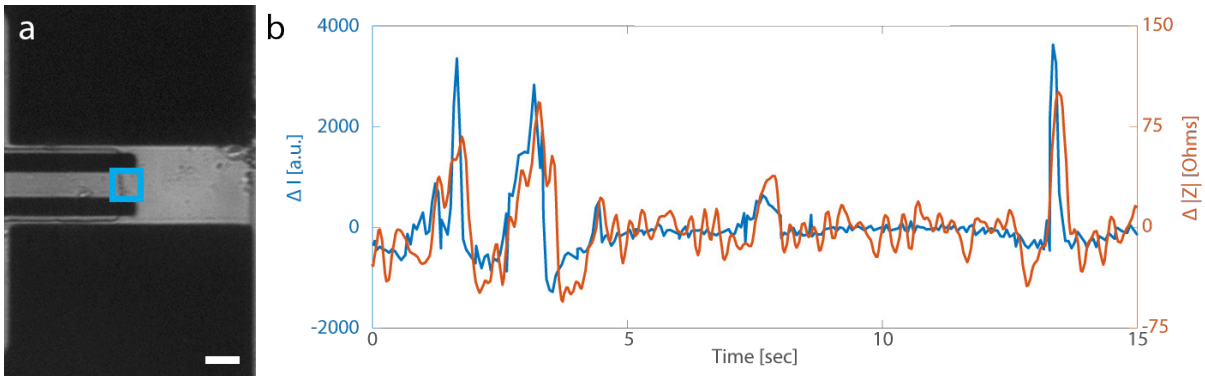

Figure 4.9: Correlation of impedance signal to bead passes. (a) Bright field view of electrode array as 2 µm diameter fluorescently labeled polystyrene beads pass over. Scale bar is 10 µm. (b) The resulting synchronized fluorescence and impedance measurements. The fluorescence signal (blue, $\lambda_{ex} = 495\,\text{nm}$, $\lambda_{em} = 519\,\text{nm}$) was summed in the blue square region between the electrodes as indicated in (a). The 10 kHz impedance signal (red) was processed by a DC notch filter to remove drift.

the expected constant phase element behavior. After PEDOT:PSS was deposited, a relatively constant R_{sol} of 20 kΩ was measured from 5 kHz to 50 kHz with a phase angle of −20° to 0°. Thus, PEDOT:PSS deposition reduced interface impedance enough to allow for successful solution resistance measurement. Given this capability to measure R_{sol}, the arrays should also be able to detect dielectric beads.

4.3.4 Detection of dielectric beads with high spatio-temporal resolution

As an initial test for these arrays, 2 µm diameter beads were flowed over the electrodes using the assembly pictured in Figure 4.4 [150]. The assembly was imaged on an inverted Olympus IX81 fluorescence microscope (Olympus America) using a Xe lamp light source and the appropriate filter set for Alexa Fluor 647 dye with a 50X long working distance objective (Mitutoyo, Japan). Passive siphon-driven flow moved 2 µm diameter fluorescent polystyrene beads (Bangs Laboratories, Fishers, IN) over the array while impedance was recorded at 10 kHz by a Keysight E4980AL impedance analyzer.

Representative results from the synchronized optical and 10 kHz impedance measurements in Figure 4.9 demonstrate detection of 2 µm diameter fluorescent polystyrene beads as they flowed across the array with good temporal agreement. The intensity of the fluorescence signal within the 4 µm by 4 µm region between the potential sense electrodes is co-plotted with the measured impedance change. Each bead caused an increase in impedance as it passed over the electrode array, with an SNR of 7 dB for the strongest impedance changes. The height of the bead relative to the electrodes was not well-resolved by the long working

distance objective used (Mitutoyo, Japan) and could have varied from 1 µm to 10 µm [150]. However, higher bead passes generally resulted in less significant impedance changes. Beads that did not pass directly over the sense electrodes were not detected, suggesting spatial resolution within 4 µm. The impedance measurements were sampled at a rate of 33 Hz, which is sufficient for measuring labeled flagellar rotation up to the Nyquist frequency of about 16 Hz. With this capability complete, we moved on to labeling flagellar motor rotation with polystyrene beads and other dielectric materials.

4.4 Labeling BFM rotation with dielectric beads

In this section, we cover a number of techniques that we developed in order to label flagellar motor rotation with a large radius of rotation, pictured in Figure 4.10. First, we cover the simplest method: attaching spherical polystyrene beads to unsheared flagella. Then, we discuss the fabrication and tethering of polystyrene bead pair duplexes to flagella [168]. Finally, we introduce the fabrication of the first photolithographically patterned silica beads for the BFM [150]. Ultimately, the simplest method of single polystyrene bead labeling was used for the final demonstration, but all techniques are presented here for posterity.

For all the following, a flowcell was prepared using one of the following three techniques:

1. A well-established technique that uses two pieces of double-sided tape to affix coverglass to a microscope slide and define a fluidic channel, known as a "tunnel slide" [148].

2. A detachable "tunnel slide" made using two thin strips of polydimethylsiloxane (PDMS) clamped between two glass microscope slides (as pictured in Figure 4.11).

3. A vacuum grease-defined channel sandwiched between two glass microscope surfaces with fluidic inlet and outlet ports drilled through one slide (as described in Section 4.5.2).

4.4.1 Spherical bead labeling

A well-developed technique for studying the bacterial flagellar motor is to attach sheared sticky flagellin stubs to polystyrene beads [175]. The sizes of beads used in these assays are typically <1 µm, which would not be detectable by our impedance array. Additionally, sheared flagellar stubs typically rotate quickly, requiring high speed cameras (>100 fps) to capture bead rotation. A larger bead tethered to a longer flagellum would result in a slower, wider radius of rotation suitable for impedance measurements.

Bead Preparation

Polystyrene beads were purchased from two suppliers and could be used interchangeably. Fluorescent polymer beads with 520 nm emission were purchased from Bangs Laboratories

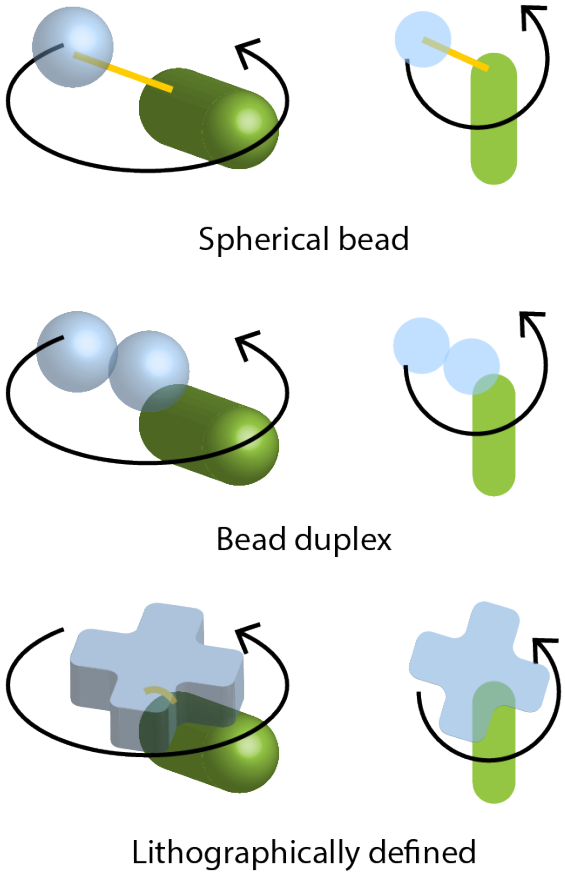

Figure 4.10: Methods for labelled flagellar motor rotation.

Inc. (Fishers, IN) and plain polystyrene beads were purchased from Polysciences Inc. (Warrington, PA). All beads used for tethering were 2 µm in diameter. Beads were diluted to 0.125% w/v in motility medium (10 mM KPO_4, 0.1 mM EDTA, 1 mM L-methionine, pH 7.0) prior to introduction to bacteria.

Cell Attachment

E. coli bacterial strain SYC12 (RP437 background, $\Delta fliC::fliC^{st}$), expresses a sticky flagellar filament and was used to demonstrate bead tethering. Bacteria were prepared by diluting 50 µL of overnight stationary culture grown in LB into 5 mL fresh T-broth (1 % w/v tryptone, 0.5 % w/v NaCl) in a 50 mL Falcon tube for aeration. Growth commenced at 30 °C with 250 rpm shaking until the culture reached an OD_{600} of 0.4-0.6 (approximately 5 hours). After reaching mid-exponential phase, the bacteria were left overnight (>12 hours) at room temperature without shaking. This added overnight growth step greatly improved the efficiency of bead tethering as shown in Figure 4.12. When ready to tether, the bacteria

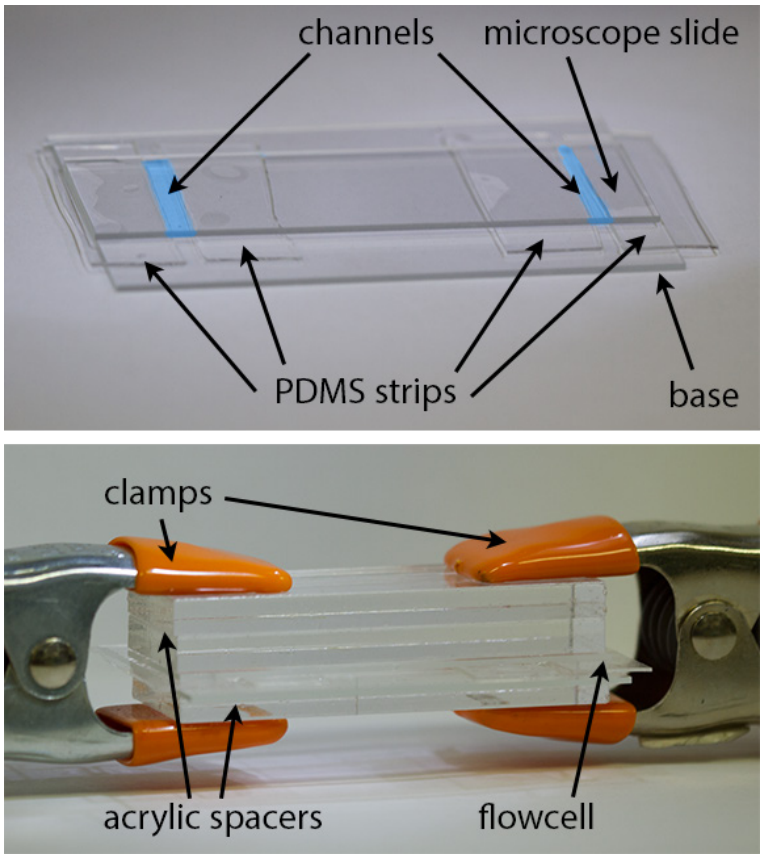

Figure 4.11: PDMS-based "tunnel slide." Acrylic spacers are used to more evenly distribute clamping force.

were pelleted by centrifugation at 4000 rcf for 5 min and washed twice in motility medium (10 mM KPO_4, 0.1 mM EDTA, 1 mM L-methionine, pH 7.0) and resuspended to an OD_{600} of 1.0.

Poly-L-lysine (PLL) was diluted in water to 0.01% w/v, passed through the channel, and immediately rinsed by motility medium. This thin layer of PLL readily adhered to silica surfaces and greatly enhanced bacterial adhesion. If PLL was given too much time to settle in the flowcell, multiple layers would be deposited and could potentially affect cell viability [190]. Then, the prepared bacterial suspension was introduced to the flowcell and allowed to settle and attach for 30 minutes. After this time, unattached bacteria were flushed with fresh motility medium. Then, the bead suspension was introduced and imaged without washing. Figure 4.13 shows a representative time lapse of bead rotation, including an image of the standard deviation calculated across the images to visualize the bead's motion. By electing to not shorten the flagellar filaments by shearing, some beads became attached to the end of long filaments for a wide radius of rotation (up to 2 µm) with a slower frequency of 2-8 Hz that should be conducive to large impedance variations suitable for electrochemical

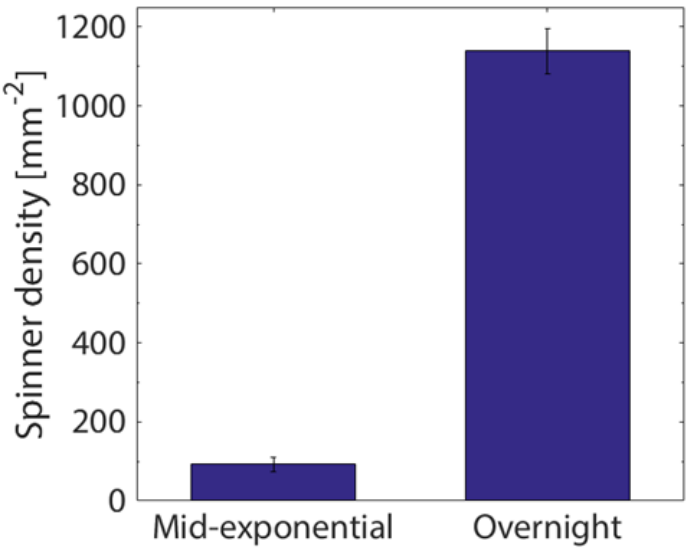

Figure 4.12: Leaving mid-exponential phase bacteria at room temperature overnight enhances bead tethering efficiency. Density of BFM-driven 2 µm beads for mid-exponential growth bacteria averaged 92 spinners per mm^2, while bacteria left at room temperature overnight averaged 1139 spinners per mm^2. The number of tethered spinning beads visible in an imaging field of 240 µm x 150 µm were counted across three fields and the average spinner density per mm^2 was calculated. Error bars mark standard error.

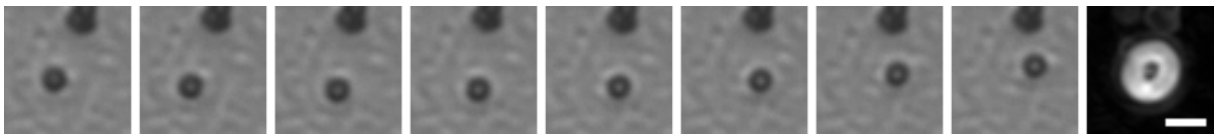

Figure 4.13: Bright field time lapse of BFM-driven clockwise bead rotation across 700 ms. Final frame is the standard deviation at each pixel, showing the path of the bead rotation. Frames are separated by 100 ms. Scale bar is 4 µm.

observation.

4.4.2 Bead duplex labeling

In order to more reliably increase the radius of rotation, an attempt was made to isolate bead pairs adsorbed together, which spontaneously arose when beads were allowed to aggregate in high concentration salt solutions [168]. These bead duplexes formed a makeshift rod structure that, when rotated about one end, had a radius of rotation of up to 4 µm.

Preparation

Beads were prepared following a protocol adapted from Pilizota et al. [168]. Polystyrene beads are typically manufactured with a slight static charge to prevent clumping. This charge was screened by suspending beads to a concentration of 2% w/v in 400 mM KCl and sonicating in a water bath for 30 min. Afterwards, the beads were washed three times in motility medium and resuspended to a storage concentration of 1% w/v. After this procedure, roughly 15% of the beads were found to be in bead duplexes.

To isolate these bead duplexes from single beads, density gradient centrifugation was performed across a 5% to 10% sucrose gradient. The gradient was established in a polypropylene ultracentrifuge tube using a tilted tube rotation method with a BioComp Gradient Master 108 (BioComp Instruments, Fredericton, NB) [191]. The beads were carefully loaded on the top of the sucrose gradient by expelling up to 200 µL by slowly twisting the pipette's volume adjustment knob to gradually expel the bead suspension held by the pipette tip. If the beads were loaded too quickly, they mixed with the gradient and did not separate well. Once the beads were loaded, they were spun to 3000 rcf in a swinging bucket ultracentrifuge (using an SW41 rotor, Beckman Coulter, Brea, CA) for one minute, then allowed to spin to a stop without any braking, which usually took about 10 minutes. By slowly coasting to a stop, shear forces at the sidewalls of the tube were reduced to minimize spreading of the bands, leading to distinct separation (Figure 4.14a). Ultraviolet light was used to better visualize the fluorescent bead bands. The end of a 1 mL pipette tip was cut off to widen its inlet and it was used to draw up the band consisting of bead pairs. The beads were imaged using fluorescence microscopy afterwards, showing that roughly 50% of beads were now in duplexes (Figure 4.14b).

Cell Attachment

E. coli bacterial strain SYC12 (RP437 background, $\Delta fliC::fliC^{st}$), was once again used to demonstrate bead tethering. Bacteria were grown and bead pairs were attached to immobilized cells using the same method described in Section 4.4.1. Figure 4.15 shows a representative time lapse of BFM-driven bead duplex, including an image of the standard deviation calculated across the images to visualize the duplex's motion. The load of a duplex

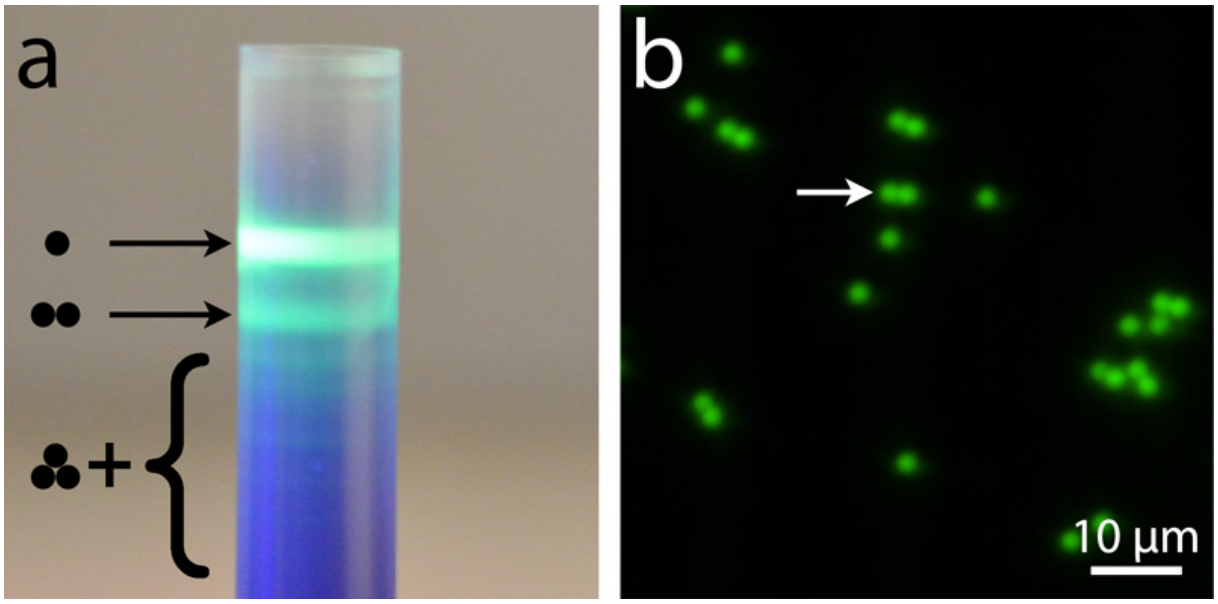

Figure 4.14: Bead duplexes. (a) After density gradient centrifugation, several distinct bands are visible, having been separated by cluster size. (b) Fluorescence microscopy (green, λ_{ex} = 495 nm, λ_{em} = 519 nm) showing the enrichment of bead duplexes after density gradient centrifugation.

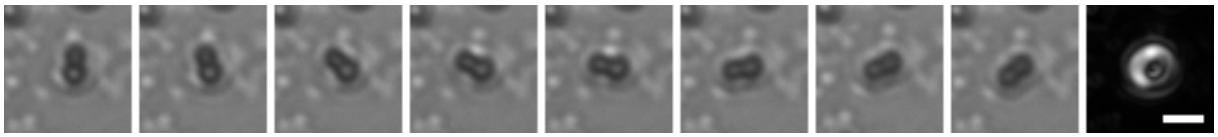

Figure 4.15: Bright field time lapse of BFM-driven bead duplex rotation across 700 ms. Final frame is the standard deviation at each pixel, showing the path of the bead rotation. Frames are separated by 100 ms. Scale bar is 4 µm.

on the BFM was larger than that of a single bead, so these assemblies rotated at a lower frequency of 1-2 Hz.

4.4.3 Lithographically defined beads

We also designed the first lithographically-defined silica beads to label the flagellar motor, which use streptavidin-biotin chemistry to attach the beads. These ultimately were not used beyond an initial demonstration since the dense silica beads often stuck to the coverglass and thus were difficult for the bacteria to continue rotating for extended periods.

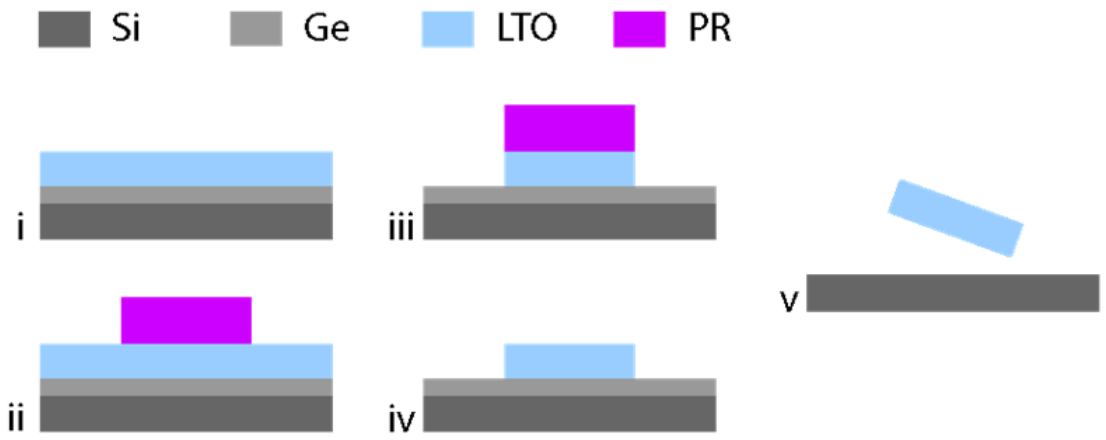

Figure 4.16: Silica bead fabrication process. (i) Deposition of Ge and low temperature oxide (LTO) by LPCVD. (ii) Patterning of photoresist. (iii) Plasma etch of beads. (iv) Removal of photoresist by oxygen plasma. (v) Release in 3.0 % hydrogen peroxide.

Fabrication

The rod fabrication process is presented in Figure 4.16 and took place on 675 µm thick 6″ p-type test grade silicon wafers. First, a 400 nm sacrificial layer of germanium was deposited by low pressure chemical vapor deposition (LPCVD) (Tylan furnace, 340 °C, 600 mTorr, 90 sccm GeH_4), immediately followed by 650 nm of low temperature oxide (LTO) by LPCVD (Tylan furnace, 450 °C, 300 mTorr, 90 sccm SiH_4, 135 sccm O_2). Second, a standard DUV photoresist (UV210-0.6, Dow chemical, Midland, MI) and a deep UV stepper lithography tool (ASML 5500/300) were used to pattern a photoresist mask that defined the beads. 4×10^6 beads fit onto 1 cm^2, yielding 5×10^8 beads per wafer. After patterning, the resist was UV hard baked to improve etch selectivity. Third, LTO was etched in a reactive-ion etcher to form the beads (Lam Research, 70mTorr, 150 sccm Ar, 25 sccm CHF_3, 25 sccm CF_4, 750 W RF power, 90 sec). Gold patches were then optionally patterned on the beads (if thiol click chemistry [192] was desired) by a second round of liftoff. A wafer at this stage is illustrated in Figure 4.17

Finally, the wafer was immersed in 3.0 % hydrogen peroxide for 2 h at room temperature to dissolve the Ge sacrificial layer [193], [194] and release the beads. Deionized water was then sprayed across the surface of the wafer to remove the beads and collect them in a centrifuge tube as shown in Figure 4.18. The beads were centrifuged at 6000 rcf for 10 min, resuspended in 1 mL ethanol, and washed 3 times in 1 mL ethanol. Released beads are shown in Figure 4.19. More detailed process notes are presented in Appendix A.

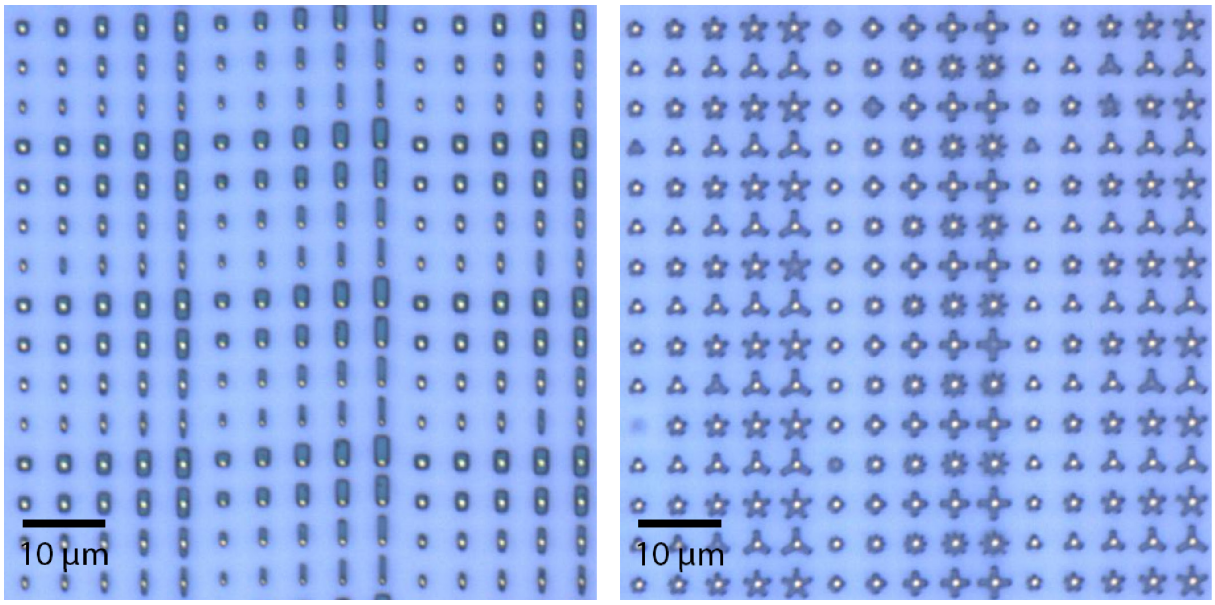

Figure 4.17: Wafer-scale array of (Left) silica rod and (Right) wheel-shaped beads with optional gold patches for thiol-based surface functionalization. Imaged on an Olympus LEXT OLS3000 Confocal Microscope in snapshot mode.

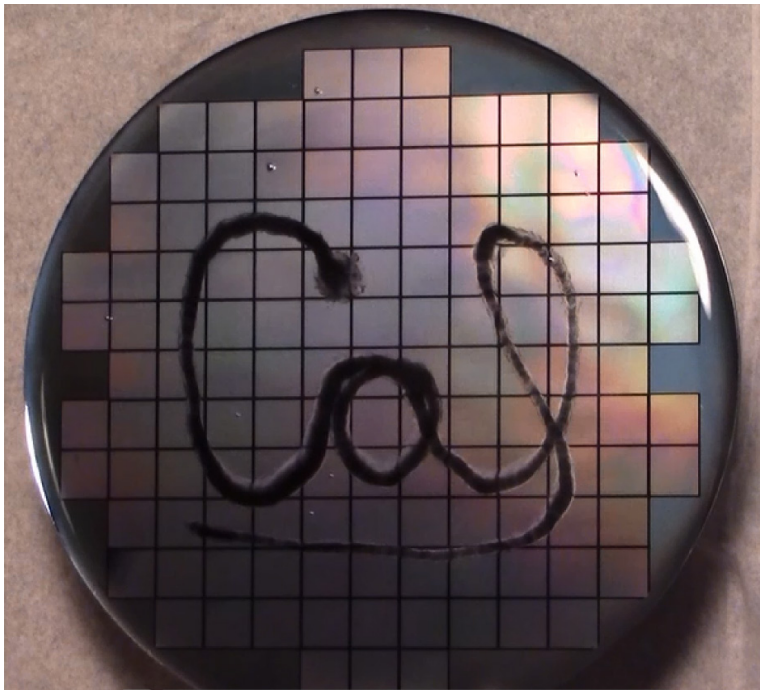

Figure 4.18: Wafer after dissolution of sacrificial germanium layer. Silica beads have been lifted off along the shape of a script 'Cal' delivered by a spray of deionized water.

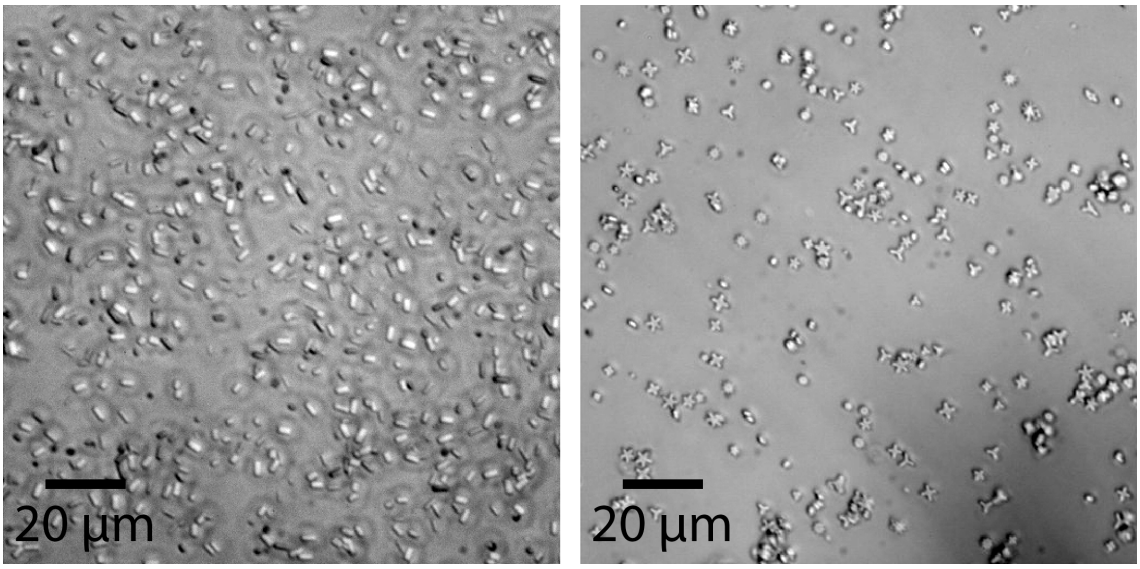

Figure 4.19: Phase contrast image of free-floating silica rod and wheel-type beads after release.

Functionalization

To functionalize the beads with biotin, the following method was used, based on a number of procedures reported in the literature [195]–[198]. In order to clean the beads and leave activated hydroxyl groups, they were spun down and resuspended in 10 mM NaOH and then sonicated at 50 °C for 20 min. Then, the beads were pelleted at 6000 rcf for 2 min and rinsed 3 times in 1 mL deionized water. Finally, the beads were resuspended in 100 µL deionized water and dehydrated in a centrivac at 60 °C for 30 min.

While the beads were dehydrating, silane-PEG-biotin (MW2000, Laysan Biosciences, Arab, Al) was dissolved into an ethanolic solution (95 % ethanol, 5 % deionized water, pH adjusted to 5.5 by glacial acetic acid) to 20 mg mL^{-1} and sonicated for 30 min for dissolution and hydrolyzation. The activated silane solution was added to the dehydrated beads and vortexed for 20 min at room temperature. The suspension was pelleted at 6000 rcf for 2 min and rinsed 3 times in 1 mL ethanol. Finally, the beads were resuspended in 100 µL ethanol and dehydrated in a centrivac at 60 °C for 45 min to complete the condensation reaction that covalently bonded the silane to the activated silica surface. Finally, the beads were resuspended in 500 µL pH 7.4 phosphate-buffered saline (PBS) for streptavidin functionalization.

To visualize the efficacy of biotinylation, the beads were conjugated to fluorescent streptavidin-FITC (Sigma Aldrich, St. Louis, MO). Rods not subjected to the biotinylation procedure above were washed and resuspended in 500 µL PBS for comparison with the biotinylated rods. Then, streptavidin-FITC from a stock solution of 1 mg mL^{-1} was added to the bead suspensions for a final concentration of 1 µg mL^{-1}. The suspensions were shaken at room temperature for 60 min at 150 rpm in the dark. The surfactant Tween-20 was then

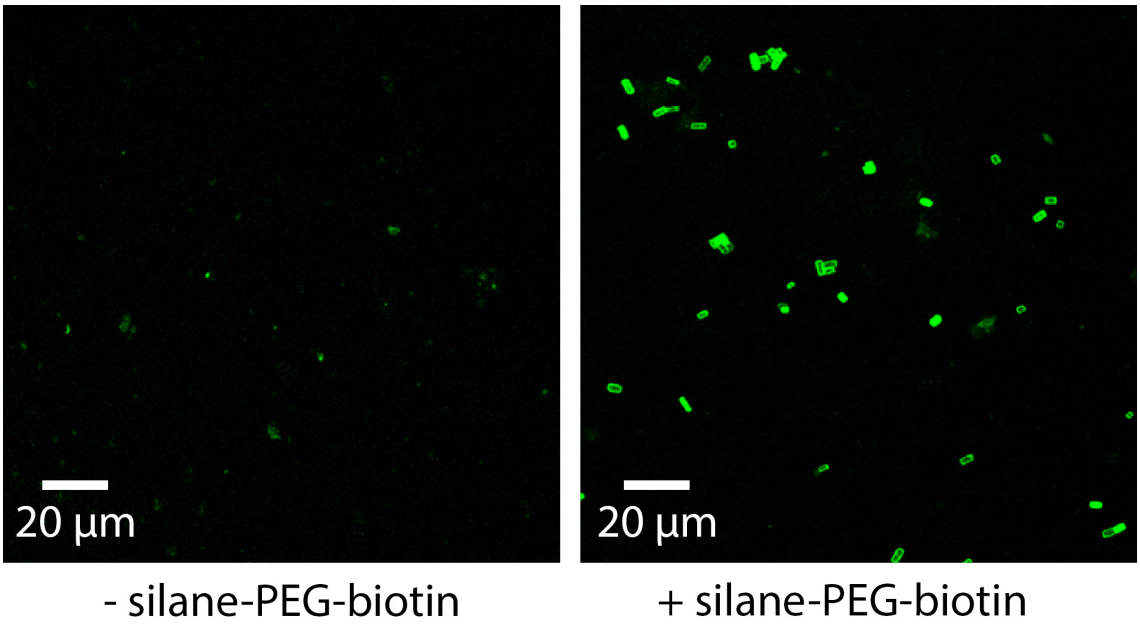

Figure 4.20: Silica rods functionalized with streptavidin-FITC, (Left) without silane-PEG-biotin functionalization and (Right) with silane-PEG-biotin functionalization. Some non-specific binding of streptavidin to non-biotinylated silica is observed, but a significantly higher streptavidin capture efficiency resulted from prior biotinylation.

added to 0.1 % to each of the bead suspensions to prevent the beads from adhering to the sides of the microcentrifuge tubes. The suspensions were pelleted at 6000 rcf for 2 min and rinsed 3 times in 500 µL PBS. A 1 µL drop of cleaned beads were placed under a 1 cm by 1 cm 1 % agarose pad on a glass coverslip. The samples were imaged on a Zeiss LSM710 Confocal Microscope using a 405 nm laser. The results are shown in 4.20, and demonstrate a significantly higher streptavidin capture efficiency resulting from the biotinylation protocol.

Cell Attachment

With the beads labeled by streptavidin, a biotinylated surface on the flagellum was necessary to complete the attachment. The MTB32 *E. coli* strain used in these experiments suppresses the flagellar filament and expresses a biotin accepting peptide (BAP) sequence on the flagellar hook (RP437 background, Δ*fliC*, *flgE*-BAP) [169].

These cells were grown from stationary overnight culture in 3 mL T-broth (1 % w/v tryptone, 0.5 % w/v NaCl) at 30 °C with 250 rpm shaking to an OD_{600} of 0.4. Then the cells were spun in a centrifuge at 1000 rcf for 1 min and washed twice in motility medium (10 mM KPO_4, 0.1 mM EDTA, 1 mM L-methionine, pH 7.0). Cell hooks were then biotinylated by resuspension in 80 µL of motility medium, 10 µL of BiomixA (0.5 M bicine buffer, pH 8.3), 10 µL of BiomixB (100 mM ATP, 100 mM $Mg(OAc)_2$, 500 µM D-biotin), and 1 µg BirA

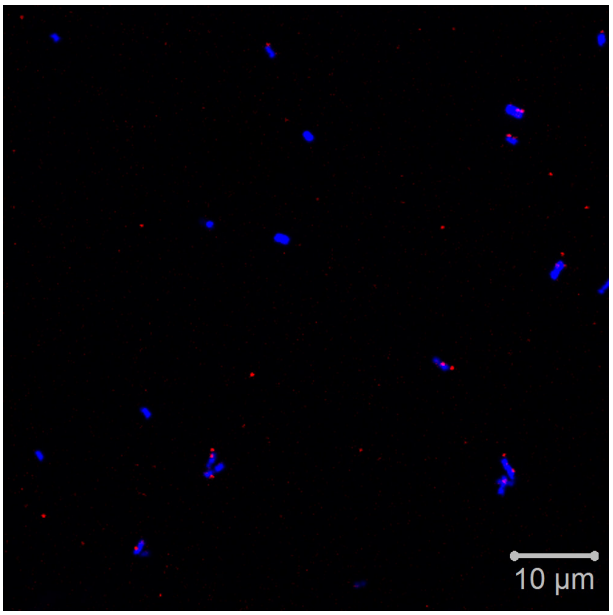

Figure 4.21: Confocal microscope image of biotinylated flagellar hooks. Bacteria were stained by DAPI (blue, $\lambda_{ex} = 358\,\text{nm}$, $\lambda_{em} = 461\,\text{nm}$) and their biotinylated hooks were tagged by neutravidin-AlexaFluor647 (red).

Figure 4.22: Bright field time lapse of BFM-driven clockwise bead rotation across 700 ms. Final frame is the standard deviation at each pixel, showing the path of the bead rotation. Frames are separated by 100 ms. Scale bar is 4 µm.

(reactants supplied by Avidity, Boulder, CO). The biotinylation proceeded for 90 min at room temperature with agitation at 150 rpm, then the cells were washed 3 times in motility medium. For confocal characterization, cells were incubated with $10\,\mu\text{g}\,\text{mL}^{-1}$ neutravidin labeled by AlexaFluor 647 dye (Thermo Fisher, Waltham, MA) for 20 min, washed 3 times, resuspended in 150 µL motility medium, and finally stained by 1 µM DAPI for 5 min. The labeled hooks were imaged with confocal microscopy and are shown in Figure 4.21, with bacteria in blue and labeled hooks in red.

Functionalization of the hooks and beads resulted in BFM-driven rotation of silica beads 4 µm in diameter at a frequency of 2 Hz as shown in the time lapse in Figure 4.22. This rotation rate was similar to the rotation of motors loaded by polystyrene bead duplexes. With many flagellar labeling techniques now tested, it was time to deliver a rotating bead to the electrode array's recording site for electronic observation.

4.5 Delivering a labeled BFM to the recording site with micrometer precision

So far in this chapter, we have described two contributions towards developing an electronic readout of BFM rotation for a biohybrid sensor:

1. The fabrication and testing of a microelectrode array to measure solution resistance in a microscale area

2. The labeling of the bacterial flagellar motor with a dielectric bead

The following section addresses the final challenge of integration: the delivery of a spinning bead to the microscale recording site of the microelectrode array.

4.5.1 Platform for simultaneous microscopy and impedance measurement

To enable delivery of a labeled BFM to the recording site, we engineered a custom platform capable of simultaneously recording a microscope stream and four-point electrochemical impedance measurements with an integrated flow channel. To allow for fine positioning, the microelectrode array was attached to a micromanuplator using a custom-built mount and imaged at a probe station as shown in Figure 4.23. With this arrangement, bacteria were immobilized on a glass slide in a flow channel 5 to 10 micrometers in thickness sealed by vacuum grease [199]. The microscope slide was clamped to the stage and to allow the electrode array to be repositioned relative to the bacteria tethered to the immobilized slide while the vacuum grease maintained the fluidic seal. Because the electrode array substrate was transparent, a BFM-driven rotating bead could be positioned and simultaneously imaged to verify the electronic measurement.

4.5.2 Platform assembly process

Each microelectrode device was assembled onto a platform for simultaneous optical and impedance measurements, as summarized in Figure 4.24. Briefly, an individual device was affixed to a printed circuit board with Crystalbond (SPI Supplies, Camden, NJ). Next, a fluidic inlet and outlet 2.5 mm in diameter were drilled through the device with a dental drill and a diamond-coated ball bit to facilitate fluid flow. A 3 mm thick piece of PDMS was placed under the array to support it throughout the drilling as shown in Figure 4.25, and the drilling was performed under water to reduce the production of volatile silica particles. With the holes drilled, silicone tubing (Tygon 1/3" ID x 3/3" OD, Saint-Gobain, La Défense, France) was inserted through each hole and sealed in place with a light-curable expoxy (Loctite 3526, Loctite, Düsseldorf, Germany). The tubing was cut with a razor blade to make it flush with the surface of the microelectrode array. Electrical connections to the interface PCB were

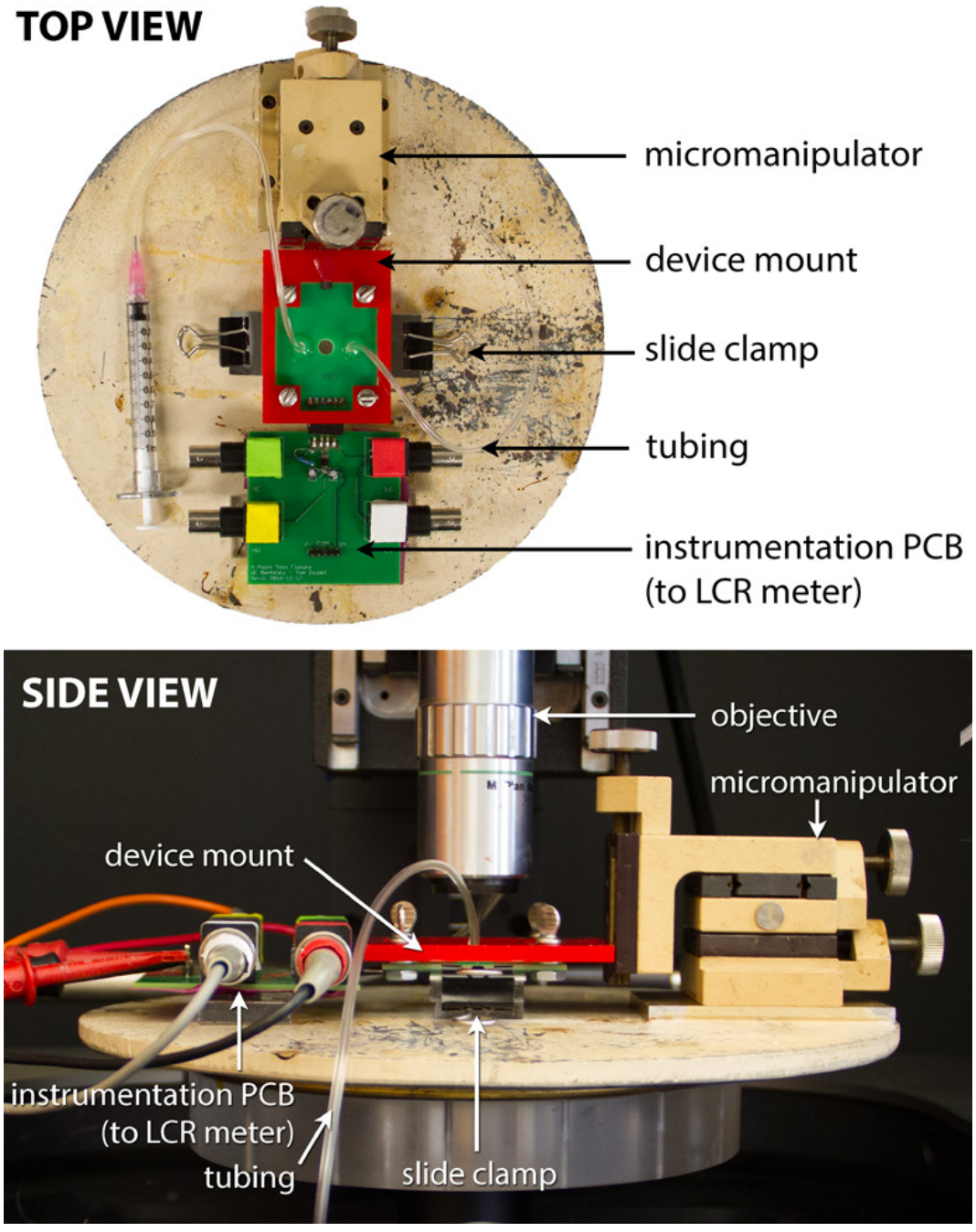

Figure 4.23: Complete setup at a probe station microscope. The slide coated with tethered spinners is clamped so that the micromaniuplator is free to align the device recording site with the desired spinner.

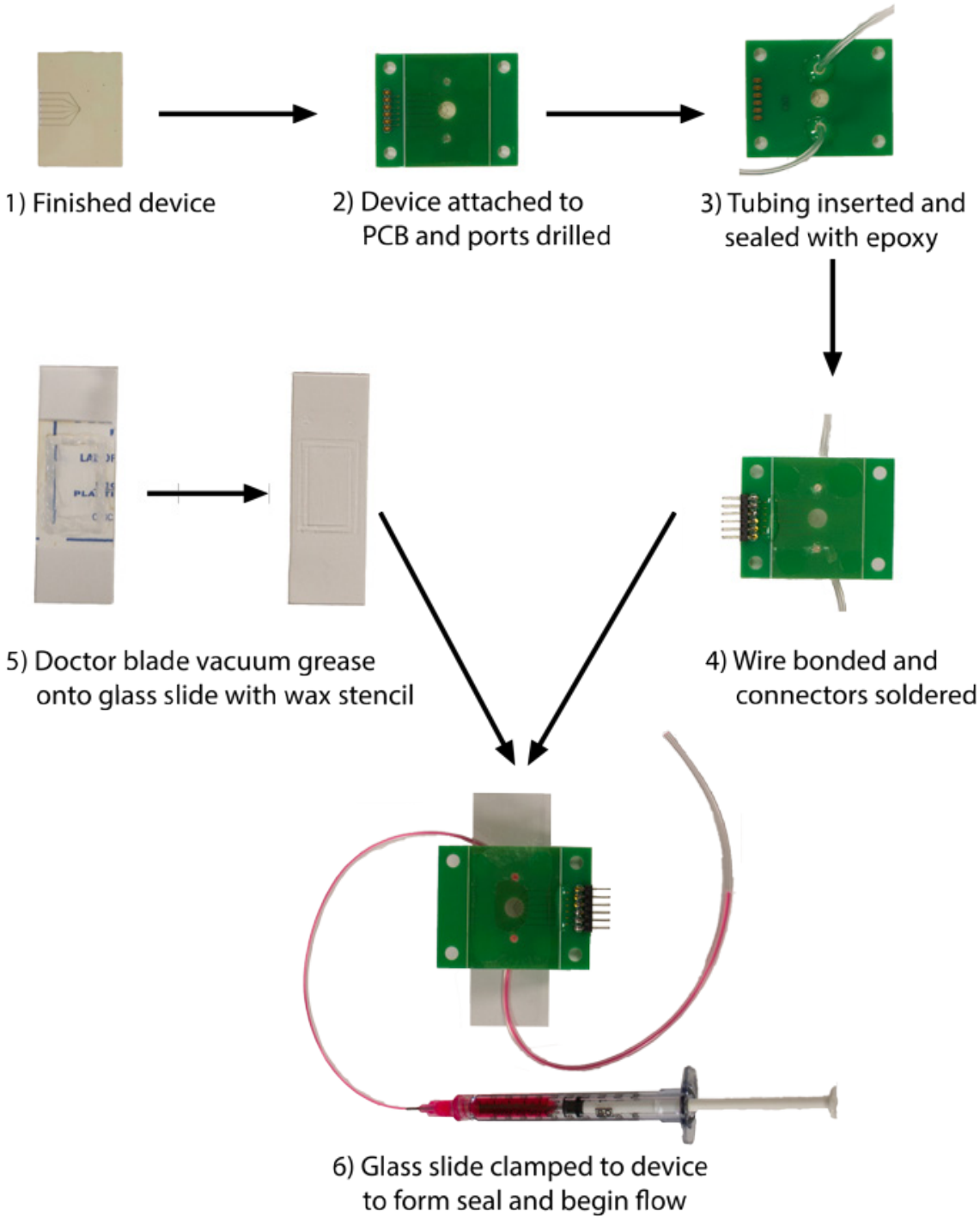

Figure 4.24: Summary of microelectrode array device and flowcell assembly process.

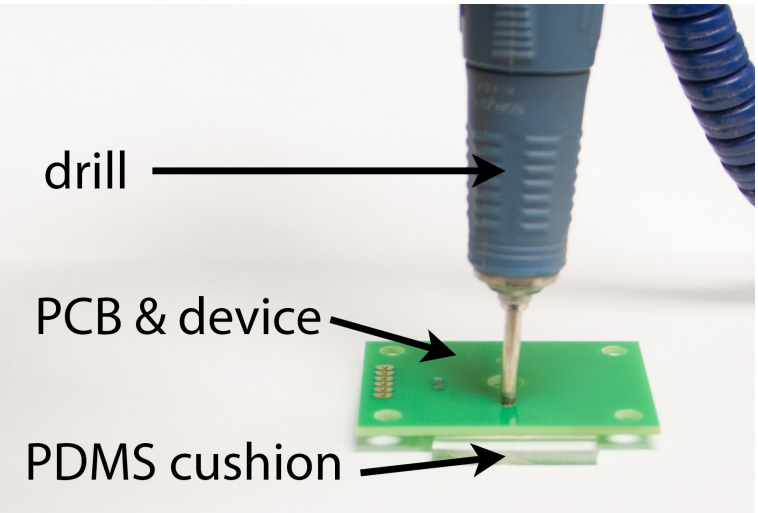

Figure 4.25: Demonstration of drilling fluidic ports through the microelectrode array device. A PDMS cushion is used to prevent cracking. Note that the actual drilling would take place with the device immersed underwater to prevent the production of volatile silica particles.

completed with Al wire using ultrasonic wedge wire-bonding (WestBond Inc., Anaheim, CA) and the connections were protected by light-curable epoxy.

A seal was made between the device and a glass microscope slide using vacuum grease that was patterned by a Parafilm wax stencil, forming a fluidic channel between the vacuum grease, electrodes, and glass slide. The slide was clamped to a mount that held it steady while the PCB and device were mounted to a three-axis micromanipulator, allowing the electrodes to be moved with respect to the stationary glass slide without breaking the fluidic seal. The entire assembly was imaged by a 20x long working distance objective (Mitutoyo, Japan) at an electronic probe station.

4.5.3 BFM-labeling protocol

E. coli bacterial strain SYC12 (RP437 background, $\Delta fliC::fliC^{st}$) was used. Bacteria were prepared by diluting 50 µL of overnight stationary culture grown in LB into 5 mL fresh T-broth (1 % w/v tryptone, 0.5 % w/v NaCl) in a 50 mL Falcon tube for aeration. Growth commenced at 30 °C with 250 rpm shaking until the culture had an OD_{600} of 0.4-0.6 (approximately 5 hours). After reaching mid-exponential phase, the bacteria were left overnight (>12 hours) at room temperature without shaking. When ready to tether, the bacteria were pelleted by centrifugation at 4000 rcf for 5 min, washed twice in motility medium (10 mM KPO_4, 0.1 mM EDTA, 1 mM L-methionine, pH 7.0) and resuspended to an OD_{600} of 1.0.

Poly-L-lysine (PLL) at 0.01% w/v was passed through the flow channel and immediately rinsed by motility medium. Then, the prepared bacterial suspension was introduced to the flowcell and allowed to settle and attach for 20 minutes. After this time, unattached bacteria

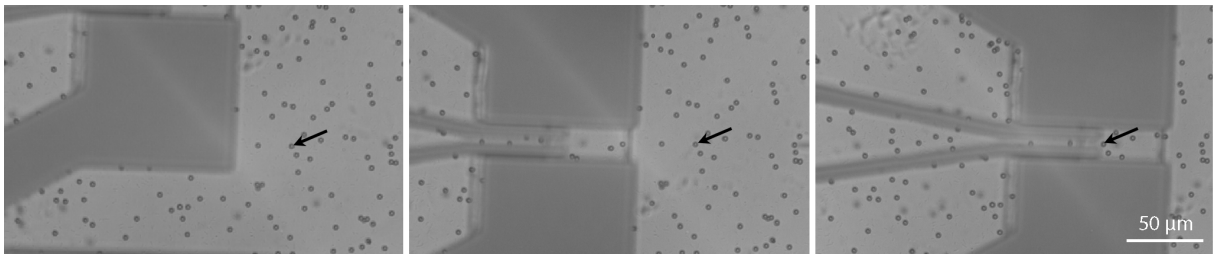

Figure 4.26: Demonstration of bead delivery. A micromaniuplator moves the electrodes towards the spinning bead marked by the black arrow.

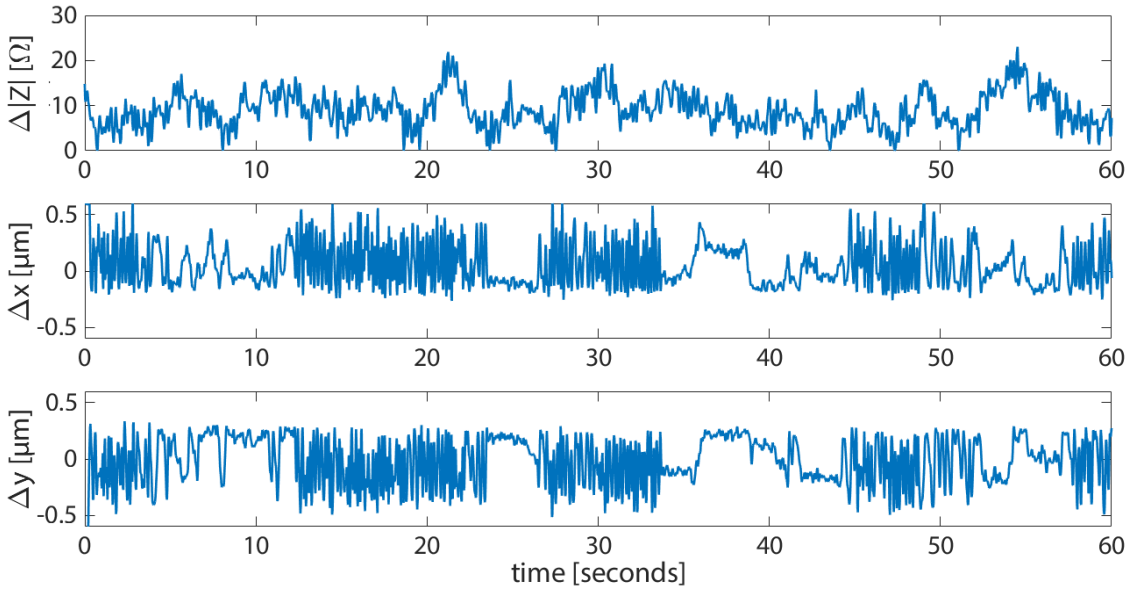

Figure 4.27: Results of attempted impedance-based observation of the flagellar motor. (a) The change in impedance above the baseline, (b) the flagellar-driven bead's x-position and (c) y-position synchronized to the impedance data.

were flushed away with fresh motility medium. Then, 2 µm beads were diluted to 0.125% w/v and introduced to the flowcell and given 5 minutes to attach to flagellar filaments. The entire assembly was then imaged at a probe station and the micromanipulators were used to deliver a spinning bead directly to the recording site as illustrated by Figure 4.26. Once positioned, impedance was recorded at 10 kHz for several minutes while a microscope image stream was simultaneously recorded.

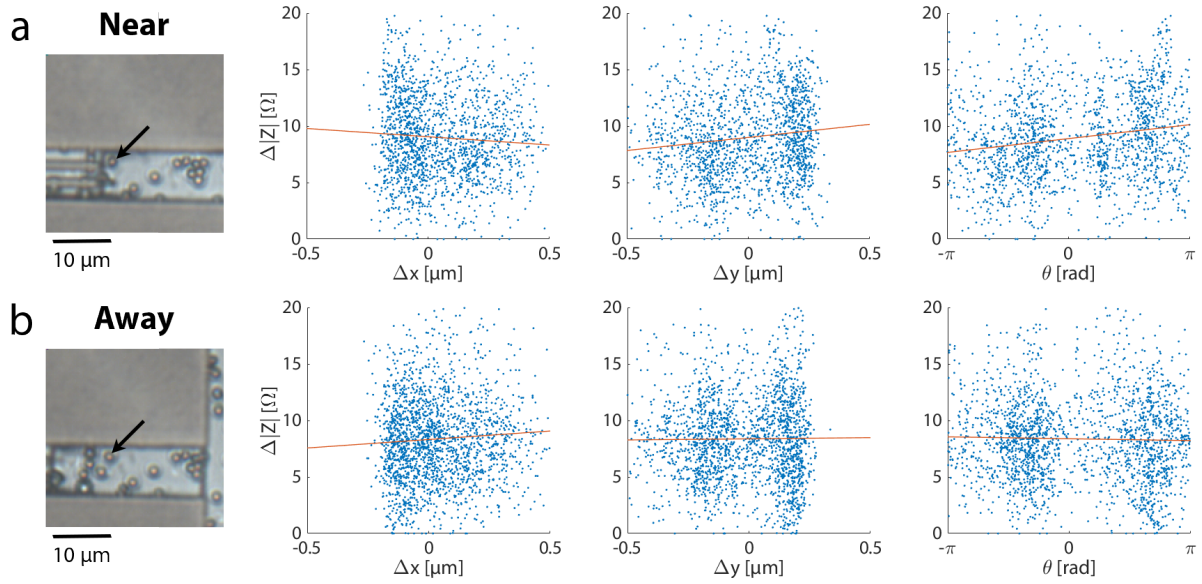

Figure 4.28: Weak correlation between bead position and change in impedance. Scatter plots comparing impedance change against x-position, y-position, and angle for (a) a bead rotating near the recording site and (b) away from the recording site. A black arrow points out the bead in a still frame taken from the microscope data. Red lines are linear least squares fits to the data.

4.5.4 Measurement results

The results for a typical experiment monitoring flagellar rotation are shown in Figure 4.27, where the change in impedance $\Delta|Z|$, the bead's x-displacement Δx, and the bead's y-displacement Δy are plotted against time. $\Delta|Z|$ at a given time was computed as the difference between the impedance measured at that time point and the baseline impedance signal (the mean of the lower 25th percentile of measurements in the surrounding 5-second window). Occasional slowing and stopping in bead rotation was observed. Also, during some intervals of interrupted bead rotation, impedance increased up to 20 Ω. Variations in impedance were generally low and subject to noise. Also, these variations were observed over timescales on the order of 2 seconds or longer, which is not fast enough to resolve the bead position rapidly enough to observe real-time BFM rotation.

Impedance was also plotted against bead displacement and is shown in Figure 4.28. A very weak linear trend appeared between y-position and impedance when the bead was spinning near the recording site (Figure 4.28a, Table 4.1). As rotation moved the bead farther from the recording site (increasing Δy), the measured impedance increased slightly. A similar relationship was seen when beads were flowed across the array in earlier experiments (Figure 4.9; impedance momentarily decreased, increased, and decreased again before returning to baseline as a bead passed across the recording site). A similar correlation was not observed

when the spinning bead was moved away from the recording site (Figure 4.28b). However, measurement noise resulted in a wide spread of the impedance measurements. The standard deviation in $\Delta|Z|$ was $3.8\,\Omega$ while the largest change in impedance was $2.32\,\Omega\,\mu m^{-1}$, so the data is inconclusive. Either a stronger trend or reduced noise would be required to resolve bead position from this impedance data.

Table 4.1: Linear fits to $\Delta|Z|$ [Ω] versus bead displacement [µm] or angle [deg] for a flagellar-driven spinning bead near to and away from the recording site.

Bead position	$\Delta\|Z\|(\Delta x)$	$\Delta\|Z\|(\Delta y)$	$\Delta\|Z\|(\theta)$
Near	$9.05 - 1.46\Delta x$	$8.99 + 2.32\Delta y$	$8.89 + 0.39\theta$
Away	$8.31 - 1.50\Delta x$	$8.38 - 0.21\Delta y$	$8.38 - 0.053\theta$

4.6 Discussion

In this chapter, we have presented solutions to three problems necessary to enable electronic flagellar observation. First, we fabricated and tested electrode arrays capable of measuring electrochemical impedance within a microscale recording site. Second, we labeled the rotation of a bacterial flagellar motor by a dielectric bead with a radius of rotation up to 2 µm. Third, we developed a method to deliver a bead-labeled flagellar motor directly to the microscale recording site. However, when these techniques were integrated together into one system, flagellar rotation could not be completely resolved electronically. In this section, we will identify the remaining issues that need to be addressed for a successful demonstration of electronic flagellar observation, and then consider directions for future development.

4.6.1 Current issues

The first issue is that although our electrode arrays were able to resolve individual bead passes, the variation in impedance caused by a rotating bead was much smaller than our system could resolve. The largest possible change in impedance occurs when a bead directly passes over the array, with up to 7 dB SNR as seen in Figure 4.9, because the bead completely enters and then leaves the recording site. In the case of a rotating bead, the bead is always partially within the recording site, so the resultant variation in impedance is naturally lower. If the area of the recording site could be reduced further to the sub-micron scale, the movement of a rotating bead would have a larger impact on measured impedance. Ideally, both the current injection electrodes and potential pickup electrodes would be made smaller to concentrate the electric field to the smaller recording site. Additionally, we could increase the radius of rotation by using asymmetric beads like the silica rods we fabricated in Section 4.4.3. The issue with our silica rods is that they were dense ($2\,g\,cm^{-3}$ density) and quickly became stuck to the electrode array surface, but similar beads made out of polystyrene ($1.05\,g\,cm^{-3}$ density) or a neutrally buoyant material would allow for asymmetric beads to

be driven without overloading the flagellar motor, displacing a higher volume of media at the recording site to increase the perturbation of impedance.

We were also constrained by the frequency we could use for impedance measurements. Above 100 kHz, the parasitic capacitances of cabling and the instrumentation amplifier began to dominate the measured impedance. This required our electrode arrays to use larger current injection electrodes. If we were to reduce the electrode size, the measurement frequency would have to increase to counter the increase in double layer impedance. For example, reducing the dimensions of the current injection electrodes from 100 µm on a side to 10 µm on a side would increase the interface impedance by a factor of 100x, so the measurement frequency would have to increase from 10 kHz to 1 MHz. This would only be possible if parasitic impedances were reduced by using instrumentation with a wider frequency response or by reducing parasitics caused by cabling and connectors.

Finally, since we are primarily interested in measuring solution resistance and not necessarily the electrochemical impedance spectrum, more specialized instrumentation could be used. The Keysight E4980AL impedance analyzer has two limitations: a maximum measurement frequency of 1 MHz and a sampling speed limited to 40 samples per second at 10 kHz, due to its auto-balancing bridge measurement method. With a custom setup, voltage measurements could be taken at a high sampling rate with an oscilloscope while a signal generator perturbs the electrode array at one frequency. Additionally, a lock-in amplifier could be used to cut down on noise and enable the tracking of small changes in impedance that we expect to observe.

4.6.2 Future potential

Assuming that electronic flagellar observation is successful, there are a number of potential directions and applications for further development. Consistent speed measurements would enable a proxy measurement of the proton motive force (PMF), a proton separation across the inner membrane that is of metabolic importance to *E. coli* and proportional to motor speed [104], [141]. A reduction in PMF coupled directly to the flagellar motor speed could indicate the presence of toxic ionophores [141], or changes of redox potential in the environment that impact affect cell health [200]. An electronic BFM monitoring method could also eventually enable miniaturization of PMF-based sensing systems, and also enable closed loop control for BFM microactuation for microrobotics as stimulation strategies continue to advance [142], [201]–[203]. High-speed impedance measurements could also extract rotation direction, which could be used to monitor flagellar rotation bias. This would allow for detection of chemoeffector concentration and type when combined with *a priori* knowledge of motor response as demonstrated in Chapter 3 [95].

The most promising direction would be to use an application specific integrated circuit (ASIC) to multiplex this measurement to hundreds of recording sites on a single device. Ideally, integrated low-noise amplification would enable label-free detection of the bacteria, so that the rotation of hundreds of cell bodies tethered by their flagella could be recorded without the extra complication of BFM labeling. A custom ASIC would allow further reduc-

tion of parasitics, enabling high-frequency measurements with low-capacitance multiplexing and further electrode miniaturization. Such a chip could be used for bench top analysis of chemical samples, or potentially be integrated onto a low-power mobile aqueous sensing platform.

4.7 Conclusion

We have developed a platform that uses low-power electrochemical measurements to monitor bead-labeled flagellar motor rotation of a single *E. coli* cell. Ultimately, the variation of the impedance caused by the rotating bead was undetectable, but this issue could be addressed by modifying the instrumentation used to take the measurement. Once completed, our system could be used as a biohybrid sensor which combines the chemotactic response the BFM to low-power electrochemical readout. An impedance-based measurement could be scaled up to large ensembles of BFMs and enable new aqueous biohybrid sensing applications. Ultimately, label-free measurements that detect single spinner cells tethered by their flagella would make it easier to scale this technique towards a large multiplexed electrode array, allowing for monitoring of many cells with different genetic backgrounds for complex solution analysis.

Chapter 5

Closing Remarks

In this dissertation, we have presented several approaches to interface electronics with bacterial cells to produce biohybrid sensing systems. This work just scratches the surface; a bounty of useful nanoscale tools exist throughout the bacterial kingdom, but we focused on the Mtr electron transfer pathway in *Shewanella oneidensis* MR-1 and the chemotaxis system in *Escherichia coli*. On the abiotic side, we focused on electronic interfaces due to their inherently low power consumption. This emphasis was made to enable applications in persistent environmental sensing and microbiorobotics, which we briefly imagine in the paragraphs that follow.

From the environmental biosensing perspective, there is a need for inexpensive, persistent water quality monitoring in many industries. Whether checking for toxins like arsenic, or pollutants like BTEX (benzene, toluene, ethylbenzene, xylene), the prevailing method is to ship a sample to a mass spectrometry lab for analysis [58]. Therefore, sampling is costly and intermittent. A persistent biohybrid sensor, such as a pollutant-sensitive conductive bacterial film like the MCBF presented in Chapter 2, could be employed for more consistent monitoring.

It is worth noting that biosensing is just one of several open problems in the emerging area of microbiorobotics, which is concerned with the precise manipulation of microscale objects that utilize either bio-inspired engineering, direct integration of microorganisms, or both [204]. Given this broad directive, the field covers sensing, actuation, and control problems. Bacteria and other microorganisms have evolved various solutions to the control [32], sensing [28], and actuation [158] problems that arise in microscale fluid environments. Therefore, robust interfaces for the flow of information between electronics and bacteria for control and access to these systems would be invaluable.

Although a fully untethered, autonomous microbiorobot is at least several decades from materializing, there is a compelling natural existence proof found inside a termite gut, an environment known as a crucible for microbial biodiversity. *Mixotricha paradoxa* is a protist that lives inside the gut of the Australian termite *Mastotermes darwiniensis*. Measuring at roughly half a millimeter in length, this protist has a unique motility strategy: symbiotic flagellated bacteria propel it while it uses its own flagellum as a rudder to steer [205]–[207].

The fact that a team of bacterial beasts of burden can move a millimeter-scale structure makes an autonomous, bacteria-driven robot possible. A silicon chip is typically 0.5 mm thick and could be 1 mm on a side for a form factor comparable to *M. paradoxa*. Such a chip could be powered by an energy scavenging system to provide on-board computation and control to the microbiorobot, while a team of attached bacteria propel it through its environment. Electronic bacterial interfaces of the sort developed in this dissertation could be integrated into such a system to provide biosensing capabilities.

Of course, these optimistic scenarios assume that several problems impeding biohybrid sensor adoption are resolved. First among these is sensor lifetime. All biologically-derived material has a finite shelf life. Biofunctionalized surfaces foul over time and become unusable, proteins degrade, and cells die. If cell-based biosensing is to have a place in the real world, development must shift towards self-sustaining structures. The MCBF presented in Chapter 2 is an example of a structure that will persist for at least several days, provided that there is a carbon source to sustain the bacteria [56]. Microbial fuel cells can be deployed for months if they are well-adapted to their environment [208]. Sensor encapsulation is also required for a complete, marketable device. A biohybrid device should not contaminate the environment it is introduced into, nor should the environment destroy its function. One encapsulation approach is to use a nanoporous membrane filter, such as the silica coating employed by BESSY [42]. Another option is to develop biohybrid structures that utilize bacteria native to the environment in which they are to be deployed.

Needless to say, a great deal of work is required to realize these imagined vignettes from our biohybrid future. With the techniques introduced here, we look forward to just a small sliver of what's possible when bacteria are interfaced with electronics.

Bibliography

[1] M. B. Miller and B. L. Bassler, "Quorum sensing in bacteria," *Annual Reviews in Microbiology*, vol. 55, no. 1, pp. 165–199, 2001.

[2] C. M. Waters and B. L. Bassler, "Quorum sensing: cell-to-cell communication in bacteria," *Annu. Rev. Cell Dev. Biol.*, vol. 21, pp. 319–346, 2005.

[3] J. Macía, F. Posas, and R. V. Solé, "Distributed computation: the new wave of synthetic biology devices," *Trends in biotechnology*, vol. 30, no. 6, pp. 342–349, 2012.

[4] J. C. Anderson, C. A. Voigt, and A. P. Arkin, "Environmental signal integration by a modular AND gate," *Molecular systems biology*, vol. 3, no. 1, p. 133, 2007.

[5] A. A. Green, J. Kim, D. Ma, P. A. Silver, J. J. Collins, and P. Yin, "Complex cellular logic computation using ribocomputing devices," *Nature*, vol. 548, no. 7665, p. 117, 2017.

[6] R. M. Shih, D. S. Contreras, T. L. Massey, J. T. Greenspun, and K. S. Pister, "Characterization of electrostatic gap-closing actuator arrays in aqueous conditions," in *Micro Electro Mechanical Systems (MEMS), 2018 IEEE*, IEEE, 2018, pp. 596–599.

[7] D. S. Contreras, D. S. Drew, and K. S. Pister, "First steps of a millimeter-scale walking silicon robot," in *Solid-State Sensors, Actuators and Microsystems (TRANSDUCERS), 2017 19th International Conference on*, IEEE, 2017, pp. 910–913.

[8] J. T. CGreenspun and K. S. Pister, "First Leaps of an Electrostatic Inchworm Motor-Driven Jumping Microrobot," in *Micro Electro Mechanical Systems (MEMS), 2018 IEEE*, IEEE, 2018.

[9] H. C. Berg, "The rotary motor of bacterial flagella," *Ann. Rev. of Biochemistry*, vol. 72, no. 1, pp. 19–54, 2003.

[10] R. Daniel, J. R. Rubens, R. Sarpeshkar, and T. K. Lu, "Synthetic analog computation in living cells," *Nature*, vol. 497, no. 7451, p. 619, 2013.

[11] D. R. Thévenot, K. Toth, R. A. Durst, and G. S. Wilson, "Electrochemical biosensors: recommended definitions and classification," *Biosensors and Bioelectronics*, vol. 16, no. 1, pp. 121–131, 2001.

[12] K. Cammann, "Bio-sensors based on ion-selective electrodes," *Fresenius' Journal of Analytical Chemistry*, vol. 287, no. 1, pp. 1–9, 1977.

[13] W. R. Heineman and W. B. Jensen, "Leland C. Clark Jr.(1918–2005)," *Biosensors and Bioelectronics*, vol. 21, no. 8, pp. 1403–1404, 2006.

[14] C. M. Wong, K. H. Wong, and X. D. Chen, "Glucose oxidase: natural occurrence, function, properties and industrial applications," *Applied microbiology and biotechnology*, vol. 78, no. 6, pp. 927–938, 2008.

[15] W. J. Blaedel and C. L. Olson, *Amperometric determination of glucose*, US Patent 3,367,849, 1968.

[16] J. Arlett, E. Myers, and M. Roukes, "Comparative advantages of mechanical biosensors," *Nature nanotechnology*, vol. 6, no. 4, pp. 203–215, 2011.

[17] J. Tamayo, P. M. Kosaka, J. J. Ruz, Á. San Paulo, and M. Calleja, "Biosensors based on nanomechanical systems," *Chemical Society Reviews*, vol. 42, no. 3, pp. 1287–1311, 2013.

[18] J Llandro, J. Palfreyman, A Ionescu, and C. H. Barnes, "Magnetic biosensor technologies for medical applications: a review," *Medical and Biological Engineering and Computing*, vol. 48, no. 10, pp. 977–998, 2010.

[19] J. B. Haun, T.-J. Yoon, H. Lee, and R. Weissleder, "Magnetic nanoparticle biosensors," *Wiley Interdisciplinary Reviews: Nanomedicine and Nanobiotechnology*, vol. 2, no. 3, pp. 291–304, 2010.

[20] L. Su, W. Jia, C. Hou, and Y. Lei, "Microbial biosensors: a review," *Biosensors and Bioelectronics*, vol. 26, no. 5, pp. 1788–1799, 2011.

[21] M. A. TerAvest and C. M. Ajo-Franklin, "Transforming exoelectrogens for biotechnology using synthetic biology," *Biotechnology and bioengineering*, vol. 113, no. 4, pp. 687–697, 2016.

[22] A. Leung, P. M. Shankar, and R. Mutharasan, "A review of fiber-optic biosensors," *Sensors and Actuators B: Chemical*, vol. 125, no. 2, pp. 688–703, 2007.

[23] A. S. Khalil and J. J. Collins, "Synthetic biology: applications come of age," *Nature Reviews Genetics*, vol. 11, no. 5, pp. 367–379, 2010.

[24] Y. Shao, J. Wang, H. Wu, J. Liu, I. A. Aksay, and Y. Lin, "Graphene based electrochemical sensors and biosensors: a review," *Electroanalysis*, vol. 22, no. 10, pp. 1027–1036, 2010.

[25] J. Wang, "Carbon-nanotube based electrochemical biosensors: A review," *Electroanalysis*, vol. 17, no. 1, pp. 7–14, 2005.

[26] J. Wang, G Rivas, X. Cai, E. Palecek, P Nielsen, H. Shiraishi, N Dontha, D Luo, C Parrado, M Chicharro, *et al.*, "DNA electrochemical biosensors for environmental monitoring. A review," *Analytica Chimica Acta*, vol. 347, no. 1-2, pp. 1–8, 1997.

[27] C. Chen, Q. Xie, D. Yang, H. Xiao, Y. Fu, Y. Tan, and S. Yao, "Recent advances in electrochemical glucose biosensors: a review," *RSC Advances*, vol. 3, no. 14, pp. 4473–4491, 2013.

[28] H. C. Berg and E. M. Purcell, "Physics of chemoreception," *Biophysical Journal*, vol. 20, no. 2, pp. 193–219, 1977.

[29] H. Mao, P. S. Cremer, and M. D. Manson, "A sensitive, versatile microfluidic assay for bacterial chemotaxis," *Proc. Natl. Acad. Sci.*, vol. 100, no. 9, pp. 5449–5454, 2003.

[30] C. E. Outten and T. V. O'halloran, "Femtomolar sensitivity of metalloregulatory proteins controlling zinc homeostasis," *Science*, vol. 292, no. 5526, pp. 2488–2492, 2001.

[31] Y. Ma, C. Zhu, P. Ma, and K. Yu, "Studies on the diffusion coefficients of amino acids in aqueous solutions," *Journal of Chemical & Engineering Data*, vol. 50, no. 4, pp. 1192–1196, 2005.

[32] H. C. Berg, D. A. Brown, *et al.*, "Chemotaxis in *Escherichia coli* analysed by three-dimensional tracking," *Nature*, vol. 239, no. 5374, pp. 500–504, 1972.

[33] M. Shamir, Y. Bar-On, R. Phillips, and R. Milo, "Snapshot: timescales in cell biology," *Cell*, vol. 164, no. 6, pp. 1302–1302, 2016.

[34] D. M. Miller, J. Olson, J. Pflugrath, and F. Quiocho, "Rates of ligand binding to periplasmic proteins involved in bacterial transport and chemotaxis.," *Journal of Biological Chemistry*, vol. 258, no. 22, pp. 13 665–13 672, 1983.

[35] D. Wang and C. A. Fierke, "The BaeSR regulon is involved in defense against zinc toxicity in *E. coli*," *Metallomics*, vol. 5, no. 4, pp. 372–383, 2013.

[36] T. Sagawa, Y. Kikuchi, Y. Inoue, H. Takahashi, T. Muraoka, K. Kinbara, A. Ishijima, and H. Fukuoka, "Single-cell *E. coli* response to an instantaneously applied chemotactic signal," *Biophysical Journal*, vol. 107, no. 3, pp. 730–739, 2014.

[37] H. Wang and Z. J. Ren, "A comprehensive review of microbial electrochemical systems as a platform technology," *Biotechnology advances*, vol. 31, no. 8, pp. 1796–1807, 2013.

[38] D. Coursolle and J. A. Gralnick, "Reconstruction of extracellular respiratory pathways for iron (III) reduction in *Shewanella oneidensis* strain MR-1," *Frontiers in microbiology*, vol. 3, p. 56, 2012.

[39] O. Bretschger, A. Obraztsova, C. A. Sturm, I. S. Chang, Y. A. Gorby, S. B. Reed, D. E. Culley, C. L. Reardon, S. Barua, M. F. Romine, *et al.*, "Current production and metal oxide reduction by *Shewanella oneidensis* MR-1 wild type and mutants," *Applied and environmental microbiology*, vol. 73, no. 21, pp. 7003–7012, 2007.

[40] D. Coursolle, D. B. Baron, D. R. Bond, and J. A. Gralnick, "The Mtr respiratory pathway is essential for reducing flavins and electrodes in *Shewanella oneidensis*," *Journal of bacteriology*, vol. 192, no. 2, pp. 467–474, 2010.

[41] M. A. TerAvest, T. J. Zajdel, and C. M. Ajo-Franklin, "The Mtr pathway of *Shewanella oneidensis* MR-1 couples substrate utilization to current production in *Escherichia coli*," *ChemElectroChem*, vol. 1, no. 11, pp. 1874–1879, 2014.

[42] A. Y. Zhou, M. Baruch, C. M. Ajo-Franklin, and M. M. Maharbiz, "A portable bioelectronic sensing system (BESSY) for environmental deployment incorporating differential microbial sensing in miniaturized reactors," *PloS one*, vol. 12, no. 9, e0184994, 2017.

[43] K. Belousov, I. Denisov, K. Lukyanenko, A. Yakimov, A. Bukatin, I. Kukhtevich, V. Sorokin, E. Esimbekova, P. Belobrov, and A. Evstrapov, "Dissolution and mixing of flavin mononucleotide in microfluidic chips for bioassay," in *Journal of Physics: Conference Series*, IOP Publishing, vol. 741, 2016, p. 012 058.

[44] J. E. B. Randles, "Kinetics of rapid electrode reactions," *Discussions of the faraday society*, vol. 1, pp. 11–19, 1947.

[45] N. Sekar and R. P. Ramasamy, "Electrochemical impedance spectroscopy for microbial fuel cell characterization," *J Microb Biochem Technol S*, vol. 6, no. 2, 2013.

[46] A. J. Bard, L. R. Faulkner, J. Leddy, and C. G. Zoski, *Electrochemical methods: fundamentals and applications*. wiley New York, 1980, vol. 2.

[47] G. Brug, A. Van Den Eeden, M Sluyters-Rehbach, and J. Sluyters, "The analysis of electrode impedances complicated by the presence of a constant phase element," *Journal of electroanalytical chemistry and interfacial electrochemistry*, vol. 176, no. 1-2, pp. 275–295, 1984.

[48] J. Li, P. S. Sheeran, and C. Kleinstreuer, "Analysis of multi-layer immiscible fluid flow in a microchannel," *Journal of Fluids Engineering*, vol. 133, no. 11, p. 111 202, 2011.

[49] B. J. Kirby, *Micro-and nanoscale fluid mechanics: transport in microfluidic devices*. Cambridge university press, 2010.

[50] P. B. Ishai, M. S. Talary, A. Caduff, E. Levy, and Y. Feldman, "Electrode polarization in dielectric measurements: a review," *Measurement Science and Technology*, vol. 24, no. 10, p. 102 001, 2013.

[51] P. Linderholm, T. Braschler, J. Vannod, Y. Barrandon, M. Brouard, and P. Renaud, "Two-dimensional impedance imaging of cell migration and epithelial stratification," *Lab on a Chip*, vol. 6, no. 9, pp. 1155–1162, 2006.

[52] T. A. Driscoll and L. N. Trefethen, *Schwarz-christoffel mapping*. Cambridge University Press, 2002, vol. 8.

[53] C. H. Hamann, A Hamnett, and W Vielstich, *Electrochemistry, Second Completely Revised and Updated Edition*, 2007.

[54] S. M. Radke and E. C. Alocilja, "A high density microelectrode array biosensor for detection of *E. coli* O157: H7," *Biosensors and Bioelectronics*, vol. 20, no. 8, pp. 1662–1667, 2005.

[55] S. Gawad, L. Schild, and P. Renaud, "Micromachined impedance spectroscopy flow cytometer for cell analysis and particle sizing," *Lab on a Chip*, vol. 1, no. 1, pp. 76–82, 2001.

[56] T. J. Zajdel, M. Baruch, G. Méhes, E. Stavrinidou, M. Berggren, M. M. Maharbiz, D. T. Simon, and C. M. Ajo-Franklin, "PEDOT:PSS-based Multilayer Bacterial-Composite Films for Bioelectronics," submitted.

[57] F. Golitsch, C. Bücking, and J. Gescher, "Proof of principle for an engineered microbial biosensor based on *Shewanella oneidensis* outer membrane protein complexes," *Biosensors and Bioelectronics*, vol. 47, pp. 285–291, 2013.

[58] D. P. Webster, M. A. TerAvest, D. F. Doud, A. Chakravorty, E. C. Holmes, C. M. Radens, S. Sureka, J. A. Gralnick, and L. T. Angenent, "An arsenic-specific biosensor with genetically engineered *Shewanella oneidensis* in a bioelectrochemical system," *Biosensors and Bioelectronics*, vol. 62, pp. 320–324, 2014.

[59] H. M. Jensen, A. E. Albers, K. R. Malley, Y. Y. Londer, B. E. Cohen, B. A. Helms, P. Weigele, J. T. Groves, and C. M. Ajo-Franklin, "Engineering of a synthetic electron conduit in living cells," *Proceedings of the National Academy of Sciences*, vol. 107, no. 45, pp. 19 213–19 218, 2010.

[60] E. Kipf, J. Koch, B. Geiger, J. Erben, K. Richter, J. Gescher, R. Zengerle, and S. Kerzenmacher, "Systematic screening of carbon-based anode materials for microbial fuel cells with *Shewanella oneidensis* MR-1," *Bioresource technology*, vol. 146, pp. 386–392, 2013.

[61] K. P. Nevin, H Richter, S. Covalla, J. Johnson, T. Woodard, A. Orloff, H Jia, M Zhang, and D. Lovley, "Power output and columbic efficiencies from biofilms of *Geobacter sulfurreducens* comparable to mixed community microbial fuel cells," *Environmental microbiology*, vol. 10, no. 10, pp. 2505–2514, 2008.

[62] L. Peng, S.-J. You, and J.-Y. Wang, "Carbon nanotubes as electrode modifier promoting direct electron transfer from *Shewanella oneidensis*," *Biosensors and Bioelectronics*, vol. 25, no. 5, pp. 1248–1251, 2010.

[63] M. Chen, X. Zhou, X. Liu, R. J. Zeng, F. Zhang, J. Ye, and S. Zhou, "Facilitated extracellular electron transfer of *Geobacter sulfurreducens* biofilm with in situ formed gold nanoparticles," *Biosensors and Bioelectronics*, vol. 108, pp. 20–26, 2018.

[64] C. Zhao, P. Gai, R. Song, J. Zhang, and J.-J. Zhu, "Graphene/Au composites as an anode modifier for improving electricity generation in *Shewanella*-inoculated microbial fuel cells," *Analytical Methods*, vol. 7, no. 11, pp. 4640–4644, 2015.

[65] Y Hindatu, M. Annuar, and A. Gumel, "Mini-review: Anode modification for improved performance of microbial fuel cell," *Renewable and Sustainable Energy Reviews*, vol. 73, pp. 236–248, 2017.

[66] R. Karthikeyan, N. Krishnaraj, A. Selvam, J. W.-C. Wong, P. K. Lee, M. K. Leung, and S. Berchmans, "Effect of composites based nickel foam anode in microbial fuel cell using *Acetobacter aceti* and *Gluconobacter roseus* as a biocatalysts," *Bioresource technology*, vol. 217, pp. 113–120, 2016.

[67] Y. Tao, Q. Liu, J. Chen, B. Wang, Y. Wang, K. Liu, M. Li, H. Jiang, Z. Lu, and D. Wang, "Hierarchically three-dimensional nanofiber based textile with high conductivity and biocompatibility as a microbial fuel cell anode," *Environmental science & technology*, vol. 50, no. 14, pp. 7889–7895, 2016.

[68] R.-B. Song, Y. Wu, Z.-Q. Lin, J. Xie, C. H. Tan, J. S. C. Loo, B. Cao, J.-R. Zhang, J.-J. Zhu, and Q. Zhang, "Rücktitelbild: Living and conducting: Coating individual bacterial cells with in situ formed polypyrrole," *Angewandte Chemie*, vol. 129, no. 35, pp. 10 744–10 744, 2017.

[69] C. Feng, L. Ma, F. Li, H. Mai, X. Lang, and S. Fan, "A polypyrrole/anthraquinone-2, 6-disulphonic disodium salt (PPy/AQDS)-modified anode to improve performance of microbial fuel cells," *Biosensors and Bioelectronics*, vol. 25, no. 6, pp. 1516–1520, 2010.

[70] K. A. Ludwig, J. D. Uram, J. Yang, D. C. Martin, and D. R. Kipke, "Chronic neural recordings using silicon microelectrode arrays electrochemically deposited with a poly (3, 4-ethylenedioxythiophene)(PEDOT) film," *Journal of neural engineering*, vol. 3, no. 1, p. 59, 2006.

[71] K. M. Persson, R. Karlsson, K. Svennersten, S. Löffler, E. W. Jager, A. Richter-Dahlfors, P. Konradsson, and M. Berggren, "Electronic Control of Cell Detachment Using a Self-Doped Conducting Polymer," *Advanced Materials*, vol. 23, no. 38, pp. 4403–4408, 2011.

[72] E. Stavrinidou, R. Gabrielsson, E. Gomez, X. Crispin, O. Nilsson, D. T. Simon, and M. Berggren, "Electronic plants," *Science advances*, vol. 1, no. 10, e1501136, 2015.

[73] X. Strakosas, M. Bongo, and R. M. Owens, "The organic electrochemical transistor for biological applications," *Journal of Applied Polymer Science*, vol. 132, no. 15, 2015.

[74] J. Yang, D. H. Kim, J. L. Hendricks, M. Leach, R. Northey, and D. C. Martin, "Ordered surfactant-templated poly (3, 4-ethylenedioxythiophene)(PEDOT) conducting polymer on microfabricated neural probes," *Acta Biomaterialia*, vol. 1, no. 1, pp. 125–136, 2005.

[75] J. J. Guzman, M. O. P. Kara, M. W. Frey, and L. T. Angenent, "Performance of electro-spun carbon nanofiber electrodes with conductive poly (3, 4-ethylenedioxythiophene) coatings in bioelectrochemical systems," *Journal of Power Sources*, vol. 356, pp. 331–337, 2017.

[76] H. Jiang, L. J. Halverson, and L. Dong, "A miniature microbial fuel cell with conducting nanofibers-based 3D porous biofilm," *Journal of Micromechanics and Microengineering*, vol. 25, no. 12, p. 125 017, 2015.

[77] Y. L. Kang, S. Ibrahim, and S. Pichiah, "Synergetic effect of conductive polymer poly (3, 4-ethylenedioxythiophene) with different structural configuration of anode for microbial fuel cell application," *Bioresource technology*, vol. 189, pp. 364–369, 2015.

[78] D. Q. Le, S. Tokonami, T. Nishino, H. Shiigi, and T. Nagaoka, "Electrochemical evaluation of poly (3, 4-ethylenedioxythiophene) films doped with bacteria based on viability analysis," *Bioelectrochemistry*, vol. 105, pp. 50–55, 2015.

[79] C. R. Myers and K. H. Nealson, "Bacterial manganese reduction and growth with manganese oxide as the sole electron acceptor," *Science*, vol. 240, no. 4857, pp. 1319–1321, 1988.

[80] N. J. Kotloski and J. A. Gralnick, "Flavin electron shuttles dominate extracellular electron transfer by *Shewanella oneidensis*," *MBio*, vol. 4, no. 1, e00553–12, 2013.

[81] J. Roncali, "Conjugated poly (thiophenes): synthesis, functionalization, and applications," *Chemical Reviews*, vol. 92, no. 4, pp. 711–738, 1992.

[82] H. R. Byon, S. W. Lee, S. Chen, P. T. Hammond, and Y. Shao-Horn, "Thin films of carbon nanotubes and chemically reduced graphenes for electrochemical micro-capacitors," *Carbon*, vol. 49, no. 2, pp. 457–467, 2011.

[83] W. Pell, B. Conway, and N Marincic, "Analysis of non-uniform charge/discharge and rate effects in porous carbon capacitors containing sub-optimal electrolyte concentrations," *Journal of electroanalytical chemistry*, vol. 491, no. 1-2, pp. 9–21, 2000.

[84] H. Wang and L. Pilon, "Physical interpretation of cyclic voltammetry for measuring electric double layer capacitances," *Electrochimica Acta*, vol. 64, pp. 130–139, 2012.

[85] J. Yan, T. Wei, B. Shao, F. Ma, Z. Fan, M. Zhang, C. Zheng, Y. Shang, W. Qian, and F. Wei, "Electrochemical properties of graphene nanosheet/carbon black composites as electrodes for supercapacitors," *Carbon*, vol. 48, no. 6, pp. 1731–1737, 2010.

[86] C. M. Proctor, J. Rivnay, and G. G. Malliaras, "Understanding volumetric capacitance in conducting polymers," *Journal of Polymer Science Part B: Polymer Physics*, vol. 54, no. 15, pp. 1433–1436, 2016.

[87] K. Tybrandt, I. V. Zozoulenko, and M. Berggren, "Chemical potential–electric double layer coupling in conjugated polymer–polyelectrolyte blends," *Science advances*, vol. 3, no. 12, eaao3659, 2017.

[88] A. Malti, J. Edberg, H. Granberg, Z. U. Khan, J. W. Andreasen, X. Liu, D. Zhao, H. Zhang, Y. Yao, J. W. Brill, *et al.*, "An organic mixed ion–electron conductor for power electronics," *Advanced science*, vol. 3, no. 2, 2016.

[89] A. Okamoto, R. Nakamura, K. H. Nealson, and K. Hashimoto, "Bound Flavin Model Suggests Similar Electron-Transfer Mechanisms in *Shewanella* and *Geobacter*," *ChemElectroChem*, vol. 1, no. 11, pp. 1808–1812, 2014.

[90] T. Arbring Sjöström, M. Berggren, E. O. Gabrielsson, P. Janson, D. J. Poxson, M. Seitanidou, and D. T. Simon, "A Decade of Iontronic Delivery Devices," *Advanced Materials Technologies*, p. 1 700 360,

[91] *Clevios PH100 datasheet*, Heraeus Group, 2010.

[92] E. Marsili, D. B. Baron, I. D. Shikhare, D. Coursolle, J. A. Gralnick, and D. R. Bond, "*Shewanella* secretes flavins that mediate extracellular electron transfer," *Proceedings of the National Academy of Sciences*, vol. 105, no. 10, pp. 3968–3973, 2008.

[93] A. Zhou, "A miniaturized bioelectronic sensing system featuring portable microbial reactors for environmental deployment," 2017.

[94] T. J. Zajdel, M. A. TerAvest, B. Rad, C. M. Ajo-Franklin, and M. M. Maharbiz, "Probing the dynamics of the proton-motive force in *E. coli*," in *Proc. of IEEE SENSORS*, 2014, pp. 1764–1767.

[95] T. J. Zajdel, A. Nam, J. Yuan, V. R. Shirsat, B. Rad, and M. M. Maharbiz, "Applying machine learning to the flagellar motor for biosensing," in *Engineering in Medicine and Biology Society (EMBC), 2018 40th Annual International Conference of the IEEE*, IEEE, 2018.

[96] V. Sourjik and N. S. Wingreen, "Responding to chemical gradients: bacterial chemotaxis," *Curr. Opinion in Cell Biology*, vol. 24, no. 2, pp. 262–268, 2012.

[97] J. P. Armitage, "Three hundred years of bacterial motility," *Foundations of Modern Biochemistry*, vol. 3, pp. 107–171, 1997.

[98] Y. Sowa and R. M. Berry, "Bacterial flagellar motor," *Quarterly reviews of biophysics*, vol. 41, no. 2, pp. 103–132, 2008.

[99] H. C. Berg, "Bacterial flagellar motor," *Current Biology*, vol. 18, no. 16, R689–R691, 2008.

[100] J. A. Nirody, Y.-R. Sun, and C.-J. Lo, "The biophysicistś guide to the bacterial flagellar motor," *Advances in Physics: X*, vol. 2, no. 2, pp. 324–343, 2017.

[101] F. W. Dahlquist, "The Bacterial Flagellar Motor Continues to Amaze," *Biophysical journal*, vol. 114, no. 3, pp. 505–506, 2018.

[102] H. C. Berg, E. coli *in Motion*. Springer Science & Business Media, 2008.

[103] K. K. Mandadapu, J. A. Nirody, R. M. Berry, and G. Oster, "Mechanics of torque generation in the bacterial flagellar motor," *Proceedings of the National Academy of Sciences*, vol. 112, no. 32, E4381–E4389, 2015.

[104] C. V. Gabel and H. C. Berg, "The speed of the flagellar rotary motor of *Escherichia coli* varies linearly with protonmotive force," *Proceedings of the National Academy of Sciences*, vol. 100, no. 15, pp. 8748–8751, 2003.

[105] S. W. Reid, M. C. Leake, J. H. Chandler, C.-J. Lo, J. P. Armitage, and R. M. Berry, "The maximum number of torque-generating units in the flagellar motor of *Escherichia coli* is at least 11," *Proceedings of the National Academy of Sciences*, vol. 103, no. 21, pp. 8066–8071, 2006.

[106] L. Turner, W. S. Ryu, and H. C. Berg, "Real-time imaging of fluorescent flagellar filaments," *Journal of bacteriology*, vol. 182, no. 10, pp. 2793–2801, 2000.

[107] P. J. Mears, S. Koirala, C. V. Rao, I. Golding, and Y. R. Chemla, "*Escherichia coli* swimming is robust against variations in flagellar number," *Elife*, vol. 3, 2014.

[108] S. M. Block, J. E. Segall, and H. C. Berg, "Impulse responses in bacterial chemotaxis," *Cell*, vol. 31, no. 1, pp. 215–226, 1982.

[109] T. W. Grebe and J. Stock, "Bacterial chemotaxis: the five sensors of a bacterium," *Current Biology*, vol. 8, no. 5, R154–R157, 1998.

[110] J. Parkinson, "Signal amplification in bacterial chemotaxis through receptor teamwork," *ASM News*, vol. 70, no. 12, pp. 575–582, 2004.

[111] S. R. Lybarger and J. R. Maddock, "Clustering of the Chemoreceptor Complex in *Escherichia coli* Is Independent of the Methyltransferase CheR and the Methylesterase CheB," *Journal of bacteriology*, vol. 181, no. 17, pp. 5527–5529, 1999.

[112] V. Sourjik, "Receptor clustering and signal processing in *E. coli* chemotaxis," *Trends in microbiology*, vol. 12, no. 12, pp. 569–576, 2004.

[113] D. Greenfield, A. L. McEvoy, H. Shroff, G. E. Crooks, N. S. Wingreen, E. Betzig, and J. Liphardt, "Self-organization of the *Escherichia coli* chemotaxis network imaged with super-resolution light microscopy," *PLoS biology*, vol. 7, no. 6, e1000137, 2009.

[114] T. Duke and D. Bray, "Heightened sensitivity of a lattice of membrane receptors," *Proceedings of the National Academy of Sciences*, vol. 96, no. 18, pp. 10 104–10 108, 1999.

[115] V. Sourjik and H. C. Berg, "Receptor sensitivity in bacterial chemotaxis," *Proceedings of the National Academy of Sciences*, vol. 99, no. 1, pp. 123–127, 2002.

[116] V. Sourjik and H. C. Berg, "Functional interactions between receptors in bacterial chemotaxis," *Nature*, vol. 428, no. 6981, p. 437, 2004.

[117] S.-H. Kim, W. Wang, and K. K. Kim, "Dynamic and clustering model of bacterial chemotaxis receptors: structural basis for signaling and high sensitivity," *Proceedings of the National Academy of Sciences*, vol. 99, no. 18, pp. 11 611–11 615, 2002.

[118] J. E. Gestwicki and L. L. Kiessling, "Inter-receptor communication through arrays of bacterial chemoreceptors," *Nature*, vol. 415, no. 6867, p. 81, 2002.

[119] G. L. Hazelbauer, C. Park, and D. M. Nowlin, "Adaptational "crosstalk" and the crucial role of methylation in chemotactic migration by *Escherichia coli*," *Proceedings of the National Academy of Sciences*, vol. 86, no. 5, pp. 1448–1452, 1989.

[120] R. G. Endres, O. Oleksiuk, C. H. Hansen, Y. Meir, V. Sourjik, and N. S. Wingreen, "Variable sizes of *Escherichia coli* chemoreceptor signaling teams," *Molecular systems biology*, vol. 4, no. 1, p. 211, 2008.

[121] J. S. Parkinson and S. E. Houts, "Isolation and behavior of *Escherichia coli* deletion mutants lacking chemotaxis functions.," *Journal of bacteriology*, vol. 151, no. 1, pp. 106–113, 1982.

[122] S Clarke and D. Koshland, "Membrane receptors for aspartate and serine in bacterial chemotaxis.," *Journal of Biological Chemistry*, vol. 254, no. 19, pp. 9695–9702, 1979.

[123] C. Wolff and J. S. Parkinson, "Aspartate taxis mutants of the *Escherichia coli* tar chemoreceptor.," *Journal of bacteriology*, vol. 170, no. 10, pp. 4509–4515, 1988.

[124] Y. Yang, A. M Pollard, C. Höfler, G. Poschet, M. Wirtz, R. Hell, and V. Sourjik, "Relation between chemotaxis and consumption of amino acids in bacteria," *Molecular microbiology*, vol. 96, no. 6, pp. 1272–1282, 2015.

[125] M. Hedblom and J Adler, "Genetic and biochemical properties of *Escherichia coli* mutants with defects in serine chemotaxis.," *Journal of bacteriology*, vol. 144, no. 3, pp. 1048–1060, 1980.

[126] M. D. Manson, V. Blank, G. Brade, and C. F. Higgins, "Peptide chemotaxis in *E. coli* involves the Tap signal transducer and the dipeptide permease," *Nature*, vol. 321, no. 6067, pp. 253–256, 1986.

[127] X. Liu and R. E. Parales, "Chemotaxis of *Escherichia coli* to pyrimidines: a new role for the signal transducer tap," *Journal of bacteriology*, vol. 190, no. 3, pp. 972–979, 2008.

[128] H. Kondoh, C. B. Ball, and J. Adler, "Identification of a methyl-accepting chemotaxis protein for the ribose and galactose chemoreceptors of *Escherichia coli*," *Proceedings of the National Academy of Sciences*, vol. 76, no. 1, pp. 260–264, 1979.

[129] B. L. Taylor, I. B. Zhulin, and M. S. Johnson, "Aerotaxis and other energy-sensing behavior in bacteria," *Annual Reviews in Microbiology*, vol. 53, no. 1, pp. 103–128, 1999.

[130] K. J. Watts, M. S. Johnson, and B. L. Taylor, "Minimal requirements for oxygen sensing by the aerotaxis receptor Aer," *Molecular microbiology*, vol. 59, no. 4, pp. 1317–1326, 2006.

[131] S. Bi, A. M. Pollard, Y. Yang, F. Jin, and V. Sourjik, "Engineering Hybrid Chemotaxis Receptors in Bacteria," *ACS synthetic biology*, vol. 5, no. 9, pp. 989–1001, 2016.

[132] G. H. Wadhams and J. P. Armitage, "Making sense of it all: bacterial chemotaxis," *Nature Reviews Molecular Cell Biology*, vol. 5, no. 12, p. 1024, 2004.

[133] N. Vladimirov and V. Sourjik, "Chemotaxis: how bacteria use memory," *Biological chemistry*, vol. 390, no. 11, pp. 1097–1104, 2009.

[134] M. Y. Galperin, "A census of membrane-bound and intracellular signal transduction proteins in bacteria: bacterial IQ, extroverts and introverts," *BMC microbiology*, vol. 5, no. 1, p. 35, 2005.

[135] J. Armitano, C. Baraquet, V. Michotey, V. Méjean, and C. Jourlin-Castelli, "The chemical-in-μwell: a high-throughput technique for identifying solutes eliciting a chemotactic response in motile bacteria," *Research in microbiology*, vol. 162, no. 9, pp. 934–938, 2011.

[136] A. Briegel, D. R. Ortega, P. Mann, A. Kjær, S. Ringgaard, and G. J. Jensen, "Chemotaxis cluster 1 proteins form cytoplasmic arrays in *Vibrio cholerae* and are stabilized by a double signaling domain receptor DosM," *Proceedings of the National Academy of Sciences*, vol. 113, no. 37, pp. 10 412–10 417, 2016.

[137] P. Cluzel, M. Surette, and S. Leibler, "An ultrasensitive bacterial motor revealed by monitoring signaling proteins in single cells," *Science*, vol. 287, no. 5458, pp. 1652–1655, 2000.

[138] U. Alon, M. G. Surette, N. Barkai, and S. Leibler, "Robustness in bacterial chemotaxis," *Nature*, vol. 397, no. 6715, p. 168, 1999.

[139] F. M. Harold, "Energy transduction by ion currents.," Escherichia coli *and* Salmonella*: cellular and molecular biology*, vol. 1, pp. 283–306, 1996.

[140] D. White *et al.*, *Physiology and biochemistry of prokaryotes*. Oxford University Press, 2000.

[141] E. R. Kashket, "The proton motive force in bacteria: a critical assessment of methods," *Annual reviews in microbiology*, vol. 39, no. 1, pp. 219–242, 1985.

[142] J. M. Walter, D. Greenfield, C. Bustamante, and J. Liphardt, "Light-powering *Escherichia coli* with proteorhodopsin," *Proceedings of the National Academy of Sciences*, vol. 104, no. 7, pp. 2408–2412, 2007.

[143] J. M. Kralj, D. R. Hochbaum, A. D. Douglass, and A. E. Cohen, "Electrical spiking in *Escherichia coli* probed with a fluorescent voltage-indicating protein," *Science*, vol. 333, no. 6040, pp. 345–348, 2011.

[144] P. D. Hockings and P. J. Rogers, "The measurement of transmembrane electrical potential with lipophilic cations," *Biochimica et Biophysica Acta (BBA)-Biomembranes*, vol. 1282, no. 1, pp. 101–106, 1996.

[145] D. Novo, N. G. Perlmutter, R. H. Hunt, and H. M. Shapiro, "Accurate flow cytometric membrane potential measurement in bacteria using diethyloxacarbocyanine and a ratiometric technique," *Cytometry Part A*, vol. 35, no. 1, pp. 55–63, 1999.

[146] J.-B. Masson, G. Voisinne, J. Wong-Ng, A. Celani, and M. Vergassola, "Noninvasive inference of the molecular chemotactic response using bacterial trajectories," *PNAS*, vol. 109, no. 5, pp. 1802–1807, 2012.

[147] D. Clausznitzer, G. Micali, S. Neumann, V. Sourjik, and R. G. Endres, "Predicting chemical environments of bacteria from receptor signaling," *PLoS Comput. Biol.*, vol. 10, no. 10, e1003870, 2014.

[148] Y. Inoue, "Rotation Measurements of Tethered Cells," *The Bacterial Flagellum: Methods and Protocols*, pp. 163–174, 2017.

[149] C.-W. Hsu, C.-C. Chang, C.-J. Lin, *et al.*, "A practical guide to support vector classification," 2003.

[150] T. J. Zajdel, A. N. Walczak, D. Sengupta, V. Tieu, B. Rad, and M. M. Maharbiz, "Towards a biohybrid sensing platform built on impedance-based bacterial flagellar motor tachometry," in *2017 IEEE BioCAS*, Oct. 2017, pp. 292–295.

[151] G. Kuwajima, "Construction of a minimum-size functional flagellin of *Escherichia coli.*," *Journal of bacteriology*, vol. 170, no. 7, pp. 3305–3309, 1988.

[152] C. A. Schneider, W. S. Rasband, and K. W. Eliceiri, "NIH Image to ImageJ: 25 years of image analysis," *Nature methods*, vol. 9, no. 7, p. 671, 2012.

[153] T. Ridler, S Calvard, *et al.*, "Picture thresholding using an iterative selection method," *IEEE trans syst Man Cybern*, vol. 8, no. 8, pp. 630–632, 1978.

[154] F. Pedregosa, G. Varoquaux, A. Gramfort, V. Michel, B. Thirion, O. Grisel, M. Blondel, P. Prettenhofer, R. Weiss, V. Dubourg, J. Vanderplas, A. Passos, D. Cournapeau, M. Brucher, M. Perrot, and E. Duchesnay, "Scikit-learn: Machine learning in Python," *Journal of Machine Learning Research*, vol. 12, pp. 2825–2830, 2011.

[155] A. Ben-Hur, C. S. Ong, S. Sonnenburg, B. Schölkopf, and G. Rätsch, "Support vector machines and kernels for computational biology," *PLoS computational biology*, vol. 4, no. 10, e1000173, 2008.

[156] B. A. Mello and Y. Tu, "Quantitative modeling of sensitivity in bacterial chemotaxis: the role of coupling among different chemoreceptor species," *Proceedings of the National Academy of Sciences*, vol. 100, no. 14, pp. 8223–8228, 2003.

[157] C. Dobell *et al.*, "Antony van Leeuwenhoek and his "Little Animals." Being Some Account of the Father of Protozoology and Bacteriology and his Multifarious Discoveries in these Disciplines.," 1932.

[158] E. M. Purcell, "Life at low Reynolds number," *American journal of physics*, vol. 45, no. 1, pp. 3–11, 1977.

[159] G. Drews, "Contributions of Theodor Wilhelm Engelmann on phototaxis, chemotaxis, and photosynthesis," *Photosynthesis research*, vol. 83, no. 1, pp. 25–34, 2005.

[160] J Adler, "Chemotaxis: old and new," *Plant Biology*, vol. 101, no. 2, pp. 93–100, 1988.

[161] J. Adler, "Chemotaxis in bacteria," *Science*, vol. 153, no. 3737, pp. 708–716, 1966.

[162] J. B. Armstrong, J. Adler, and M. M. Dahl, "Nonchemotactic mutants of *Escherichia coli*," *Journal of Bacteriology*, vol. 93, no. 1, pp. 390–398, 1967.

[163] R. M. Macnab and D. Koshland, "The gradient-sensing mechanism in bacterial chemotaxis," *Proceedings of the National Academy of Sciences*, vol. 69, no. 9, pp. 2509–2512, 1972.

[164] H. C. Berg and R. A. Anderson, "Bacteria swim by rotating their flagellar filaments," *Nature*, vol. 245, no. 5425, p. 380, 1973.

[165] M. Silverman and M. Simon, "Flagellar rotation and the mechanism of bacterial motility," *Nature*, vol. 249, pp. 73–74, 1974.

[166] B. E. Scharf, K. A. Fahrner, L. Turner, and H. C. Berg, "Control of direction of flagellar rotation in bacterial chemotaxis," *PNAS*, vol. 95, no. 1, pp. 201–206, 1998.

[167] W. S. Ryu, R. M. Berry, and H. C. Berg, "Torque-generating units of the flagellar motor of *Escherichia coli* have a high duty ratio," *Nature*, vol. 403, no. 6768, pp. 444–447, 2000.

[168] T. Pilizota, T. Bilyard, F. Bai, M. Futai, H. Hosokawa, and R. M. Berry, "A programmable optical angle clamp for rotary molecular motors," *Biophysical journal*, vol. 93, no. 1, pp. 264–275, 2007.

[169] M. T. Brown, B. C. Steel, C. Silvestrin, D. A. Wilkinson, N. J. Delalez, C. N. Lumb, B. Obara, J. P. Armitage, and R. M. Berry, "Flagellar hook flexibility is essential for bundle formation in swimming *Escherichia coli* cells," *J. of Bacteriology*, vol. 194, no. 13, pp. 3495–3501, 2012.

[170] Z. Xiao-Qian, L. Zhe-Yu, X.-Y. Zhang, L. Jiang, R. Nan-Qi, and S. Kai, "Advance in Bacteria Chemotaxis on Microfluidic Devices," *Chinese Journal of Analytical Chemistry*, vol. 45, no. 11, pp. 1734–1744, 2017.

[171] A. Mahdavifar, J. Xu, M. Hovaizi, P. Hesketh, W. Daley, and D. Britton, "A nitrocellulose-based microfluidic device for generation of concentration gradients and study of bacterial chemotaxis," *Journal of The Electrochemical Society*, vol. 161, no. 2, B3064–B3070, 2014.

[172] C. Roggo, C. Picioreanu, X. Richard, C. Mazza, H. Van Lintel, and J. R. van der Meer, "Quantitative chemical biosensing by bacterial chemotaxis in microfluidic chips," *Environmental microbiology*, vol. 20, no. 1, pp. 241–258, 2018.

[173] M. Kojima, Z. Wang, M. Nakajima, T. Arai, and T. Fukuda, "Microchip device with parallel operation for bacterial chemotactic analysis," *Sensors and Actuators B: Chemical*, vol. 245, pp. 695–701, 2017.

[174] J.-W. Kim and S. Tung, "Bio-hybrid micro/nanodevices powered by flagellar motor: challenges and strategies," *Frontiers in bioengineering and biotechnology*, vol. 3, 2015.

[175] T. Kasai and Y. Sowa, "Measurements of the Rotation of the Flagellar Motor by Bead Assay," *The Bacterial Flagellum: Methods and Protocols*, pp. 185–192, 2017.

[176] M. Koch, A. Evans, and A Brunnschweiler, "Design and fabrication of a micromachined Coulter counter," *Journal of micromechanics and microengineering*, vol. 9, no. 2, p. 159, 1999.

[177] M. D. Graham, "The Coulter principle: foundation of an industry," *JALA: Journal of the Association for Laboratory Automation*, vol. 8, no. 6, pp. 72–81, 2003.

[178] H. Morgan, T. Sun, D. Holmes, S. Gawad, and N. G. Green, "Single cell dielectric spectroscopy," *Journal of Physics D: Applied Physics*, vol. 40, no. 1, p. 61, 2006.

[179] S. Gawad, K. Cheung, U. Seger, A. Bertsch, and P. Renaud, "Dielectric spectroscopy in a micromachined flow cytometer: theoretical and practical considerations," *Lab on a Chip*, vol. 4, no. 3, pp. 241–251, 2004.

[180] T. Sun and H. Morgan, "Single-cell microfluidic impedance cytometry: a review," *Microfluidics and Nanofluidics*, vol. 8, no. 4, pp. 423–443, 2010.

[181] T Chen, F Artis, D Dubuc, J.-J. Fournie, M Poupot, and K Grenier, "Microwave biosensor dedicated to the dielectric spectroscopy of a single alive biological cell in its culture medium," in *Microwave Symposium Digest (IMS), 2013 IEEE MTT-S International*, IEEE, 2013, pp. 1–4.

[182] M. R. Kellman, F. R. Rivest, A. Pechacek, L. L. Sohn, and M. Lustig, "Node-Pore Coded Coincidence Correction: Coulter Counters, Code Design, and Sparse Deconvolution," *IEEE Sensors Journal*, vol. 18, no. 8, pp. 3068–3079, 2018.

[183] H. Schwan, "Electrode polarization impedance and measurements in biological materials," *Annals of the New York Academy of Sciences*, vol. 148, no. 1, pp. 191–209, 1968.

[184] R. Rodriguez-Trujillo, O. Castillo-Fernandez, M. Garrido, M. Arundell, A. Valencia, and G. Gomila, "High-speed particle detection in a micro-Coulter counter with two-dimensional adjustable aperture," *Biosensors and Bioelectronics*, vol. 24, no. 2, pp. 290–296, 2008.

[185] P. Linderholm, L. Marescot, M. H. Loke, and P. Renaud, "Cell culture imaging using microimpedance tomography," *IEEE Transactions on Biomedical Engineering*, vol. 55, no. 1, pp. 138–146, 2008.

[186] P. Linderholm and P. Renaud, "Comment on "AC frequency characteristics of coplanar impedance sensors as design parameters" by Jongin Hong, Dae Sung Yoon, Sung Kwan Kim, Tae Song Kim, Sanghyo Kim, Eugene Y. Pak and Kwangsoo No, Lab Chip, 2005, 5, 270," *Lab on a Chip*, vol. 5, no. 12, pp. 1416–1417, 2005.

[187] R. Schinzinger and P. A. Laura, *Conformal mapping: methods and applications*. Courier Corporation, 2003.

[188] X. Cui and D. C. Martin, "Electrochemical deposition and characterization of poly (3, 4-ethylenedioxythiophene) on neural microelectrode arrays," *Sensors and Actuators B: Chemical*, vol. 89, no. 1-2, pp. 92–102, 2003.

[189] V. Castagnola, C. Bayon, E. Descamps, and C. Bergaud, "Morphology and conductivity of PEDOT layers produced by different electrochemical routes," *Synthetic metals*, vol. 189, pp. 7–16, 2014.

[190] S. Shima, H. Matsuoka, T. Iwamoto, and H. Sakai, "Antimicrobial action of ε-poly-L-lysine," *The Journal of antibiotics*, vol. 37, no. 11, pp. 1449–1455, 1984.

[191] D. H. Coombs and N. R. Watts, "Generating sucrose gradients in three minutes by tilted tube rotation," *Analytical biochemistry*, vol. 148, no. 1, pp. 254–259, 1985.

[192] C. E. Hoyle, A. B. Lowe, and C. N. Bowman, "Thiol-click chemistry: a multifaceted toolbox for small molecule and polymer synthesis," *Chemical Society Reviews*, vol. 39, no. 4, pp. 1355–1387, 2010.

[193] B. Lu and M. M. Maharbiz, "Protein patterning using germanium as a sacrificial layer," in *Engineering in Medicine and Biology Society (EMBC), 2017 39th Annual International Conference of the IEEE*, IEEE, 2017.

[194] B. Lu and M. M. Maharbiz, "Germanium as a scalable sacrificial layer for nanoscale protein patterning," *PloS one*, vol. 13, no. 4, e0195062, 2018.

[195] M. Chaimberg and Y. Cohen, "Note on the silylation of inorganic oxide supports," *Journal of colloid and interface science*, vol. 134, no. 2, pp. 576–579, 1990.

[196] D. Liu, P. R. Johnson, and M. Elimelech, "Colloid deposition dynamics in flow-through porous media: Role of electrolyte concentration," *Environmental science & technology*, vol. 29, no. 12, pp. 2963–2973, 1995.

[197] S. Upadhyayula, T. Quinata, S. Bishop, S. Gupta, N. R. Johnson, B. Bahmani, K. Bozhilov, J. Stubbs, P. Jreij, P. Nallagatla, *et al.*, "Coatings of polyethylene glycol for suppressing adhesion between solid microspheres and flat surfaces," *Langmuir*, vol. 28, no. 11, pp. 5059–5069, 2012.

[198] J. Cras, C. Rowe-Taitt, D. Nivens, and F. Ligler, "Comparison of chemical cleaning methods of glass in preparation for silanization," *Biosensors and bioelectronics*, vol. 14, no. 8, pp. 683–688, 1999.

[199] T. E. Saxl, "Electrorotation of the bacterial flagellar motor," PhD thesis, University of Oxford, 2007.

[200] V. A. Bespalov, I. B. Zhulin, and B. L. Taylor, "Behavioral responses of *Escherichia coli* to changes in redox potential," *Proceedings of the National Academy of Sciences*, vol. 93, no. 19, pp. 10 084–10 089, 1996.

[201] O. Béja, L Aravind, E. V. Koonin, M. T. Suzuki, A. Hadd, L. P. Nguyen, S. B. Jovanovich, C. M. Gates, R. A. Feldman, J. L. Spudich, *et al.*, "Bacterial rhodopsin: evidence for a new type of phototrophy in the sea," *Science*, vol. 289, no. 5486, pp. 1902–1906, 2000.

[202] D. C. Fung and H. C. Berg, "Powering the flagellar motor of *Escherichia coli* with an external voltage source," *Nature*, vol. 375, no. 6534, p. 809, 1995.

[203] K Nogawa, M Kojima, M Nakajima, M Homma, and T Fukuda, "Driving force control of flagellar motor by local environmental control system with nano/micro dual pipettes," *J. Robotics Society of Japan*, vol. 29, no. 5, pp. 463–469, 2011.

[204] M. Kim and A. A. Julius, *Microbiorobotics: biologically inspired microscale robotic systems*. William Andrew, 2012.

[205] L. R. Cleveland and A. Grimstone, "The fine structure of the flagellate *Mixotricha paradoxa* and its associated micro-organisms," *Proceedings of the Royal Society of London B: Biological Sciences*, vol. 159, no. 977, pp. 668–686, 1964.

[206] S. L. Tamm, "Flagellated ectosymbiotic bacteria propel a eucaryotic cell.," *The Journal of cell biology*, vol. 94, no. 3, pp. 697–709, 1982.

[207] S. L. Tamm, "Locomotory waves of *Koruga* and *Deltotrichonympha*: Flagella wag the cell," *Cell motility and the cytoskeleton*, vol. 43, no. 2, pp. 145–158, 1999.

[208] L. M. Tender, S. A. Gray, E. Groveman, D. A. Lowy, P. Kauffman, J. Melhado, R. C. Tyce, D. Flynn, R. Petrecca, and J. Dobarro, "The first demonstration of a microbial fuel cell as a viable power supply: powering a meteorological buoy," *Journal of Power Sources*, vol. 179, no. 2, pp. 571–575, 2008.

[209] W. M. Rohsenow and H. Y. Choi, *Heat, mass, and momentum transfer*. Prentice Hall, 1961.

Appendix A

Process notes

This appendix presents more details about the specific fabrication processes used in this dissertation and developed at the Marvell Nanofabrication Facility. I have synthesized the following notes from my cleanroom notebook and attempted to make them as complete as succinctly possible. I have tried to provide more details and explanation where applicable for process adaptation. Some facility-specific minutiae has been included where it may assist users of the Marvell Nanofabrication Facility, though these details reflect the time and place that this process was developed and may deviate as time marches on. Metrology steps are generally excluded. Please proceed with caution!

A.1 Glossary of terms and tools

Term	Description
DUV	deep ultra-violet
EBPVD	electron beam physical vapor deposition
ENIG	electroless nickel immersion gold
HMDS	hexamethyldisilazane
IPA	isopropyl alcohol
LOR	lift-off resist
LPCVD	low pressure chemical vapor deposition
LTO	low temperature oxide
MOS	metal oxide semiconductor
PM	primary mark
PVD	physical vapor deposition
PR	photoresist
QDR	quick dump rinse
SRD	spin rinse dry
TCP	transformer coupled plasma
UV	ultra-violet

Table A.1: Terms used in process notes.

Tool	Description
asml300	ASML 5500/300 4X reduction stepper
axcelis	AXCELIS Fusion M200PCU Photostabilizer System
cha	CHA Solution electron-beam evaporator
disco	Disco DAD3240 automatic dicing saw
headway2	Headway stand-alone manual load photoresist spinner
lam6	Oxide Rainbow Etcher
lam7	Metal Al TCP Etcher
lam8	Poly-Si TCP Etcher
matrix	Matrix 106 resist removal system
mrc944	MRC 944 sputtering system with sputter-etch
msink1	Photoresist strip and pre-furnace metal clean sink
msink2	General purpose photoresist strip sink
msink6	MOS clean wet sink for pre-furnace clean
msink8	Non-MOS clean wet sink for post PR-strip
msink16	General purpose sink used for lift-off
msink20	Ultrasonic lift-off and general solvent sink
picotrack1	Picotrack coater system
picotrack2	Picotrack developer system
primeoven	HMDS prime oven
ptherm	Plasma-Therm parallel plate etcher
quintel	Quintel Q4000 mask aligner
svgcoat1	SVG 8626 6” photoresist coat track (i-line resists)
svgcoat3	SVG 8626 6” lift-off resist coat track
svgcoat6	SVG 8800 6” photoresist coat track (DUV resists)
svgdev6	SVG 8800 6” photoresist develop track
technics-c	Technics C Plasma Etching System
tystar12	Tylan non-MOS clean LTO LPCVD furnace
tystar20	Tylan non-MOS clean Si-Ge LPCVD furnace
vacoven	YES vacuum oven
westbond	Westbond wirebonder model 7400B

Table A.2: Marvell Nanofabrication Facility tools used in this work.

A.2 Electrode array process

A.2.1 Alignment marks in opaque annulus

This process is used to pattern an opaque Al ring on the front side of the silica substrate with primary marks (PMs) for alignment in the **asml300** stepper. This step is necessary to fully take advantage of the **asml300**'s 50 nm interlayer alignment tolerance. For designs that may tolerate 1 µm interlayer misalignment, the front side PMs are optional as the next layer may be instead patterned by a contact aligner. This process also deposits a thin metal layer on the backside of the wafer to enable electrostatic chuck clamping on downstream tools, as well as render the wafer visible to capacitive index sensors on the coater tracks.

1. **msink8**: Clean 500 nm-thick 6″ diameter fused silica wafers
   - 10 min dip in 90 °C piranha solution, then rinse with QDR and dry with SRD
   - Should not follow with customary HF dip because this would etch the silica wafers
2. **mrc944**: Deposit 120 nm Al on wafer backside by PVD
   - 20 cm/ sec target speed, 1 kW power, 4 passes
   - This conductive and opaque backside layer enables wafer to clamp to electrostatic chucks in downstream tools
   - Another option is to deposit 120 nm Cr onto the wafer backside using the **cha** EBPVD tool
3. **mrc944**: Deposit 120 nm Ti on wafer frontside by PVD
   - 50 cm/ sec target speed, 1 kW power, 20 passes
4. **primeoven**: HMDS prime
   - Recipe 2, deposits a multilayer of HMDS with a 2 min prime at 90 °C to promote photoresist adhesion
5. **picotrack1**: Spin coat 420 nm DUV210-0.6
   - 7000 rpm spin speed
   - 130 °C, 60 sec soft bake
6. **asml300**: Expose PM and CENTERHOLE layers, 20 mJ cm^{-2} dose
   - PMs are diffraction gratings used for interlayer alignment
   - CENTERHOLE is used to clear a square of silica square on the wafer for the devices

7. **pictotrack2**: Develop resist
    - PEB 130 °C, 60 sec
    - 60 sec puddle in MF-26A
8. **axcelis**: Hard bake DUV resist
    - Recipe U:
        a) 20 sec 110 °C prebake
        b) 20 sec ramp to 140 °C with low UV power
        c) 30 sec postbake 140 °C with high UV power
9. **lam7**: Anisotropic Al etch to define PMs
    - 7001_Al_ME Standard Al Main Etch recipe
    - 800 W RF Power, 90 sccm Cl_2, 45 sccm BCl_3, 8 mTorr, 60 sec etch time
10. **matrix**: Strip photoresist with oxygen plasma
    - 450 W, 150 sec
    - Must remove all organics before proceeding to **mrc944**
11. **mrc944**: Deposit 40 nm Al on wafer frontside by PVD
    - Al is more reflective than Ti at the HeNe wavelength ($\lambda = 633$ nm) used for asml300 interlayer alignment [209].
    - Al is necessary for a sufficiently strong alignment signal when viewed through subsequent process layers. Ti works under some conditions, but Al is more consistent.
12. **picotrack1**: Spin coat 420 nm DUV210-0.6
    - 7000 rpm spin speed
    - 130 °C, 60 sec soft bake
13. **asml300**: Expose CENTERHOLE layer, 20 mJ cm^{-2} dose
14. **pictotrack2**: Develop resist as in step 7
15. **axcelis**: Hard bake DUV resist as in step 8
16. **lam7**: Anisotropic Al etch to clear the center of the wafer as in step 9
17. **matrix**: Strip photoresist with oxygen plasma as in step 10

A.2.2 Metalization

This standard lift-off process is used to pattern the Au electrode array. A thin Ti layer is used to promote Au adhesion to the silica substrate. LOR-5A lift-off resist is used to make lift-off edges cleaner and to accelerate the lift-off process.

18. **hotplate**: Dehydration bake
    - 200 °C, 5 min
    - Recommended by Microchem, manufacturer of LOR-5A, for adhesion and repeatability
    - A convection oven can be used if batch processing is desired, but 30 min bake is suggested in this case
19. **svgcoat3**: Spin coat 550 nm LOR-5A
    - 5000 rpm spin speed
    - 190 °C, 140 sec soft bake
20. **picotrack1**: Spin coat 420 nm DUV210-0.6
    - no HMDS prime necessary since DUV210-0.6 adheres well to LOR-5A
    - 7000 rpm spin speed
    - 130 °C, 60 sec soft bake
21. **asml300**: Expose metal layer, 12.5 mJ cm^{-2} dose
22. **picotrack2**: Develop resist
    - PEB 130 °C, 60 sec
    - 60 sec puddle in MF-26A
    - Approximately 500 nm PR undercut is desired for lift-off
    - Do not hard bake the resist
23. **technics-c**: Descum in O_2 plasma
    - 180 mTorr O_2, 50 W RF power, 30 sec
    - without descum, bond pads flake off during wire bonding
24. **cha**: Deposit 5 nm Ti and 145 nm Au by EBPVD
    - Pump vacuum pressure down to 1 µTorr before starting deposition
    - Ti deposits at 1 Å s^{-1}

- Au deposits at $5\,\text{Å}\,\text{s}^{-1}$

25. **msink16**: Lift-off in Remover 1165
    - Overnight at room temperature
    - If desired, heat Remover 1165 to 70 °C for faster lift-off (approximately 1 h).
    - Wash wafer with IPA spray and DI rinse once all metal has lifted off

Please note that the process described above uses the **asml300** stepper, but this layer could alternatively be patterned at a contact aligner if desired, using the lithographic patterning described in the Insulation section that follows.

A.2.3 Insulation

This procedure patterns a 2.8 µm thick spin-on polyimide layer over the electrodes for insulation. An aluminum hard mask is used to pattern the polyimide in an oxygen plasma etch process in order to remove insulation over the active regions of the electrodes and the wire bonding pads.

26. **msink2**: Clean wafer with 60 min dip in 80 °C Remover 1165, then rinse with QDR and dry with SRD
    - Wafer cleanliness very important for adhesion of the polyimide in the next steps
    - **msink2** is used since it is compatible with Au-coated wafers
27. **ptherm**: Clean wafer with oxygen plasma
    - Clean chamber with O_2 plasma for 5 min, 80 mTorr, 300 W RF power
    - Clean wafer with O_2 plasma for 2 min, 80 mTorr, 200 W RF power
    - **ptherm** is used since it is compatible with Au-coated wafers
28. **headway2**: Spin coat VM-651 adhesion promoter
    - Mix VM-651 to 0.1 % in DI water
    - Spin program:
      a) Puddle VM-651 solution on the wafer for 20 seconds
      b) Spin 3000 rpm, 1000 rpm/ sec ramp, 30 sec to remove excess
    - Put wafer in 120 °C convection oven for 15 min to dry its surface
29. **headway2**: Spin coat PI-2610 polyimide precursor
    - Spin program:

a) Spin 500 rpm, 100 rpm/ sec ramp, 30 sec
b) Stop spinning and wait 30 sec to inspect spreading
c) Spin at full speed 2500 rpm, 300 rpm/ sec ramp, 30 sec

30. **vacoven**: Cure polyimide at 450 °C for 30 min

- Cure under N_2 at 200 Torr, hot N_2 for ramp-up and dwell, both hot and room temperature N_2 for ramp-down and dehydration
- Use five nitrogen pump-purge cycles to dehydrate vacuum oven before running the oven program
- Oven program:
  a) 75 °C, 20 min to allow dehydration loops to complete
  b) ramp up to 300 °C in 60 min
  c) hold at 300 °C for 30 min to allow temperature to stabilize
  d) ramp up to 450 °C in 60 min
  e) hold at 450 °C for 30 min to cure
  f) ramp down to 75 °C in 1 min for faster ramp down
  g) hold setpoint at 75 °C for 20 h to wait for cooldown and idle

31. **svgcoat3**: Spin coat 1 µm LOR-5A

- 1000 rpm spin speed
- 190 °C, 200 sec soft bake

32. **svgcoat1**: Spin coat 1.2 µm OiR 906-12 (i-line resist)

- 4100 rpm spin speed
- 90 °C, 60 sec soft bake

33. **quintel**: Align and expose blocking layer

- Use pressure contact mode
- Total dose of i-line and g-line is 225 mJ cm^{-2}
- Typically requires 7-9 sec exposure

34. **svgdev6**: Develop resist

- PEB 120 °C, 60 sec
- 60 sec puddle in MF-26A developer
- Second develop, without hard bake, for 30 sec puddle in MF-26A developer
- Do not hard bake the resist

35. **cha**: Deposit 75 nm Al by EBPVD
    - Pump vacuum pressure down to 1 µTorr before starting deposition
    - Al deposits at 4 Å s^{-1}
36. **msink16**: Lift-off in Remover 1165
    - Overnight at room temperature
    - If desired, heat Remover 1165 to 70 °C for faster lift-off (approximately 1 h).
    - Wash wafer with IPA spray and DI rinse once all metal has lifted off
37. **ptherm**: Polyimide plasma etch
    - 80 mTorr, 80 sccm O_2, 150 W
    - Etch rate is about 200 nm/ min, but is not uniform. Etch for 10 min, then check and etch for an additional 5 min if required
    - Plasma is light blue in color and it becomes white-green as the polyimide is completely consumed
    - This step simultaneously etches away the photoresist and the polyimide
38. **msink16**: Backside Al etch
    - Immerse wafer in 150 mL Al Etchant Type A from Transene (80 % H_3PO_4, 5 % HNO_3, 5 % CH_3COOH, 10 % H_2O) and 50 mL DI at room temperature with light agitation until the Al is etched away (5-10 min)
    - This step removes the Al from the backside, making the devices transparent
    - Additionally, residual scum left over from the polyimide etch is removed

A.2.4 Singulation and assembly

40. **disco**: Dice the individual devices
    - Blade speed 30 000 rpm, feed rate 1 mm/ sec
    - 40 mm by 30.5 mm dies
41. **westbond**: Mount die to PCB and wire bond
    - Mount die to PCB with Crystal Bond
      a) heat hotplate to 130 °C and place interface PCB on hot plate, with two drops of Crystal Bond and wait for it to melt
      b) press die onto the liquid Crystal Bond and remove from heat, waiting for it to solidify

c) also can use binder clips to hold surfaces together while the assembly is left a convection oven to melt the Crystal Bond

- wedge wire bond with Al-1 % Si 0.001 25" diameter wire
- Power setting 300 for first bond (on die) and 400 on PCB ENIG pad
- the westbond wire bonder in 490 Cory Hall (pisterbond) may also be used

A.3 Bead process

A.3.1 PM definition

This process is used to etch primary marks into the Si substrate for interlayer alignment with the **asml300** stepper.

1. **msink6**: Clean 675 nm-thick 6" diameter Si p-type test wafers
   - 10 min dip in 90 °C piranha solution, then rinse with QDR
   - 1 min dip in room temperature 10:1 HF 49 %, then rinse with QDR and dry with SRD
2. **primeoven**: HMDS prime
   - Recipe 2, deposits a multilayer of HMDS with a 2 min prime at 90 °C to promote photoresist adhesion
3. **picotrack1**: Spin coat 420 nm DUV210-0.6
   - 7000 rpm spin speed
   - 130 °C, 60 sec soft bake
4. **asml300**: Expose PM layer
   - 20 mJ cm^{-2} dose
   - Six PMs are patterned, though only two are required for alignment
5. **picotrack2**: Develop resist
   - PEB 130 °C, 60 sec
   - 60 sec puddle in MF-26A
6. **axcelis**: Hard bake DUV resist
   - Recipe U:
     a) 20 sec 110 °C prebake

b) 20 sec ramp to 140 °C with low UV power
c) 30 sec postbake 140 °C with high UV power

- Improves Si etch selectivity

7. **lam8**: Etch 240 nm PMs into Si wafer
   - 8001_POLY_ME Standard Poly-Si Main Etch recipe
   - 12 mTorr, 50 sccm Cl_2, 150 sccm HBr, 300 W RF Power, 60 sec etch time
   - 120 nm is the nominal PM depth, but 240 nm seems to work better when aligning through LTO in subsequent steps
8. **matrix**: Strip photoresist with oxygen plasma
   - 450 W, 150 sec

A.3.2 Silica bead definition

This process is used to define the LTO beads on a Ge sacrificial layer.

9. **msink8**: Clean wafers in post-PR processing sink
   - 10 min dip in 90 °C piranha solution, then rinse with QDR
   - 1 min dip in room temperature 10:1 HF 49 %, then rinse with QDR and dry with SRD
   - This extra cleaning step is required since the wafer has been through PR processing before proceeding to the furnaces
10. **msink6**: Clean wafers in pre-furnace sink
    - 10 min dip in 90 °C piranha solution, then rinse with QDR
    - 1 min dip in room temperature 10:1 HF 49 %, then rinse with QDR and dry with SRD
11. **tystar20**: Deposit 400 nm Ge by LPCVD
    - 340 °C, 600 mTorr, 90sccm GeH_4
    - Deposition rate approximately 6 nm/ min, so I deposit for 70 min
    - This is the sacrificial release layer, so precise thickness is not important
12. **tystar12**: Deposit 750 nm LTO by LPCVD
    - 450 °C, 300 mTorr, 90sccm SiH_4, 135 sccm O_2
    - Deposition rate approximately 11 nm/ min, so I deposit for 70 min

13. **picotrack1**: Spin coat 900 nm DUV210-0.6
    - 1450 rpm spin speed
    - 130 °C, 60 sec soft bake
14. **asml300**: Expose desired BEADS layer
    - 10.66 mJ cm^{-2} for RODS
    - 9.33 mJ cm^{-2} for WHEELS
15. **picotrack2**: Develop resist
    - PEB 130 °C, 60 sec
    - 60 sec puddle in MF-26A
16. **axcelis**: Hard bake DUV resist
    - Recipe U:
      a) 20 sec 110 °C prebake
      b) 20 sec ramp to 140 °C with low UV power
      c) 30 sec postbake 140 °C with high UV power
17. **lam6**: Etch LTO to define beads
    - 6001_OXIDE_ME Standard Anisotropic silicon oxide etch recipe
    - 70 mTorr, 150 sccm Ar, 25 sccm CHF_3, 25 sccm CF_4, 750 W RF Power, 60-120 sec etch time
    - Monitor the endpoint detection signals to be sure to over-etch at least 20 sec since the etch rate is not uniform, otherwise you will encounter the frustrating "blister packing" effect
18. **matrix**: Strip photoresist with oxygen plasma
    - 450 W, 150 sec

A.3.3 Gold patch patterning

This procedure uses a lift-off process and the **asml300** stepper to pattern 500 nm-diameter circular Au patches in the center of each bead.

19. **picotrack1**: Spin coat 900 nm DUV210-0.6
    - 1450 rpm spin speed
    - 130 °C, 60 sec soft bake

20. **asml300**: Expose PATCHES layer
    - $40\,\mathrm{mJ\,cm^{-2}}$ dose
    - dark field pattern so a higher exposure than usual is used
21. **picotrack2**: Develop resist
    - PEB 130 °C, 60 sec
    - 60 sec puddle in MF-26A
22. **technics-c**: Descum in O_2 plasma
    - 180 mTorr O_2, 50 W RF power, 30 sec
23. **cha**: Deposit 5 nm Ti and 30 nm Au by EBPVD
    - Pump vacuum pressure down to 1 µTorr before starting deposition
    - Ti deposits at $1\,\mathrm{Å\,s^{-1}}$
    - Au deposits at $5\,\mathrm{Å\,s^{-1}}$
24. **msink20**: Sonication-assisted lift-off
    - immerse wafer in Remover 1165
    - sonicate in room temperature water bath for 5 min
    - rinse wafers with IPA and dry with N_2 gun

Appendix B

Spinner processing code

B.1 Workflow

The data processing workflow pictured in Figure B.1 was used to process microscopy of tethered spinning cells. The scripts and associated files can be found at the end of this Appendix in condensed form. The most recent versions of the code files can be found online in the following Git repository: `https://github.com/zajdel/Spinners`. Three programs provide the majority of processing:

1. **StitchStacks.ijm** - ImageJ macro that converts image sequence to binarized stack
2. **1_create_traces.py** - Python script that produces heading traces, using user assistance to identify spinning cells
3. **2_quality_control.py** - Python script that annotates spinning direction, using user assistance to select direction thresholds

Streams of tethered spinner cells are saved as a series of .tif images that are to be stitched together into a stack. At the same time, files are filtered and then binarized for black cell bodies on a white background. This is accomplished with the ImageJ macro **StitchStacks.ijm**. Then, **1_create_traces.py** is used to select the spinner cells and extract heading traces. The program takes the file location of the binarized image as an input. The command line function call looks like this:

```
>> 1_create_traces.py folder\stackname
```

The program averages several hundred frames from the binarized stack, resulting in a circle surrounding the tether point of each spinning cell as shown in Figure B.2. These mean circles are overlaid on top of a looping video of the first few hundred frames of the stack. The user selects an estimated tether point on the mean image and the program searches for the darkest pixel in the region immediately surrounding this selection. The result is a .csv file with the following format:

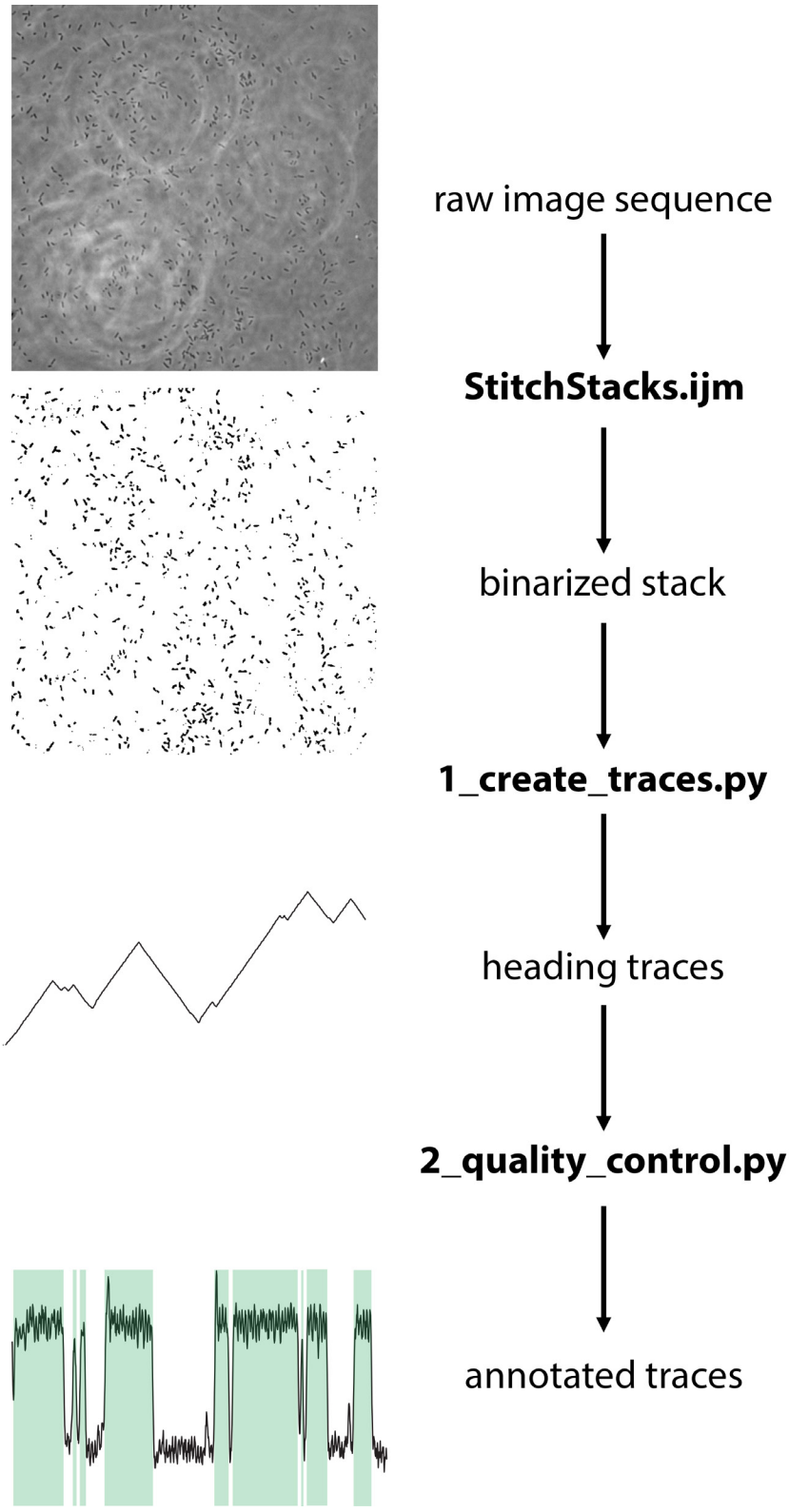

Figure B.1: Spinner signal processing workflow.

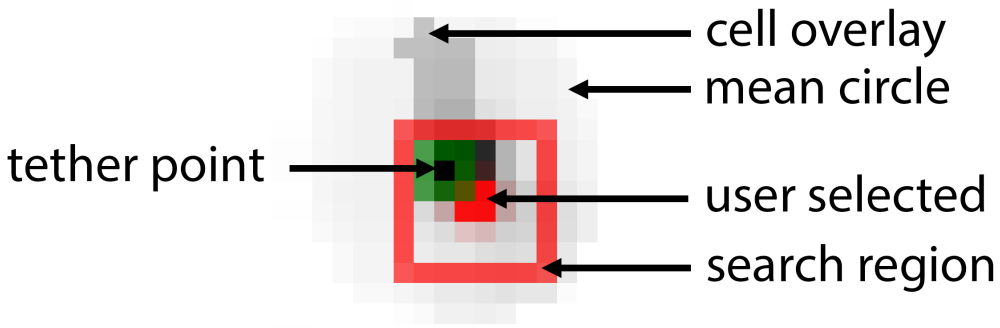

Figure B.2: Detecting the tether point of a spinner cell with **1_create_traces.py**. This is a magnified screen capture of the program at runtime. The solid red square marks the pixel that the user selects, and the program searches within the larger red square outline for the darkest pixel of the mean image, marked in green.

```
x_coord,  y_coord,     tL,     tH,  heading1,  heading2,  heading3, ...
    298,      192,     -1,     -1,   -2.3562,    -0.245,   -0.6435, ...
    255,      114,     -1,     -1,    -0.245,    -0.588,   -1.1071, ...
```

For each selected cell, the (x,y) coordinates of the tether point, -1 is written to both the low direction threshold (tL) and high direction threshold (tH), and the computed headings are all written to the .csv. This file is further processed by **2_quality_control.py**.

```
>> 2_quality_control.py folder\csvname
```

This program sets the high and low thresholds for every cell's velocity, producing a new .csv file with the user-selected thresholds. If a user determines that a given trace should be excluded from analysis, a zero is written to both thresholds. The result is a .csv file with the following format:

```
x_coord,  y_coord,     tL,     tH,  heading1,  heading2,  heading3, ...
    298,      192,   0.10,  -0.36,   -2.3562,    -0.245,   -0.6435, ...
    255,      114,      0,      0,    -0.245,    -0.588,   -1.1071, ...
```

Further analysis can be completed now that the thresholds for direction labeling have been selected and problematic traces have been flagged.

B.2 StitchStacks.ijm

```
/*
-----------------------------------------------------
```

```
StitchStacks.ijm
ImageJ Macro
Purpose: open a folder consisting of frames from a
spinner stream, then filter, segment, and save as zip
-------------------------------------------------------
*/

// pick out the directory that
dir = getDirectory("Pick date to process!");

// retrieve all frames from the folder
list = getFileList(dir);

for (i=0; i<list.length; i++) {
   // if this is a folder, concatenate the images inside!
   if (endsWith(list[i], "/"))
   {
        // open the frames
      experiment = list[i];
      list2 = getFileList(dir+experiment);
      tifname=list2[0];
      run("Image Sequence...", "open="+dir+list[i]+tifname+" sort use");

        // process and binarize the image
        run("8-bit");
      run("Smooth","stack");
      run("Unsharp Mask...", "radius=1 mask=0.90 stack");
      run("Auto Threshold...", "method=Default white stack");

        // save as zip
      title = substring(experiment,0,lengthOf(experiment)-1);
      saveAs("ZIP", dir+title+".zip");
      close();
   }
}
```

B.3 utilities.py

```
# Import packages
from __future__ import division, unicode_literals # , print_function
import argparse
import numpy as np
```

```
from matplotlib import animation
import matplotlib.pyplot as plt
import matplotlib.patches as patches
from scipy.signal import medfilt
import pims
```

B.4 1_create_traces.py

```
from __future__ import division
from utilities import *
#  Ex. python 1_create_traces.py 100u_leu1 [TIF]
from PIL import Image
from Queue import Queue

parser = argparse.ArgumentParser(description="Create traces of cells identified
    in a TIF and output to CSV.")
parser.add_argument("source", help="source file [TIF]")
parser.add_argument("dest", nargs="?", help="destination file [CSV]")
parser.add_argument("-v", "--verbose", help="verbose output: display trace for
    every cell", action="store_true")
args = parser.parse_args()

tif_name = args.source + '.tif'
raw_frames = pims.TiffStack(tif_name, as_grey=False)
frames = np.array(raw_frames, dtype=np.uint8)

# use (and/or overwrite) existing file
centers = []
if args.dest:
    csv_name = args.dest + '.csv'
    data = np.loadtxt(csv_name, delimiter=",")
    centers, _, _ = np.hsplit(data, np.array([2, 3]))

# ^*^*^*^*^*^*^*^*^*^*^*^*^*^*^*^*^*^*^*^*^*^*^*^*^*^*^*^*^*^*^*^*^*^*^*^*^*^*^*^*^
# ^*^*^*^*^*^*^*^*^*^    Getting Mean Image     *^*^*^*^*^*^*^*^*^*^*^*^*^*^*^*^
# ^*^*^*^*^*^*^*^*^*^*^*^*^*^*^*^*^*^*^*^*^*^*^*^*^*^*^*^*^*^*^*^*^*^*^*^*^*^*^*^*^

# use only first 500 frames
mean = np.mean(frames[0:500], axis=0)

# ^*^*^*^*^*^*^*^*^*^*^*^*^*^*^*^*^*^*^*^*^*^*^*^*^*^*^*^*^*^*^*^*^*^*^*^*^*^*^*^*^
# ^*^*^*^*^*^*^*^*^*^  Overlay Mean on Frames  *^*^*^*^*^*^*^*^*^*^*^*^*^*^*^*^
```

```
# *^*^*^*^*^*^*^*^*^*^*^*^*^*^*^*^*^*^*^*^*^*^*^*^*^*^*^*^*^*^*^*^*^*^*^*^*^*^*^*^

overlay = Image.fromarray(mean).convert('RGB')
new_frames = []
for frame in frames:
    frame = Image.fromarray(frame).convert('RGB')
    new_frames.append(np.asarray(Image.blend(frame, overlay, 0.8)))
frameview = new_frames

# *^*^*^*^*^*^*^*^*^*^*^*^*^*^*^*^*^*^*^*^*^*^*^*^*^*^*^*^*^*^*^*^*^*^*^*^*^*^*^*^
# *^*^*^*^*^*^*^*^*^  Show Frames for Center Selection *^*^*^*^*^*^*^*^*^*^*^
# *^*^*^*^*^*^*^*^*^*^*^*^*^*^*^*^*^*^*^*^*^*^*^*^*^*^*^*^*^*^*^*^*^*^*^*^*^*^*^*^

# cycle through first 50 frames
N = 50
show_frames = frameview[0:N]

fig, ax = plt.subplots()
im = ax.imshow(show_frames[0], aspect='equal')

# if using existing CSV, show previously selected centers
for center in centers:
    rect = patches.Rectangle((center[0] - 0.5, center[1] - 0.5), 1, 1,
        linewidth=1, edgecolor='r', facecolor='none')
    ax.add_patch(rect)

# convert centers array to list of tuples and create a set from it
selected_points = set(tuple(map(tuple, centers)))


# Error handling on press: find minimum intensity in mean in 5x5 area around
    selected center
def on_press(event):
    if event.xdata and event.ydata:
        x, y = int(round(event.xdata)), int(round(event.ydata))
        print('You pressed {0} at ({1}, {2}) with mean value of
            {3}.'.format(event.button, x, y, mean[y, x]))

        rect = patches.Rectangle((x - 0.5, y - 0.5), 1, 1, linewidth=1,
            edgecolor='r', facecolor='none')
        ax.add_patch(rect)
        roi = [(i, j) for i in range(x - 2, x + 3) for j in range(y - 2, y + 3)
            if 0 < i < mean.shape[1] and 0 < j < mean.shape[0]]
        min_intensity = min([mean[p[::-1]] for p in roi]) # p[::-1] reverses tuple
```

```
        correct_x, correct_y = np.mean([p for p in roi if mean[p[::-1]] ==
           min_intensity], axis=0)
        selected_points.add(
            (correct_x, correct_y) # use set to avoid duplicates being stored.
               (use tuple because can hash.)
        )
        if correct_x != x or correct_y != y:
            print('Corrected green box at ({0}, {1})'.format(correct_x,
               correct_y))
            area = patches.Rectangle((x - 2.5, y - 2.5), 5, 5, linewidth=0.5,
               edgecolor='r', facecolor='none')
            correction = patches.Rectangle((correct_x - 0.5, correct_y - 0.5), 1,
               1, linewidth=0.5, edgecolor='g', facecolor='none')
            ax.add_patch(area)
            ax.add_patch(correction)


fig.canvas.mpl_connect('button_press_event', on_press)


def init():
    im.set_data(show_frames[0])


def animate(i):
    im.set_data(show_frames[i % N])
    return im


anim = animation.FuncAnimation(fig, animate, init_func=init, interval=100)
plt.show()

num_selected_points = len(selected_points)

# *^*^*^*^*^*^*^*^*^*^*^*^*^*^*^*^*^*^*^*^*^*^*^*^*^*^*^*^*^*^*^*^*^*^*^*^*^*^*^
# *^*^*^*^ Post-Processing: Calculate Angle and Generate Traces *^*^*^*^*^*^*^
# *^*^*^*^*^*^*^*^*^*^*^*^*^*^*^*^*^*^*^*^*^*^*^*^*^*^*^*^*^*^*^*^*^*^*^*^*^*^*^

# maximum distance a pixel can be to be considered part of cell defined by some
   chosen center
MAX_DISTANCE = 8

num_frames = len(frames)
```

```
def euclidean_distance(p1, p2):
    return np.linalg.norm(np.asarray(p1) - np.asarray(p2))


def find_furthest_points(center, frame):
    """Given a center and a frame, computes furthest connected points to center
       with distance less than MAX_DISTANCE"""
    # get all points connected to center ("cell"), find furthest points
    nearest_pixel_to_center = (int(round(center[0])), int(round(center[1])))
    fringe = Queue()
    fringe.put(nearest_pixel_to_center)
    cell = set()
    cell.add(nearest_pixel_to_center)
    marked = set()
    marked.add(nearest_pixel_to_center)

    # modified breadth-first search
    while not fringe.empty():
        p = fringe.get()
        p1 = (p[0] - 1, p[1])
        p2 = (p[0] + 1, p[1])
        p3 = (p[0], p[1] - 1)
        p4 = (p[0], p[1] + 1)
        p5 = (p[0] - 1, p[1] - 1)
        p6 = (p[0] - 1, p[1] + 1)
        p7 = (p[0] + 1, p[1] - 1)
        p8 = (p[0] + 1, p[1] + 1)
        for p in [p1, p2, p3, p4, p5, p6, p7, p8]:
            if (p not in marked
                    and 0 <= p[0] < len(frames[frame][1])
                    and 0 <= p[1] < len(frames[frame][0])
                    and euclidean_distance(center, p) <= MAX_DISTANCE
                    and frames[frame][p[1], p[0]] == 0):
                marked.add(p)
                cell.add(p)
                fringe.put(p)

    cell = list(cell)
    max_dist = max([euclidean_distance(p, center) for p in cell])
    return [p for p in cell if euclidean_distance(p, center) == max_dist]


# calculate angle by using furthest point from center
```

```
wrapped_traces = []
for center in selected_points:
    ellipses = []
    trace = []
    for i in range(num_frames):
        furthest_points = find_furthest_points((center[0], center[1]), i)
        if len(furthest_points) > 1:
            if len(trace):
                # take point whose angle is closest to previous angle
                furthest_point = min(furthest_points, key=lambda x: abs(trace[i -
                    1] % (2 * np.pi) - np.arctan2(x[0] - center[0], center[1] -
                    x[1]) % (2 * np.pi)))
            else:
                # TODO: what to do if first frame is ambiguous
                furthest_point = furthest_points[0]
        else:
            furthest_point = furthest_points[0]
        # define angle to increase positively clockwise
        ang = np.arctan2(center[1] - furthest_point[1], furthest_point[0] -
            center[0])
        trace.append(ang)

    # add wrapped trace to CSV output
    # prepend center_x, center_y, -1, -1 (unverified status)
    wrapped_traces.append(np.append([center[0], center[1]], np.append([-1, -1],
        trace)))

    if args.verbose:
        # unwrap trace and apply 1D median filter (default kernel size 3)
        unwrapped = medfilt(np.unwrap(np.asarray(trace[2:])))

        plt.xlabel('Frame', fontsize=20)
        plt.ylabel('Angle', fontsize=20)
        plt.title('Trace ({0}, {1})'.format(center[0], center[1]), fontsize=20)
        plt.plot(unwrapped, 'r-', lw=1)
        plt.grid(True, which='both')
        plt.show()

# output: center_x, center_y, status, status, trace
np.savetxt(args.dest or args.source + ".csv", wrapped_traces,
    fmt=','.join(["%.4f"] * 2 + ["%i"] * 2 + ["%.4f"] * num_frames))
```

B.5 2_quality_control.py

```
from utilities import *
#  Ex. python 2_quality_control.py 1mM_asp1
from math import sin, cos
from matplotlib.widgets import Button
from matplotlib.widgets import Slider

parser = argparse.ArgumentParser(description="Perform quality control on
    generated traces and/or determine thresholds for switches.")
parser.add_argument("source", help="source file [CSV]")
parser.add_argument("frames", nargs="?", help="frames [TIF]")
parser.add_argument("-d", "--dest", help="destination file [CSV]")
parser.add_argument("-t", "--type", type=int, choices=[0, 1, 2, 3], default=2,
                    help="""type of quality control: 0 - show trace,
                                                     1 - show reconstructed cells
                                                         overlaid on actual video,
                                                     2 - show velocity graph
                                                         processed from trace with
                                                         manual thresholding,
                                                     3 - show velocity graph
                                                         processed from trace with
                                                         automated threhsolding"""
                    )
args = parser.parse_args()

if args.frames is None and args.type == 2:
    parser.error("frames required when type is 1")

if args.frames:
    tif_name = args.frames + '.tif'
    raw_frames = pims.TiffStack(tif_name, as_grey=False)
    frames = np.array(raw_frames, dtype=np.uint8)

data_name = args.source + '.csv'
data = np.loadtxt(data_name, delimiter=",", ndmin=2)
num_cells = data.shape[0]
# Status code: (-1, -1): unverified,
#              (0, 0): verified - bad,
#              (1, 1): verified - good,
#              (x, y): verified - good with lower threshold x and upper threshold
    y
centers, status, trace = np.hsplit(data, np.array([2, 4]))
# for backward compatibility when status did not include threshold
```

```
if status.shape[1] == 1:
    status = np.hstack((status, status))

# *^*^*^*^*^*^*^*^*^*^*^*^*^*^*^*^*^*^*^*^*^*^*^*^*^*^*^*^*^*^*^*^*^*^*^*^*^*^*^
# *^*^*^*^*^*^*^*^*^*^*^*^ Helper Functions  *^*^*^*^*^*^*^*^*^*^*^*^*^*^*^
# *^*^*^*^*^*^*^*^*^*^*^*^*^*^*^*^*^*^*^*^*^*^*^*^*^*^*^*^*^*^*^*^*^*^*^*^*^*^*^


def moving_average(values, window=8):
    weights = np.repeat(1.0, window) / window
    sma = np.convolve(values, weights, 'valid')
    return sma


def hysteresis_threshold(tr, thresh_high, thresh_low):
    direction = np.zeros(len(tr))
    prev_direction = 1

    for k in range(0, len(tr)):
        if tr[k] < thresh_low:
            direction[k] = -1
            prev_direction = -1
        elif tr[k] > thresh_high:
            direction[k] = 1
            prev_direction = 1
        else:
            direction[k] = prev_direction

    return direction


def mad(arr):
    """Computes the median absolute deviation (MAD) of an input array."""
    med = np.median(arr)
    return np.median(np.abs(arr - med))


def threshold(y, lag, thresh_high, thresh_low, influence):
    """Dynamically thresholds input data array.
    Uses median, median absolute deviation, and asymmetric treatment of up and
        down signals to threshold input.
    Essentially a parametrized peak-trough detection algorithm.
    Args:
        y: input data
```

```
    lag: lag of moving window used to smooth data
    thresh_high: number of median absolute deviations data point differs
        above median to threshold up
    thresh_low: number of median absolute deviations data point differs below
        median to threshold down
    influence: influence (between 0 and 1) of new signals on median and
        median absolute deviation
Returns:
    signals, median filter, median absolute deviation filter
adapted from https://stackoverflow.com/q/22583391
"""
signals = np.zeros(len(y))
filtered_y = np.array(y)
med_filter = [0] * len(y)
mad_filter = [0] * len(y)
med_filter[lag - 1] = np.median(y[0:lag])
mad_filter[lag - 1] = mad(y[0:lag])
# for first lag signals, do not have prior data, so evaluate based on sign
for i in range(0, lag):
    signals[i] = 1 if y[i] > 0 else -1
for i in range(lag, len(y)):
    # UP: (y[i] - med_filter[i - 1] > threshold AND difference > 0.1) OR y[i]
        > 0.5 + min of 4 previous y[i]
    if (y[i] - med_filter[i - 1] > thresh_high * mad_filter[i - 1] and y[i] -
        med_filter[i - 1] > 0.3) or y[i] - min(y[i - 4:i]) > 0.4:
        signals[i] = 1

        filtered_y[i] = influence * y[i] + (1 - influence) * filtered_y[i - 1]
        med_filter[i] = np.median(filtered_y[(i-lag):i])
        mad_filter[i] = mad(filtered_y[(i-lag):i])
    # DOWN: (y[i] - med_filter[i - 1] < threshold AND difference < -0.1) OR
        y[i] < -0.5 + max of 4 previous y[i]
    elif (y[i] - med_filter[i - 1] < -thresh_low * mad_filter[i - 1] and y[i]
        - med_filter[i - 1] < -0.3) or y[i] - max(y[i - 4:i]) < -0.4:
        signals[i] = -1

        filtered_y[i] = influence * y[i] + (1 - influence) * filtered_y[i - 1]
        med_filter[i] = np.median(filtered_y[(i - lag):i])
        mad_filter[i] = mad(filtered_y[(i - lag):i])
    # NO CHANGE: signals[i] = signals[i - 1]
    else:
        signals[i] = signals[i - 1]
        filtered_y[i] = y[i]
        med_filter[i] = np.median(filtered_y[(i - lag):i])
```

```
            mad_filter[i] = mad(filtered_y[(i - lag):i])

    return np.asarray(signals), np.asarray(med_filter), np.asarray(mad_filter)

# *^*^*^*^*^*^*^*^*^*^*^*^*^*^*^*^*^*^*^*^*^*^*^*^*^*^*^*^*^*^*^*^*^*^*^*^*^*^
# *^*^*^*^*^*^*^*^*^*^*^*^*^*^ QC Type 1 *^*^*^*^*^*^*^*^*^*^*^*^*^*^*^*^*^
# *^*^*^*^*^*^*^*^*^*^*^*^*^*^*^*^*^*^*^*^*^*^*^*^*^*^*^*^*^*^*^*^*^*^*^*^*^*^


def animate_frames_overlay(counter):
    num_subplots = 9
    num_frames = data.shape[1]
    radius = 8

    fig, ax = plt.subplots(3, 3)
    animations = []
    cells = []
    time_text = fig.text(0.147, 0.92, '', horizontalalignment='left',
        verticalalignment='top')

    def init():
        for i in range(num_subplots):
            center_x, center_y = centers[counter].astype(np.int)
            ax[i % 3, i // 3].set_xlim(center_x - 8, center_x + 8)
            ax[i % 3, i // 3].set_ylim(center_y - 8, center_y + 8)
            animations.append(ax[i % 3, i // 3].imshow(frames[num_frames /
                num_subplots * i, center_y - 8:center_y + 8, center_x - 8:center_x
                + 8], aspect='equal', extent=[center_x - 8, center_x + 8, center_y
                - 8, center_y + 8]))
            x = [center_x, center_x + radius * cos(trace[counter, num_frames /
                num_subplots * i])]
            y = [center_y, center_y + radius * sin(trace[counter, num_frames /
                num_subplots * i])]
            cells.append(ax[i % 3, i // 3].plot(x, y)[0])
        time_text.set_text('Frame 0 of %d' % (num_frames / num_subplots))

    def animate(frame):
        for i in range(num_subplots):
            center_x, center_y = centers[counter].astype(np.int)
            animations[i] = ax[i % 3, i // 3].imshow(frames[(num_frames /
                num_subplots * i) + frame % (num_frames / num_subplots), center_y
                - 8:center_y + 8, center_x - 8:center_x + 8], aspect='equal',
                extent=[center_x - 8, center_x + 8, center_y - 8, center_y + 8])
```

```
            # angle is calculated with respect to numpy array, i.e. arctan(x/y),
                so we correct with
            # x = center_x + sin(theta) and y = center_y + cos(theta)
            x = [center_x, center_x + radius * cos(trace[counter, (num_frames /
                num_subplots * i) + frame % (num_frames / num_subplots)])]
            y = [center_y, center_y + radius * sin(trace[counter, (num_frames /
                num_subplots * i) + frame % (num_frames / num_subplots)])]
            cells[i].set_data(x, y)
        time_text.set_text(’Frame %d of %d’ % (frame % (num_frames /
            num_subplots), num_frames / num_subplots - 1))

    anim = animation.FuncAnimation(fig, animate, init_func=init, interval=80)
    plt.show()

# *^*^*^*^*^*^*^*^*^*^*^*^*^*^*^*^*^*^*^*^*^*^*^*^*^*^*^*^*^*^*^*^*^*^*^*^*^*^
# *^*^*^*^*^*^*^*^*^*^*^*^ QC Types 2 and 3  *^*^*^*^*^*^*^*^*^*^*^*^*^*^*^
# *^*^*^*^*^*^*^*^*^*^*^*^*^*^*^*^*^*^*^*^*^*^*^*^*^*^*^*^*^*^*^*^*^*^*^*^*^*^


def show_trace(counter):
    fig, ax = plt.subplots()

    def record_yes(event):
        status[counter] = thresh
        plt.close()

    def record_no(event):
        status[counter] = [0, 0]
        plt.close()

    unwrapped = np.unwrap(np.asarray(trace[counter]))
    ma_trace = moving_average(unwrapped, 8) # 8*1/32 fps ~ 250 ms moving average
        filter window
    velocity = np.convolve([-0.5, 0.0, 0.5], ma_trace, mode=’valid’)

    plt.xlabel(’Frame’, fontsize=20)
    plt.ylabel(’Angle’, fontsize=20)
    plt.title(’Trace ({0}, {1}): {2} of {3}’.format(centers[counter][0],
        centers[counter][1], counter + 1, num_cells), fontsize=20)

    if args.type == 0:
        plt.plot(unwrapped, ’r-’, lw=1)
    elif args.type == 2:
        thresh = [-1, -1]
```

```
        vel_range = np.abs(np.nanmax(velocity) - np.nanmin(velocity))
        # if thresh has previously been set
        if not np.array_equal(status[counter], [0, 0]) or not
            np.array_equal(status[counter], [-1, -1]):
            thresh_high, thresh_low = status[counter]
        else:
            thresh_high = np.nanmax(velocity) - vel_range * 0.50
            thresh_low = np.nanmin(velocity) + vel_range * 0.25
        thresh = [thresh_high, thresh_low]
        d = hysteresis_threshold(velocity, *thresh)

        def update_sensitivity(val):
            thresh_high = s_high_thresh.val
            thresh_low = s_low_thresh.val
            thresh[0], thresh[1] = thresh_high, thresh_low
            dd = hysteresis_threshold(velocity, *thresh)
            f1.set_ydata(dd)
            f2.set_ydata((thresh_high, thresh_high))
            f3.set_ydata((thresh_low, thresh_low))
            fig.canvas.draw_idle()

        s_high_thresh = Slider(fig.add_axes([0.20, 0.15, 0.65, 0.03]), 'Upper
            Threshold', -2.0, 2.0, valinit=thresh_high)
        s_low_thresh = Slider(fig.add_axes([0.20, 0.1, 0.65, 0.03]), 'Lower
            Threshold', -2.0, 2.0, valinit=thresh_low)
        s_high_thresh.on_changed(update_sensitivity)
        s_low_thresh.on_changed(update_sensitivity)
        f1, = plt.plot(range(0, len(velocity)), d, 'b-')
        f2, = plt.plot((0, len(velocity)), (thresh_high, thresh_high), 'g', lw=3)
        f3, = plt.plot((0, len(velocity)), (thresh_low, thresh_low), 'k', lw=3)
    elif args.type == 3:
        thresh = [1, 1] # no threshold in type 3, so set default to [1, 1]

        signals, med_filter, mad_filter = threshold(velocity, 4, 10, 3.5, 0.2)
        plt.plot(range(0, len(velocity)), velocity, 'r-')
        # FOR DEBUGGING USE, DISPLAY TRIGGERS FOR SWITCH
        # plt.plot(range(0, len(velocity)), med_filter, 'k', lw=0.5)
        # plt.plot(range(0, len(velocity)), med_filter + 10 * mad_filter, 'g',
            lw=0.5)
        # plt.plot(range(0, len(velocity)), med_filter - 3.5 * mad_filter, 'g',
            lw=0.5)
        plt.plot(range(0, len(velocity)), signals, 'b-')
        plt.ylim((-2, 2))
```

```
        plt.xlim((0, 1875))

    plt.grid(True, which='both')

    b_yes = Button(fig.add_axes([0.65, 0.9, 0.1, 0.03]), 'Yes')
    b_no = Button(fig.add_axes([0.80, 0.9, 0.1, 0.03]), 'No')
    b_yes.on_clicked(record_yes)
    b_no.on_clicked(record_no)

    figManager = plt.get_current_fig_manager()
    figManager.window.showMaximized()

    plt.show()


for i in range(num_cells):
    if args.type == 1:
        animate_frames_overlay(i)
    else:
        show_trace(i)

# output: center_x, center_y, status/upper threshold, status/lower threshold,
    trace
np.savetxt(args.source + "_checked.csv", np.hstack((centers, status, trace)),
    fmt=','.join(["%.4f"] * 2 + ["%.4f"] * 2 + ["%.4f"] * trace.shape[1]))
```